12-2-2022 10:00 AM

Synthesis and Surface Modification of Azide Decorated Silver Nanoclusters

Alexander H. Stöckli, *The University of Western Ontario*

Supervisor: Corrigan, John F., *University of Waterloo*
Co-Supervisor: Workentin, Mark S., *The University of Western Ontario*
A thesis submitted in partial fulfillment of the requirements for the Master of Science degree in Chemistry
© Alexander H. Stöckli 2022

Abstract

In nanocluster research, easy modification of the cluster surface while maintaining the cluster core remains a key challenge. Herein we report the synthesis, structure, and properties of four targeted Ag_{20} nanoclusters (NCs) with surface azide moieties, two of which have 8 azide moieties, $[CO_3@Ag_{20}(S^tBu)_{10}(m\text{-}N_3\text{-}C_6H_4COO)_8(DMF)_4]$ and $[CO_3@Ag_{20}(S^tBu)_{10}(p\text{-}N_3\text{-}C_6H_4COO)_8(DMF)_4]$, and two of which have 6 azide moieties, $[CO_3@Ag_{20}(S^tBu)_{10}(m\text{-}N_3\text{-}C_6H_4COO)_6(NO_3)_2(DMF)_4]$ and $[CO_3@Ag_{20}(S^tBu)_{10}(p\text{-}N_3\text{-}C_6H_4COO)_8(NO_3)_2(DMF)_4]$. These Ag_{20} NCs with surfaces azide moieties are the first examples of Ag nanoclusters that can undergo **c**luster **s**urface **s**train-**p**romoted **a**zide **a**lkyne **c**ycloaddition (CS-SPAAC) click reactions, introducing new functionality to the cluster surface. Reactivity was screened on the 8-azide NCs using a model strained cyclooctyne framework in *exo*-bicyclo[6.1.0]non-4-yn-9-ylmethanol (BCN) and a ferrocene functionalized derivative. Reaction products and parent clusters were characterized by UV-Vis., FT-IR, and NMR spectroscopies. The structure of the parent clusters and presence of surface azides was further confirmed by SCXRD analysis and XPS. Both tested clusters were found to be amenable to CS-SPAAC reactions with retention of the NC frameworks.

Keywords

Silver nanocluster, surface modification, click chemistry, strain promoted azide-alkyne cycloaddition

Summary for Lay Audience

Silver is a metal that is known to many people in everyday life from its use in jewelry and ornamentation, but also has a rich history in areas such as commerce (as a currency), culture (where different religions have associated it with God and made idols from it), medicine (where small silver molecules have applications in anti-cancer, anti-bacterial, anti-fungal drugs as examples) and analog photography. In more recent history, silver quantum dots became a large area of research interest in the 1990's because of their unique light emitting and semi-conducting properties, making them potential candidates for both medical imaging and solar power applications. However, a silver quantum dot is not a single substance but actually a group of substances of varying sizes with a small range. Because of this it is difficult to precisely change the properties and structures of these substances and account for that change. From this research, the desire to more finely control the structure of silver clusters and devise atomically precise formulae came, and was fulfilled by the advent of silver nanoclusters. Silver nanoclusters are smaller than quantum dots, but have a specific chemical formula and so a silver nanocluster refers to a single atomically defined substance. This means that any changes to the nanocluster can be exactly detailed since it changes the chemical formula of the cluster, and so relationships between composition and the properties of the nanocluster can be established. The surface attachments on cluster surfaces can both introduce cluster surface functionality and can change the composition and shape of the cluster core due to their differing stabilizing effects. Since nanoclusters are not easily modified after they are assembled, it would be beneficial to put groups on the cluster surface, that can easily and efficiently react with complementary molecules to deliver additional function. In this thesis I was able to make and characterize, for the first reported time, silver nanoclusters with surface azide groups and showed that they react with alkynes to add functionality to silver nanocluster surfaces.

Co-Authorship Statement

Chapter 1 was written by the author and edited by Prof. John Corrigan and Prof. Mark Workentin.

Chapter 2 was written as an article for submission to the *Journal of the American Chemical Society*. XPS data was collected and analyzed by Carolina Vega, and the paragraph discussing the XPS results was written by Carolina Vega. TEM images were collected by Natalie Hamada at the Canadian Centre for Electron Microscopy. Electrochemical analysis of **1-*p***, **1-*m*** and their click products with FcBCN was performed by Dr. Mahdi Hesari. The BCN and FcBCN used for test click reactions was made by Johanna De Jong, who also provided the experimental procedure used to obtain FcBCN. SCRXD data was collected and refined by Paul Boyle in the case of **1-*p***, and by Prof. John Corrigan in the case of **1-*m***. The chapter was edited by Prof. John Corrigan and Prof. Mark Workentin.

Chapter 3 was written by the author and edited by Prof. John Corrigan and Prof. Mark Workentin. SCXRD data for **2-*p*** and **2-*m*** were collected and refined by Prof. John Corrigan.

Acknowledgments

First, I would like to thank my thesis supervisors, Prof. John F. Corrigan and Prof. Mark S. Workentin, for giving me the opportunity to work on this project. In addition to their insight and guidance with the project, I want to thank them for helping me get acclimated to London, a city about ~24 times larger than the largest city I lived in up to when I started my studies, and told me the interesting things to check out around town and the nice local restaurants. I'd also like to acknowledge the effort that Prof. Corrigan and Prof. Workentin put in to maintaining some level of social environment within their research groups despite the challenges that the COVID-19 pandemic presented; I'm grateful for the opportunity to have met the enthusiastic, friendly, and talented researchers I know today through their groups. I'd also like to thank them for celebrating in my success since it is something that I'm reluctant to celebrate myself. I'd also like to thank Prof. Corrigan for collecting and refining the SCXRD data on three of my crystal samples, and I'd like to thank Prof. Workentin for all his help with the UV-Vis. measurements.

I would also like to thank my thesis examiners, Dr. Paul J. Ragogna and Dr. Kim M. Baines, for taking the time from their busy schedules to read about my work over the past two years. I hope that you will find the present work interesting. I'd also like to thank the professors who taught the courses I took for passing their knowledge on to me. In no particular order, I'd like to thank Prof. Elizabeth R. Gillies, who taught Advanced Chemical Communications, for vastly improving my writing; Prof. Yang Song, who taught Powder Diffraction, for making an incredibly complex subject easier to understand; Prof. Robert H. E. Hudson, who taught Nucleaic Acid Chemistry, for bringing the passion and energy to a subject area that was outside my usual interest deeply fascinating; and Prof. Mark S. Workentin, who taught Organic Photochemistry, for teaching me knowledge that was very useful in the course of the research project. More broadly, I'd like to thank the Department of Chemistry at the University of Western Ontario and including Dr. Paul Boyle who collected and refined SCXRD data on one of my samples, and Dr. Mat Willans for his help in the NMR facility. I'd also like to thank Dr. Chris Levy and Benjamin Bridge. Assisting with the teaching labs and watching students learn

about chemistry from hands-on experience was one of the more fun aspects of completing my studies, and Dr. Levy and Ben ensured that it ran as smoothly as possible for the TA's.

Naturally, I'd also like to thank my wonderful colleagues for welcoming me into the research groups and really making sure there was never a dull moment at the lab. Justin, thank you for your guidance with the first-year report and presentation, and for showing me some pretty cool organic chemistry and proton NMR spectra of organic molecules. Johanna, thank you for keeping me company in the Workentin lab, and always having some music playing. Thank you also for inviting me on lunch and Timmies runs – it was nice walking around campus and chatting outside the lab. Carolina, thank you for being so enthusiastic about chemistry and such a friendly person – your energy and kindness are quite contagious and you made the lab a nicer place just by being there. Jack, thank you for being my friend and consoling me when my experiments weren't going to well. Thank you also for playing chess and briscola with me – it was always a lot of fun even if I'm not particularly good at playing. I also enjoyed our conversations about nothing in particularly while just hanging around in the lab or cleaning the dirty glassware. Andy, thank you for the humour you brought to the Corrigan offices, I enjoyed discovering the secret Diels-Alder reactions you would hide all around the place. Mansha, thank you for always making sure the Corrigan labs were lively, and I appreciate the decorating you organized for the holidays. A boisterous, cheerful lab is a joy to step in to, and you made sure the Corrigan labs always had something interesting going on. Zahra, thanks for always asking me how I was doing when we saw each other in the halls. It was a small, kind gesture but was very appreciated. Jeffrey, thank you for being friendly – I liked chatting whenever you would visit my and Nils' office, or when I would visit yours. Nils, thank you for being like a brother to me. You've helped me countless times with advice or letting me bounce ideas off you, and you also shared with me your experiences that helped put my challenges with chemistry into a less severe context. It was always great talking to you and hearing about your family, or your stories from Germany or Finland, or hearing about how TA-ing was going or about your chemistry. It was also fun having someone to speak German with, and learning lots of new things about it. It was a great pleasure to meet and work with you all!

Table of Contents

List of Schemes

List of Figures

List of Schemes

List of Appendices

List of Abbreviations, Symbols and Nomenclature

1-*m*	[CO_3@Ag_{20}(S^tBu)$_{10}$(m-N_3-C_6H_4COO)$_8$(DMF)$_4$]	E_{CB}	Potential of conduction band
1-*p*	[CO_3@Ag_{20}(S^tBu)$_{10}$(p-N_3-C_6H_4COO)$_8$(DMF)$_4$]	E_{VB}	Potential of valence band
^1H	Proton (NMR Spectroscopy)	FcBCN	*exo*-bicyclo[6.1.0]non-4-yn-9-ylmethylferrocenecarboxylate
2-*m*	[CO_3@Ag_{20}(S^tBu)$_{10}$(m-$N_3C_6H_4COO$)$_{(6)}$(NO_3)$_2$(DMF)$_4$]	FT-IR	Fournier-Transformed Infrared (Spectroscopy)
2-*p*	[CO_3@Ag_{20}(S^tBu)$_{10}$(p-$N_3C_6H_4COO$)$_{(6)}$(NO_3)$_2$(DMF)$_4$]	GC	Glassy Carbon (Electrode)
2θ	Angle between incident and reflected x-ray beam.	GPa	Gigapascal
4-FBT	Fluorobenzenethiolate		
$^{13}C\{^1H\}$	Proton decoupled Carbon-13 NMR spectroscopy	hr.	Hour(s)
@	Encased within. For example CO_3@Ag_{20} denotes a carbonate molecule trapped within a Ag_{20} shell.	*In vivo*	Takes place or tested in a living organism
Å	Angstrom	K	Kelvin
°C	Degree Celsius	kV	Kilovolts
δ	Chemical shift	L	Litres

ε	Molar absorptivity, how well a material absorbs light at a specific wavelength	LUMO	Lowest unoccupied molecular orbital
$\lambda_{excitation}$	In fluorescence spectroscopy, the wavelength at which the material is excited before measuring the emission spectrum	m (NMR Data)	Multiplet
λ_{max}	In an absorbance spectrum, wavelength at which most intense absorbance is observed	Me	Methyl ($-CH_3$)
$\lambda_{max\ emission}$	The wavelength in a fluorescence spectrum where the most intense emission is observed	MeCN	Acetonitrile
μA	Microampere	mg	Milligram
φ Scan	In crystallography, scan along axis perpendicular to ω scan	MHz	Megahertz
ω Scan	In crystallography, angle of scan along the same axis as 2θ between the sample holder and incident x-ray	min.	Minute
Ag	Silver	mL	Millilitre, 0.001 L
Ag_2S	Silver(I) sulfide	mM	Millimolar, 0.001 mol L^{-1}
Au	Gold	mmol	Millimole, 6.022×10^{20} molecules

BARAC	Biarylazacyclooctynone	mol	Mole, 6.022×10^{23} molecules
BCN	$(1\alpha, 8\alpha, 9\alpha)$-bicyclo[6.1.0]non-4-yn-9-ol	mV	Millivolt
^{t}Bu	*Tert*-butyl, $(-C-(CH_3)_3)$	NHC	N-Heterocyclic Carbene
br (NMR Data)	Broad	nm	Nanometre
CDCl	Deuterated Chloroform	NMR	Nuclear Magnetic Resonance
CdS	Cadmium Sulfide	ns	Nanosecond
cm	Centimetres	$O_2^{\bullet-}$	Superoxide Radical
cm^{-1}	Wavenumber	OH	Hydroxyl
CS-SPAAC	Cluster Surface Strain-Promoted Azide-Alkyne Cycloaddition	$OH^{\bullet}$	Hydroxyl Radical
Cu	Copper	POMS	Polyoxometalate
CuAAC	Copper-Catalyzed Azide-Alkyne Cycloaddtion	POSS	Polyhedral oligomeric silsesquioxane
CV	Cyclic Voltammetry, Cyclic Voltammogram	ppm	Parts per million
d (NMR Data)	Doublet	q (NMR Data)	Quartet
DCC	N,N'-dicyclohexylcarbodiimide	Quantum Yield	Measure of number of photons emitted by a material vs. photons absorbed

DCM	Dichloromethane, CH_2Cl_2	RCOO$^-$	Carboxylate
DIBAC	Aza-dibenzocyclooctyne	RNA	Ribonucleic Acid
DIBO	Dibenzocyclooctyne	s (NMR Data)	Singlet
DIFO	3,3-difluorocyclooctyne	s., sec.	Second(s)
DIMAC	6,7-dimethoxyazacyclooct-4-yne	SCXRD	Single Crystal X-Ray Diffraction
DMAc	Dimethylacetamide	SG	Glutathione
DMAP	4-Dimethyl aminopyridine	SPAAC	Strain-Promoted Azide-Alkyne Cycloaddition
DMF	Dimethylformamide	SR	Thiolate
DMI	1,3-dimethyl-2-imidazolidinone	SWCNT	Single-walled carbon nanotube
DMSO-d_6	Deuterated Dimethyl sulfoxide	t (NMR Data)	Triplet
DNA	Dioxyribonucleic Acid	TBAPF$_6$	tetra-n-butylammonium hexafluorophosphate
dppp	1,3-Bis(diphenylphosphino)propane	TEM	Transmission Electron Mircoscopy
DPV	Differential Pulse Voltammetry/Voltagram	THF	Tetrahydrofuran
$E_{1/2}$	Halfwave Potential	TiO$_2$	Titanium(IV) Dioxide

Et	Ethyl, (-CH_2CH_3)	UV-Vis.	Ultraviolet-visible light (~200-800 nm)
Et$_2$O	Diethyl Ether	V	Volts
EtOAc	Ethyl Acetate	XPS	X-ray photoelectron spectroscopy
eV	Electron Volt (1.602×10^{-19} J)	ZnO	Zinc Oxide

<div align="center">

Chapter 1

</div>

1   Project Background and Current Objectives

This chapter provides the general background knowledge on which the current work is based. First, the historical use of silver in commerce, culture, medicine and imaging is discussed to give the reader a broad understanding of how versatile silver chemistry can be. After this, silver quantum dots are discussed in the context of medical imaging and semiconducting materials, as they represent a major area of research interest in silver nanomaterials in the 1990's. From this research, the desire to more finely control the structure of silver clusters and devise atomically precise formulae came and was fulfilled by the advent of silver nanoclusters. The surface ligands on silver nanoclusters can both introduce cluster surface functionality and can change the composition and morphology of the cluster core due to their differing stabilizing effects. Since nanoclusters are not easily modified post-assembly, it would be of interest to install azide surface groups, which can participate in azide-alkyne cycloadditions to create triazole linkages with a new functional group, demonstrating easy surface modifiability.

1.1   A Brief Introduction to Silver, Ag

Silver (Ag) is an interesting metal and has been considered so for a very long time. The indigenous peoples of South America, particularly the Inka, refined silver since prehistoric times to make ceremonial objects and status symbols, as silver was associated with the moon and the Inka royalty.[1,2] The Old Testament in the Bible mentions silver being crafted from ores by cupellation and used in a variety of ways, such as in the making of religious idols, musical instruments, money, offering trays, and as a construction material for buildings of religious or spiritual importance.[3] The monetary value of silver is also of historical importance, as silver was used as a dominant form of currency from biblical times up until the late 1800's.[4] In fact, it has been said that the discovery of vast amounts of silver in the New World represents one of the biggest changes in the global economy in

history.[5] Being of value, it was used to fund wars and also taken as plunder by nations and thieves alike, most notably in the Caribbean piracy which targeted Spanish silver fleets.[6]

Silver has been used in various medical applications since ancient times. Ancient Persians, Greeks, Phoenicians, Romans, and Egyptians are all accounted to have used silver's anti-microbial properties to their advantage in food and water storage. Silver solutions were also used in dressing wounds and aiding in healing stomach ulcers in ancient Greece.[7,8] In the centuries that followed, silver and specifically silver nitrate were used to treat all manner of disease and maladies, such as bad breath, epilepsy, heart palpitations and brain infections.[7,8] In the 1900's, silver was used extensively in surgical sutures and wound dressings to prevent infections.[7,8]

Even silver's tendency to form photosensitive compounds, a challenging drawback in synthetic chemistry, is highly useful in the right context. Before the advent of digital photography, silver(I) halide salts were used to create pictures.[9] Briefly, a thin suspension of silver halide on a solid medium was exposed to light, causing some of the silver to be reduced to metallic silver, particularly where the intensity of the light was strongest.[9] Excess silver halide is washed away, historically with thiosulphate salts, and only a negative image, where the brightest areas appear darkest and darkest areas appear lightest, is left.[9] A positive image is made by projecting light through the negative image onto another suspension of silver(I) halide salts.[9]

Silver is still an important metal in modern research. For example, small silver coordination complexes with ligands such as N-heterocyclic carbenes (NHCs), phosphines, nitrogen-containing heterocycles, and approved pharmaceuticals have shown great potential as anticancer, anti-inflammatory, antimicrobial, and antifungal, antibacterial, and antimalarial agents.[10] Another frontier in modern silver chemistry is in the realm of nanochemistry. As will be detailed below, silver nanoparticles and nanoclusters have a broad range of potential applications, depending on their properties, which derive from their size, structure, composition and surface chemistry. In a funny coincidence, one of the main applications

silver nanoparticles are investigated for is in medical imaging, drawing on a combination of silver's histories as a medicine and imaging agent in photography.

1.2 Silver Sulfide (Ag$_2$S) Quantum Dots

A quantum dot is a material which exhibits the quantum confinement effect with respect to its band structure and so has size dependent luminescent and semi-conductor properties.[11] Most quantum dots fall in a size range from 2 – 10 nm, with larger quantum dots displaying a lesser quantum confinement effect compared to smaller quantum dots of like composition, and thus having narrower bandgaps.[11] Quantum dots based on Ag$_2$S frameworks are of research interest due to properties which are amenable for applications in chemical sensing, photovoltaics, and bio-imaging.[12-20]

With regards to photovoltaics, narrow band-gap semiconductors are desired to sensitize wide band-gap semiconductors like ZnO and TiO$_2$, to improve their ability to harvest visible and infrared light.[13-15] The bandgap of Ag$_2$S quantum dots depends on their size and is larger than that of the bulk material due to quantum confinement,[12,13] but still small enough that it extends the absorbance of the wide bandgap semiconductor into the visible light region, as shown in **Figure 1.1**.[13-15] Depositing these quantum dots onto the surface of wide bandgap semiconductors is beneficial because the electrons generated quickly inject into the semiconductor and separate from the electron holes where this process is slower in a thicker Ag$_2$S coating, allowing for recombination of electrons and electron holes.[13,15] These semiconductor composites can also be used for organic vapour sensing as they generate active radical oxygen species such as O$_2^{\bullet-}$ and OH$^{\bullet}$ which can then react with organic materials, leading to degradation of organic compounds and a drop in the measured current from the composite due to the redox chemistry consuming some of the electrons and electron holes.[14,15]
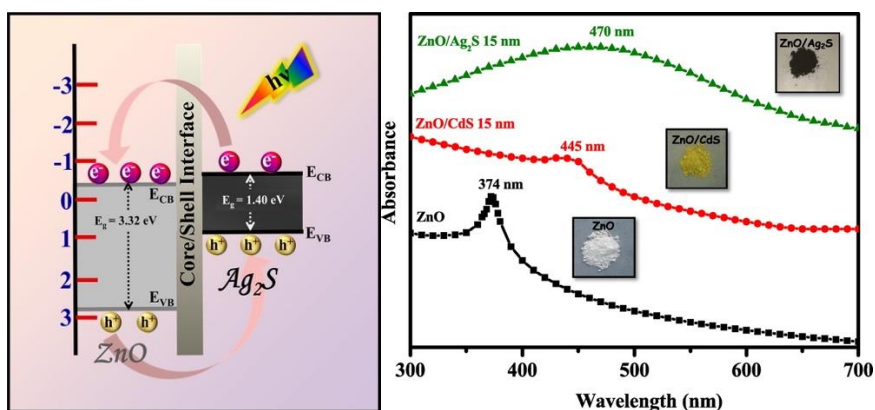
Figure 1.1: On left, schematic showing mechanism of action for Ag_2S sensitized ZnO. On right, absorbance spectrum of naked ZnO nanorods, as well as ZnO nanorods with 15 nm thick coatings of CdS and Ag_2S. Adapted with permission from Khanchandani, S.; Srivastava, P. K.; Kumar, S.; Ghosh, S.; Ganguli, A. K. *Inorg. Chem.* **2014**, *53* (17), 8902-8912. Copyright 2014 American Chemical Society.

In bioimaging, luminescent molecules that emit in the second near-infrared window (NIR-II, 1000 – 1400 nm) are desired because of the improved signal-to-noise ratio when compared to fluorophores that emit in the first near-infrared window (NIR-I, 750 – 850 nm), where there is interference with the signal produced by the fluorophores due to the autofluorescence of the living body.[12,16-20] Ag_2S is known to be minimally cytotoxic[12,17-19] and quantum dots of Ag_2S can be synthesized in the aqueous phase,[17,18] demonstrating that they can easily enter and leave the body. The emission of Ag_2S quantum dots is also tunable, as modulation of the quantum dot size will change the emission wavelength, with larger cores emitting at longer wavelengths.[12,18,20] Emission wavelengths as low as 624 nm to as high as ~1200 nm were attainable, showing potential broad applicability in NIR bioimaging.[12,18,20]

While silver containing quantum dots are of research interest, to enhance their usefulness it is necessary to be able to finely control their composition, size, and surface chemistry. For this, such nanomaterials have to be monodisperse and atomically precise in nature to allow for changes in the material to be measured with precision.

1.3 Silver Nanoclusters

The term nanocluster was first used in 1989 by Steigerwald and Brus[21] for the purpose of describing quantum dots as 'semi-conductor nanoclusters' but has now come to define clusters of atoms, usually stabilized by periphery ligands, where the cluster core typically has a diameter of less than 2 nm.[11] The most well-known nanoclusters have cores composed of noble metals, particularly group 11 metals (coinage metals; Cu, Ag, Au) as these are particularly well suited materials due to their metallophilic interactions, which more easily overcome the repulsive force between cationic atoms in the cluster core.[22] Often to aid in the self-assembly of these materials, an anionic template is used around which a layer of metal ions assembles with further growth accomplished by metallophilic interactions as well as the presence of stabilizing ligands.[22] Due to the flexibility in their coordination modes, chalcogenides (E^{2-}, E = O, S, Se, Te) and chalogenolates ($R-E^{1-}$) are often used for anionic templates and stabilizing ligands, respectively.[22] In addition to simple chalcogenide templates, polyanionic templates such as the sulfate anion or polyoxometalates (POMS) have also been successfully used in the synthesis of nanoclusters.[23,24] Nanocluster materials are diverse in their core architectures and optical properties, and synthetic methods used to obtain one nanocluster are often not easily modifiable to target another species.[22] Nanocluster materials are monodisperse and atomically precise, meaning their size and composition can be exactly measured and modified so their structural chemical properties can be understood on a fundamental level.[25]

As described above, Ag_2S nanomaterials are of interest due to their photoluminescent and semiconductor properties in combination with their low inherent toxicity. Ag_2S nanoclusters have also been synthesized and characterized. As nanocluster materials are studied mainly for their luminescent properties,[11] applications in imaging and responsive materials come to mind. The first luminescent Ag_2S nanocluster synthesized and structurally characterized was $[Ag_{62}S_{13}(S^tBu)_{32}](BF_4)_4$ (**I**) in 2010.[26] (**I**) is centrosymmetric and consisted of an $[Ag_{14}S_{13}]$ core and the shell consisted of 2 layers of 12 silver(I) ions in the lower layer and 36 silver(I) ions on the nanocluster surface, with each thiolate bridging 3 silver centres.[26] This structure is shown in **Figure 1.2**. Nanocluster (**I**) luminesced red

intensely in both the solid state and in solution at 621 nm and 613 nm, respectively where solutions were demonstrated to be photostable for months.[26]
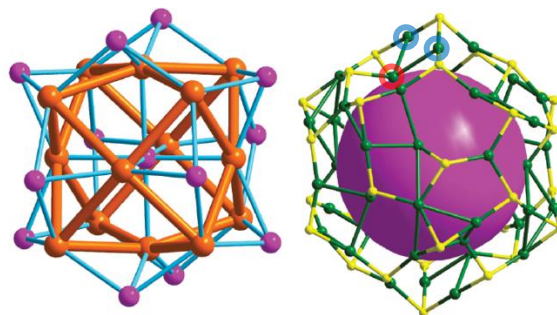
Figure 1.2: Structure of $[Ag_{62}S_{13}(S^tBu)_{32}](BF_4)_4$ (I), where surface ^tBu are omitted for clarity. The $[Ag_{14}S_{13}]$ core is shown on the left, where Ag^+ ions are orange and the S^{2-} are purple. To the right, the $[Ag_{48}(S^tBu)_{32}]$ is shown around a simplified core represented by a purple sphere. Ag^+ is here represented by green spheres, and the S^- from the thiolates is represented by yellow sphere. Though hard to discern, the 2 layers in the shell can be seen in that some Ag^+, such as the one outlined in red, clearly sit lower relative to surrounding Ag^+, outlined in blue. Adapted with permission from Li, G.; Lei, Z.; Wang, Q.-M. *J. Am. Chem. Soc.* **2010**, *132* (50), 17678-17679**.** Copyright 2010 American Chemical Society.

A more recent example of an interesting luminescent nanocluster is $[Ag_{50}S_7(SC_6H_4F)_{36}(dppp)_6] \cdot 4\,DMI$ (**II**, where dppp = 1,3-bis(diphenylphosphino)propane and DMI = 1,3-dimethyl-2-imidazolidinone), which was highly unusual in that while high-nuclearity nanoclusters tend to display thermal instability, (**II**) can be heated to 120 °C before any noticeable change happened in the powder X-ray diffraction pattern of the material, at which point the DMI solvent was lost.[27] The material shows no degradation upon being heated to 140 °C.[27] The structure of (**II**) is illustrated in **Figure 1.3**. Solvent-free crystals of (**II**), $[Ag_{50}S_7(SC_6H_4F)_{36}(dppp)_6]$ (**IIa**), displayed thermochromic activity and could be reversibly cooled to -160 °C where absorbance at 525 nm made the crystals appear yellow, and heated to 140 °C where absorbance at 565 nm made them appear dark red, for at least 4 cycles without degradation.[27] Thermochromic activity has been used in

applications such as anti-counterfeiting, smart windows, and thermal sensors.[27] Additionally, (**IIa**) displayed reversible piezochromic (pressure induced colour change) activity, with an absorption onset of 586 nm at room temperature and atmospheric pressure that could be shifted to 670 nm at 7.5 GPa, changing the observed colour of the material from orange-red to deep red.[27]
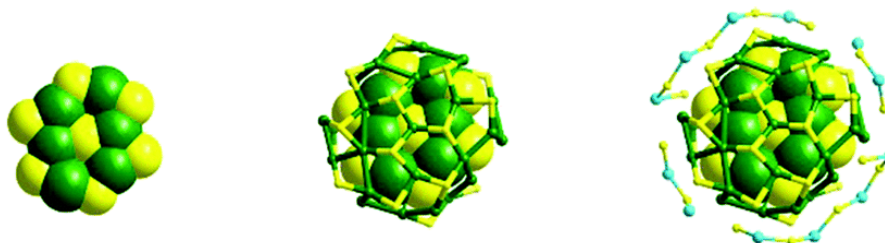
Figure 1.3: $[Ag_{50}S_7(SC_6H_4F)_{36}(dppp)_6] \cdot 4$ DMI (II) is composed of a Ag_6S_7 core (shown on the left, Ag = green, S = yellow) encased within a $Ag_{32}S_{22}$ shell (shown with ball and stick framework in the middle), which is further encased by a single layer of $Ag_{12}S_{14}$ about the equator (shown with outermost ring on right, where teal = Ag and S = yellow).[27] Surface C_6H_4F and dppp ligands are omitted for clarity. Used with permission of The Royal Society of Chemistry, from Thermochromism and piezochromism of an atomically precise high-nuclearity silver sulfide nanocluster, by Sun, Q.-Q.; Li, Q.; Li, H.-Y.; Zhang, M.-M.; Sun, M.-E.; Li, S.; Quan, Z.; and Zang, S.-Q., published in Chemical Communications, vol. 57, issue 19, 2021; permission conveyed through Copyright Clearance Center, Inc.

Though nanoclusters are studied primarily for their luminescent properties and structures, some nanoclusters also display semiconductor properties.[24] One example is the multishell nanocluster, $[SO_4@Ag_{78}S_{15}(C_5H_9S)_{27}(CF_3CO_2)_{12}](CF_3CO_2)_7$ (**III**), the structure of which is described in **Figure 1.4**. The simple polyanionic sulfate template used in the synthesis was crucial for obtaining the cluster, as larger polyoxometallate templates of the same charge did not yield the same complex.[24] Nanocluster (**III**) absorbed broadly in the UV and visible light regions, like other semiconductor nanomaterials such as quantum dots. A bandgap of 1.40 eV was estimated for (**III**) from a diffuse optical reflection spectrum, which gave this atomically precise nanocluster an equivalent bandgap to the one of narrow

semi-conductor Ag_2S quantum dot discussed earlier.[13, 24] Since this narrow bandgap seems to arise from the structure of the cluster core rather than the ligand,[24] the nanocluster could offer the appealing narrow bandgap properties needed for applications in photovoltaics while still having a surface which can be precisely modified to further tailor it to this application.
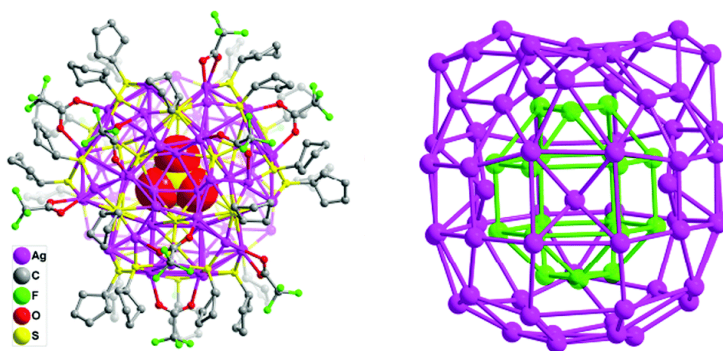
Figure 1.4: $[SO_4@Ag_{78}S_{15}(C_5H_9S)_{27}(CF_3CO_2)_{12}](CF_3CO_2)_7$ (**III**) consists of a sulfate anionic template within a Ag_{18} inner shell, which sits within and is connected to an $[Ag_{60}(C_5H_9S)_{27}]$ shell via 15 sulfide anions.[24] The complete molecular structure is shown on the left, and the Ag_{18} and Ag_{60} shells are more clearly illustrated on the left using green and purple spheres, respectively.[24] Used with permission of The Royal Society of Chemistry, from Small size yet big action: a simple sulfate anion templated a discrete 78-nuclearity silver sulfur nanocluster with a multishell structure, by Cheng, L.-P.; Wang, Z.; Wu, Q.-Y.; Su, H.-F.; Peng, T.; Luo, G.-G.; Li, Y.-A.; Sun, D.; and Zheng, L.-S., published in Chemical Communications, vol. 54, issue 19, 2018; permission conveyed through Copyright Clearance Center, Inc.

Nanoclusters have a diverse range of core architectures and properties based on those structures. While properties such as the luminescence, stimuli driven chromatic response, and narrow electronic band structure discussed above which arise from the core structure of the nanocluster are important, the surface chemistry of the nanocluster can also play an important role in determining its overall properties, such as a nanocluster's UV-Vis. absorbance profile, luminescence, and electrochemical activity.

1.4 Surface Ligands and Modification in Nanoparticles and Nanoclusters

Surface ligands can have a strong effect on the physical properties of the nanocluster core, as demonstrated by Bakr *et al.*[28,29] First, in 2015, the Bakr group showed that the core of a mixed silver(0)/(I) nanocluster protected with thiolates can be grown and shrunk via ligand exchange.[28] It was even shown to be reversible in one case, where $[Ag_{35}(SG)_{18}]$ (**IVa,** SG = glutathionate $(C_{10}H_{16}N_3O_6S^-)$) was converted to $[Ag_{44}(4\text{-}FBT)_{30}]$ (**IVb,** 4-FBT = 4-fluorobenzenethiolate $(FC_6H_4S^-)$).[28] The conversion from (**IVb**) back to (**IVa**) proceeded slowly as metastable intermediates of $[Ag_{37}(SG)_{21}]$ and $[Ag_{36}(SG)_{20}]$ were generated alongside (**IVa**), but these metastable intermediates converged to (**IVa**) when left at a cool temperature for an extended period. [28] This reversible size control process is illustrated in **Figure 1.5**. Exchange with a varied array of ligands showed that the silver core size is highly tunable, and nanoclusters with up to ~200 silver atoms at the core were obtained when the SG in (**IVa**) was exchanged with cyclohexanethiolate $(C_6H_{11}S^-)$, resulting in $Ag_{\sim200}(SC_6H_{11})_{\sim70}$.[28] While the formula for the cluster could not unambiguously confirmed as being atomically precise due to an inability to characterize it via electrospray ionization mass spectrometry, the authors noted that the products still retained nanocluster characteristics (non-plasmonic absorbance) and matrix-assisted laser desorption/ionization mass spectrometry indicated that products are monodisperse.[28] However, agglomeration can also occur which lead to nanoparticle rather than nanocluster materials, such as when SG was exchanged for *p*-thiobenzoic acid $(HSC_6H_4CO_2H)$, which resulted in a compound which displayed optical properties characteristic of silver nanoparticles. [28]

[Ag$_{35}$(SG)$_{18}$] (**IVa**)

[Ag$_{44}$(4-FBT)$_{30}$] (**IVb**)

Metastable [Ag$_{37}$(SG)$_{21}$] and [Ag$_{36}$(SG)$_{20}$]
Intermediates and [Ag$_{35}$(SG)$_{18}$] (**IVa**)
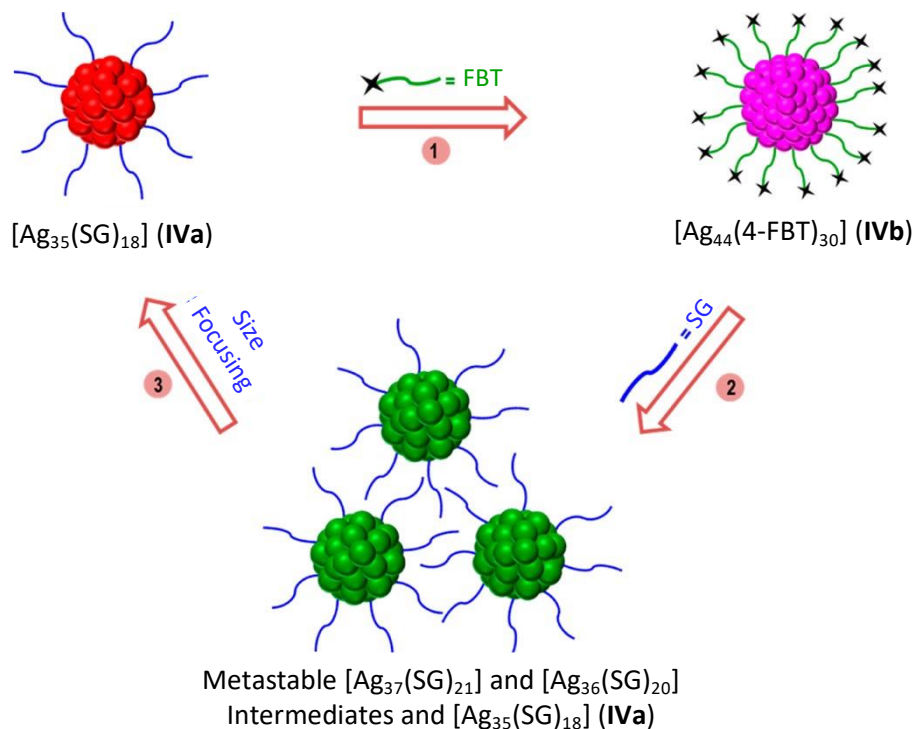
Figure 1.5: Bakr *et al.* demonstrated that [Ag$_{35}$(SG)$_{18}$] (**IVa**) can be converted to [Ag$_{44}$(4-FBT)$_{30}$] (**IVb**) in a quick, one-step ligand exchange reaction, and back to (**IVa**) via another ligand exchange where metastable intermediates are generated but converge to (**IVa**) when cooled at 4 °C for 6 hr.[28] Adapted with permission from Bootharaju, M. S.; Burlakov, V. M.; Besong, T. M. D.; Joshi, C. P.; AbdulHalim, L. G.; Black, D. M.; Whetten, R. L.; Goriely, A.; Bakr, O. M. *Chem. Mater.* **2015**, *27* (12), 4289-4297. Copyright 2015 American Chemical Society.

The Bakr group further demonstrated that the composition of the nanocluster core is highly sensitive to the geometry of the protecting ligands in a 2016 paper where a ligand exchange between 4-FBT and 2,4-dimethylbenzenethiolate ((Me)$_2$C$_6$H$_4$S$^-$) allowed for reversible interconversion between the mixed silver(0)/(I) nanoclusters [Ag$_{44}$(SC$_6$H$_4$F)$_{30}$] (**Va**) and [Ag$_{25}$(SC$_6$H$_4$(Me)$_2$)$_{18}$] (**Vb**).[29] Ag$_{44}$ and Ag$_{25}$ nanoclusters are well known and have strikingly different core architectures where Ag$_{44}$ is constructed of a hollow Ag$_{12}$ icosahedron contained within a Ag$_{20}$ dodecahedron which is stabilized by six Ag$_2$(SR)$_5$ units, and Ag$_{25}$ consists of a non-hollow Ag$_{13}$ icosahedron protected with six Ag$_2$(SR)$_3$.[29]

These different core geometries lead to different optical properties, as illustrated by **Figure 1.6**.
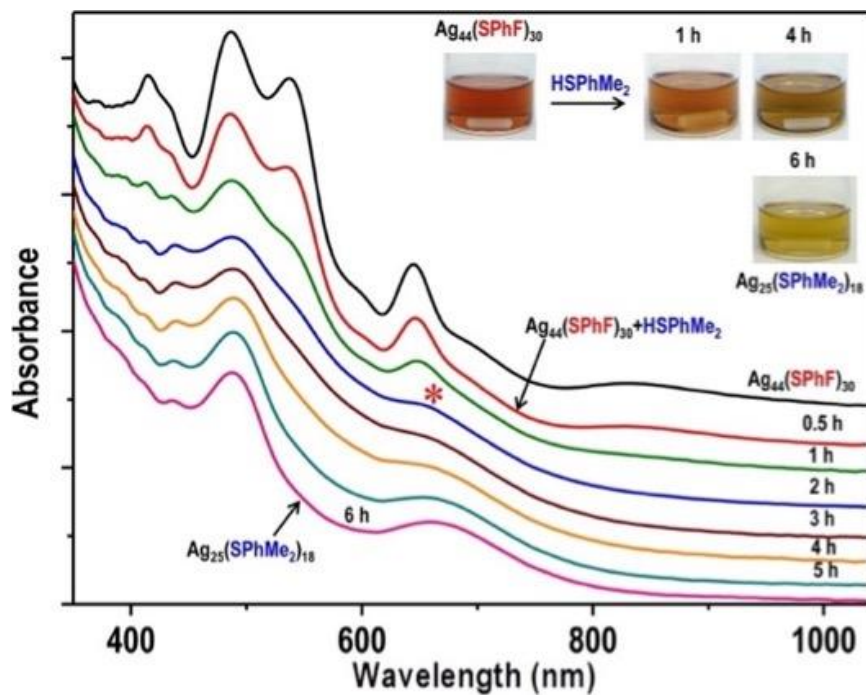
Figure 1.6: UV-Vis. spectrum of aliquots of an organic phase ligand exchange where [Ag$_{44}$(SPhF)$_{30}$] (**Va**) is converted to [Ag$_{25}$(SPhMe$_2$)$_{18}$] (**Vb**) by addition of the thiol HSC$_6$H$_4$(Me)$_2$.[29] The red asterisk indicated the broadening and bathochromic shift of the peak at 644 nm, indicating ligand exchange taking place.[29] The optical features of the Ag$_{44}$ cluster (peaks at 833, 537, and 644 nm) shift as the ligand exchange nears completion until only optical properties typical of Ag$_{25}$ clusters, namely a broad peak at ~650 nm and several small peaks below 450 nm, are observed.[29] Adapted with permission from Bootharaju, M. S.; Joshi, C. P.; Alhilaly, M. J.; Bakr, O. M. *Chem. Mater.* **2016**, *28* (10), 3292-3297. Copyright 2016 American Chemical Society.

A similar effect has been demonstrated for silver(I) thiolate nanoclusters. In 2018, Zang and coworkers synthesized an all silver(I) nanocluster using a thiolated polyhedral oligomeric silsesquioxane (POSS) ligand, which tethered six small Si$_8$O$_{12}$ silica nanoclusters to the surface of the resulting Ag$_{12}$ nanocluster, with salt counterions and

solvent filling in vacant coordination sites to give [$Ag_{12}(SSi_8O_{12}C_{31}H_{69})_6(CF_3COO)_6(THF)_6$] (**VIa**).[30] When crystallized out of a DCM/THF mixture the Ag_{12} core was ellipsoidal and the POSS ligands were arranged on the cluster surface in a pseudo-octahedral arrangement (**Figure 1.7**).[30] However, the cluster could also be crystallized out of a DCM/acetone mixture to yield [$Ag_{12}(SSi_8O_{12}C_{31}H_{69})_6(CF_3COO)_6(C_3H_6O)_2$] (**VIb**) which had a Ag_{12} core which was significantly more spherical and more stable, and the POSS surface ligands adopted a quasi-octahedral arrangement (**Figure 1.7**).[30] The transformation between the two core and surface ligand configurations was reversible simply by immersing a sample of either cluster into the opposite coordinating solvent, and the different core-ligand arrangements gave differing physical properties such as hydrophobicity.[30] In short, the protecting ligands that reside at the nanocluster's surface often play a key role in determining the geometry and nuclearity of the core, which in turn determines the optical and physical properties intrinsic to the nanocluster.
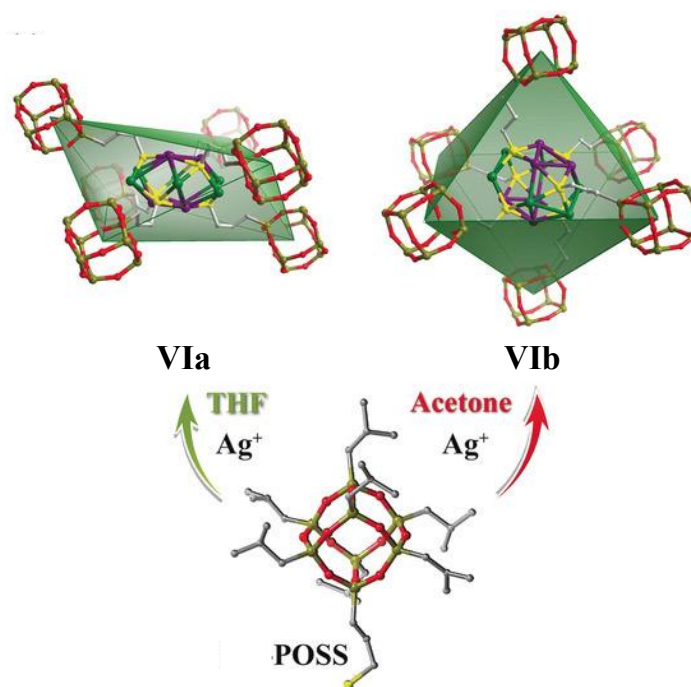
Figure 1.7: Coordinating solvent molecules can change the core structure of a of silver(I) thiolate nanocluster, as shown with the example of $[Ag_{12}(SSi_8O_{12}C_{31}H_{69})_6(CF_3COO)_6(THF)_6]$ (**VIa**) and $[Ag_{12}(Ssi_8O_{12}C_{31}H_{69})_6(CF_3COO)_6(C_3H_6O)_2]$ (**VIb**) where the only change in the synthetic method was whether THF or acetone was used as a solvent during crystallization.[30] **VIb** has a much more spherical core (width = 7.108 Å, height = 4.659 Å) than **VIa** (width = 7.657 Å, height = 3.814 Å).[30] Colouring: Peripheral Ag = green, trimer Ag = violet, S = yellow, C = gray, Si = dark yellow, O = red. Hydrogen, CF_3COO, and coordinating solvents have been omitted for clarity. Adapted with permission from Li, S.; Wang, Z.-Y.; Gao, G.-G., Li, B.; Luo, P.; Kong, Y.-J.; Liu, H.; Zang, S.-Q. *Angew. Chem. Int. Ed.* **2018**, *57* (39), 12775–12779. Copyright 2018 Wiley-VCH Verlag GmbH & Co. KGaA, Weinheim**.**

Surface ligands can also introduce new functionalities into nanocluster materials. This was shown over a decade ago with the surface functionalization of silver thiolate and copper thiolate clusters with ferrocenyl ligands, thus creating nanocluster materials with redox

active surfaces.[31-35] Previous work in our group has focussed on installing functional thiolate ligands onto the surfaces of gold and silver nanometer sized clusters,[31,36] due to the ease of creating functional and structurally diverse making them a class of ligand that is easy to tailor with an application of the resulting cluster in mind.[28,37-40] However, it is worth noting that thiolate ligands are often used in silver nanocluster synthesis even if the thiolate ligand has no ostensible functionality, due to the strong stabilizing nature of the Ag-SR bond and flexible coordination modes of thiolate ligands.[33,39,40] Zang *et al.* demonstrated extensive surface modification of a silver(I) thiolate nanoclusters in 2018 with a series of papers, two of which will be discussed for illustrative purposes as in both cases non-functional thiolates (tert-butyl thiolate and phenylmethanethiolate) were used to create a stable silver(I) cluster while the functionality on the cluster surface came from the use of functionalized carboxylate or pyridine ligands.[41,42]

In the first instance, a remarkably stable framework underwent ligand exchange, causing weakly coordinating nitrate surface ligands on the $[(CO_3)@Ag_{20}(S^tBu)_{10}(NO_3)_8(DMAc)_4]$ (**VII**) nanocluster to be displaced with a variety of carboxylate ligands without changing the morphology or nuclearity of the core (**Figure 1.8**).[41] Complete ligand exchange with a room-temperature fluorescent carboxylate, alrestatin ($C_{12}H_6O_2NCH_2COOH$), allowed for the non-fluorescent cluster precursor to attain room-temperature fluorescence when ligand exchange was performed, yielding $[(CO_3)@(Ag_{20}(S^tBu)_{10}(C_{12}H_6O_2NCH_2COO)_8(MeCN)_4]$ (**VIIa**).[41] Of note is that (**VIIa**) had a green emission at 513 nm with a quantum yield of 6.36% and lifetime of emission of 19.29 ns, which differs from the free carboxylic acid substantially (λ_{em} = 450 nm, lifetime of 6.46 ns), implicating a mixture of metal-to-ligand and ligand-to-ligand charge transfers, as well as $\pi - \pi$ stacking interactions between nanoclusters in the solid state, meaning that the fluorescence of the cluster is unique and longer lived compared to the free ligand.[41] In addition to this, ligand exchange with a ferrocenyl carboxylate installed an electrochemically active surface onto the electrochemically inert Ag_{20} core, as shown by the cyclic voltammograms obtained wherein the Ag_{20} nanocluster with the ferrocenyl functionalized surface is the only cluster that showed any response.[41] Of particular interest due to their rarity and synthetic difficulty,

chiral silver(I) thiolate nanoclusters were synthesized by partial ligand exchange of the nitrates in (**VII**) with enantiopure amino acids, with L-/D-alanine, L-/D-valine, and L-/D-proline being employed.[41] This allowed the nanoclusters to respond to chiral stimuli, as shown by the circular dichroism measurements in the paper.[41]
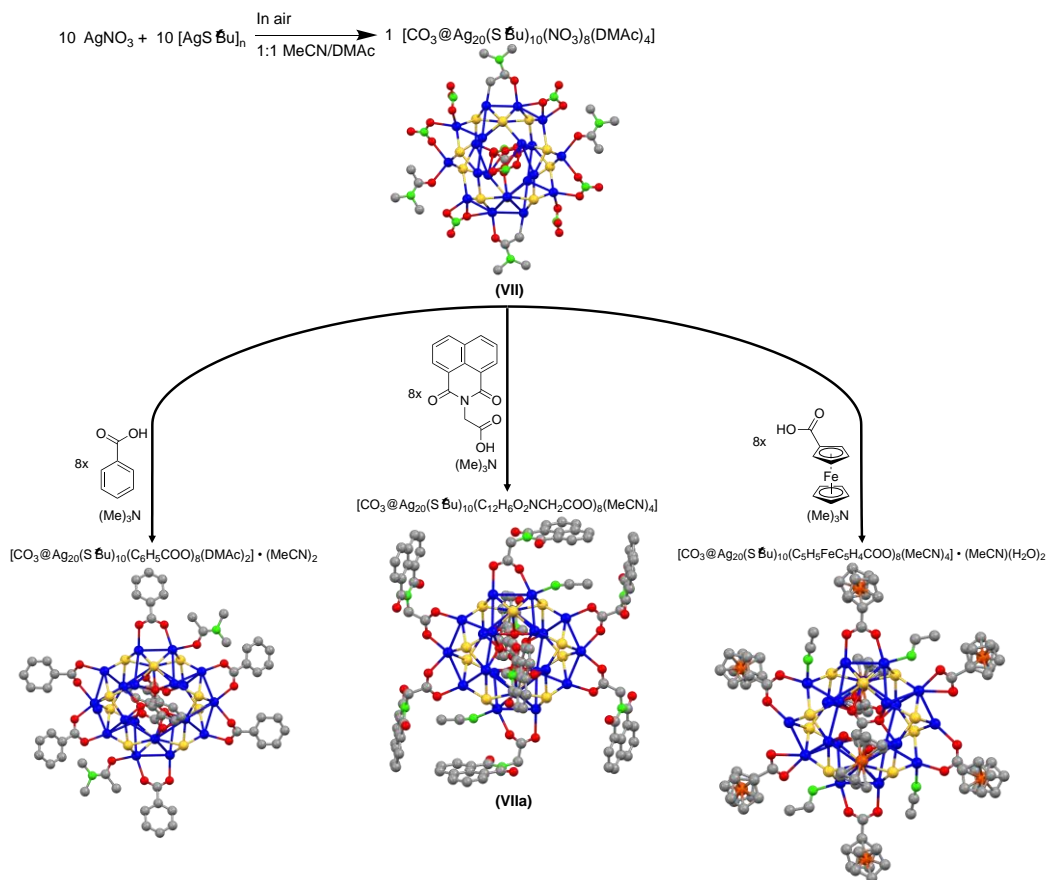
Figure 1.8: Reaction carried out by Gao and Zang *et al.*[42] to obtain a carbonate templated silver(I) thiolate nanocluster with nitrate ligands, and subsequent ligand exchange reactions used to change the cluster surface while retaining the same cluster core. For illustrative purposes hydrogen atoms, t-butyl groups, and lattice solvents are not shown. Colouring; grey = C, green = N, red = O, yellow = S, orange = Fe, blue = Ag.

In the second instance, a direct synthesis method was used where functionalized pyridinyl ligands were introduced into a reaction mixture consisting of AgO_2CCF_3 and silver(I)

phenylmethanethiolate.[42] Since the pyridinyl ligands were functionalized far from the point of ligation and there were no substantial electronic differences between ligands, the nanocluster cores were all identical even when the pyridinyl ligand was changed.[42] Each cluster had the general formula $[Ag_{12}(SCH_2C_6H_5)_6(CF_3COO)_6(L)_6]$ (L = pyridinyl ligand, **VIII**), and the optical properties of the cluster were tailored according to which pyridinyl was coordinated.[42] For example, when the ligand was changed from pyridine (on **VIIIa**, **Figure 1.9**) to 4-(9-anthracenyl)-pyridine (on **VIIIb**) to 4-[4-(1,2,2-triphenylethenyl)phenyl]-pyridine (on **VIIIc**), the emission properties of the solid changed from λ_{em} = 610 nm at 83 K, to a broad emission at λ_{em} = 545 at 293 K, to λ_{em} = 490 nm at 293 K.[42] Of note with regards to the **VIIb** is that when the nanocluster was dissolved, the broad emission peak disappeared and two sharp peaks at 400 nm and 418 nm appeared instead.[42] This suggests the presence of an excimer due to $\pi - \pi$ stacking in the anthracenyl moieties in the solid state upon illumination, which was disturbed when the nanocluster was dispersed in solution.[42] This excimer formation in the solid state could create a dually emissive material, where the emission due to the excimer and emission due to the core and interactions between the core and the ligands, can be tuned independently of each other, illustrating how useful surface functionalization is to tailoring applicability of nanocluster materials.[42]
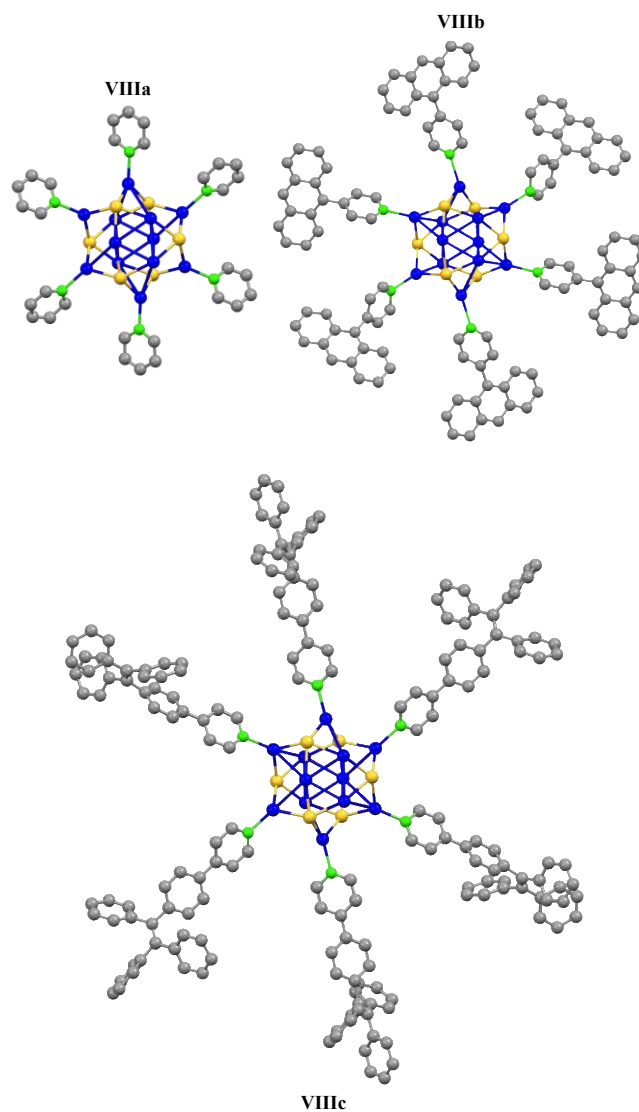
Figure 1.9: Molecular structures of [Ag$_{12}$(SCH$_2$C$_6$H$_5$)$_6$(CF$_3$COO)$_6$(NC$_5$H$_5$)$_6$] (**VIIIa**), [Ag$_{12}$(SCH$_2$C$_6$H$_5$)$_6$(CF$_3$COO)$_6$(NC$_5$H$_4$C$_{14}$H$_9$)$_6$] (**VIIIb**), and [Ag$_{12}$(SCH$_2$C$_6$H$_5$)$_6$(CF$_3$COO)$_6$(NC$_5$H$_4$C$_{26}$H$_{21}$)$_6$] (**VIIIc**).[42] Colouring; grey = C, green = N, red = O, yellow = S, blue = Ag. SCH$_2$C$_6$H$_5$ and CF$_3$COO ligands and hydrogen have been omitted for clarity.

These papers by the Zang group also demonstrate the two main routes to surface modification and functionalization used today. The first method being post-synthetic ligand exchanged, where weakly coordinating ligands are replaced with ligands which contain the desired functionality.[41] The benefit and drawback of this method, as shown by Bakr, is that the cluster core can undergo rearrangements that change the intrinsic physical and optical properties of the nanocluster.[25,26] The second method is through direct synthesis where the functionalized ligand is introduced directly into the reaction mixture to obtain a functionalized nanocluster.[42] The drawback of this approach is a loss of fine control over the nanocluster core composition, due to the unknown effect that different functionalized ligands will have towards targeting certain cores.[28] Additionally, some functionalized ligands have functional groups that are incompatible with the direct synthesis conditions. Another notable feature of these clusters is that though neither example takes advantage of a sulfide template which is well known is silver cluster chemistry from the when quantum dots were developed based on Ag_2S frameworks, both still take advantage of the chemistry between silver and sulfur in that both use thiolates as stabilizing ligands due to the strong Ag-S bond and coordination flexibility of the sulfur atom.

1.5   Azide Functional Groups and Click Chemistry

Click chemistry, a term coined by K. B. Sharpless in 1999,[43] describes reactions which are broadly applicable, have high yields, are stereospecific and produce few or no by-products, such that the products are easily isolated by standards procedures, such as column chromatography.[44] There are four types of chemical reactions which constitute click chemistry; of particular interest to the current work are cycloadditions such as the Huisgen's cycloaddition.[44] Huisgen's cycloaddition, shown in **Scheme 1.1**, is a well-known condensation between an alkyne and azide moiety to give 1,2,3-triazole linkages which join two organic groups, R and R', where one is typically a scaffold (such as a protein) and the other a desired functionality (such as a chromophore).[44] In this way, installation of an azide (N_3) functional group allows for easy and selective further modification of a material, since azides and alkynes are highly reactive with each other, but unreactive towards most other functional groups, with some notable exceptions.[44]

Poor Regioselectivity
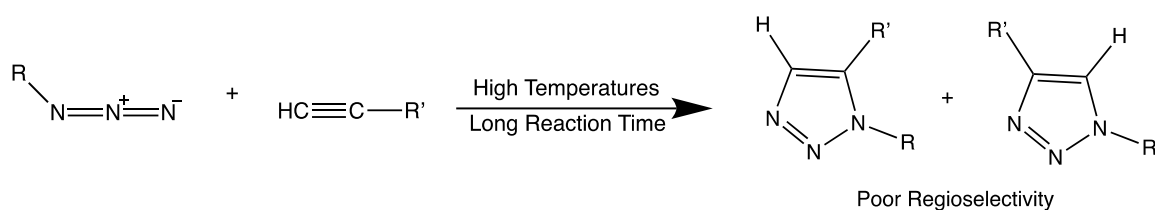
Scheme 1.1: Uncatalyzed Huisgen Cycloaddition between and azide and alkyne to form 1,4 and 1,5 traizoles.

The original Huisgen's cycloaddition is limited in its use by the stability of the alkyne, thus necessitating a high temperature and long reaction time to drive the reaction forward to completion that some R groups will not tolerate.[44] Additionally, there is a lack of regiospecificity between the 1,5-isomer and 1,4-isomer in the product.[44] Addition of a copper(I) catalyst, investigated separately by Sharpless and Meldal, improved the azide-alkyne cycloaddition by both activating the alkyne and templating the reacting groups so that only the 1,4-isomer is formed.[44] This copper-catalyzed azide-alkyne cycloaddition (CuAAC) reaction is the most popular metal ion catalyzed Huisgen cycloaddition and is used in chemical and biochemical syntheses for conjugation, due to its tolerance of a wide range of reaction conditions (aqueous or organic media, and ambient temperatures).[44] Another popular metal catalyzed azide-alkyne cycloaddition is that catalyzed by ruthenium(II) complexes, which selectively targets the 1,5-isomer when there is sufficient steric hindrance about the ruthenium metal centre, typically achieved by the presence of a pentamethylcyclopentadienyl ring.[44] In each case there are drawbacks, the most limiting for biological use being the possibility of introducing possibly toxic metals into an organism.[44] Another drawback in any chemical setting is the formation of side-products through interactions between redox active spectator molecules with the redox active metals.[44] In the specific case of copper, generation and maintenance of the copper(I) catalyst can be challenging due to the ease of oxidizing copper(I) to copper(II), the incompatibility between some functional groups and reducing agents to obtain copper(I) from copper(II), and the inefficiency of generating the copper(I) catalyst from disproportionation between copper(0) and copper(II).[44] In the specific case of ruthenium,

the relatively more expensive catalyst is more reactive towards oxygen and less reactive towards substrates, meaning the azide-alkyne cycloaddition must be carried out under an inert atmosphere at either high temperatures or longer reaction times.[44] Additionally, the catalyst is only efficient in aprotic solvents.[44]

Due to the limitations and drawbacks of metal catalyzed azide-alkyne cycloadditions, metal free alternatives where the alkyne is still activated as to avoid the high temperatures and reaction times required by the original Huisgen cycloaddition have been investigated.[44,45] The strain-promoted azide-alkyne cycloaddition (SPAAC) between a strained cyclooctyne and organic azide advanced by Bertozzi and Agard[45] based on earlier work by Wittig and Krebs is of particular interest to the current work.[44] The ring strain in cyclooctyne destabilizes the alkyne, lowering the energy of the LUMO and raising the energy of the HOMO, activating it so that the transition state is easy to achieve, and the reaction can proceed at room temperature efficiently without the need for a catalyst.[44,45] This approach has already been used for labeling biomolecules and living cells, as well as DNA and RNA synthesis,[44] and several strained alkynes have been developed for this purpose including cyclooctynes[45] (including difluorinated cyclooctynes, DIFO)[46], dibenzocyclooctynes (DIBO),[47] 6,7-dimethoxyazacyclooct-4-yne (DIMAC),[48] biarylazacyclooctynone (BARAC),[49] aza-dibenzocyclooctyne (DIBAC)[50] among many others (**Figure 1.10**). Each of these strained alkynes some with its own benefits, such as stability of the alkyne in DIBO,[47] increased hydrophilicity in DIBAC and DIMAC,[48,50] or having a high-yielding synthetic route like DIBAC,[50] though a general goal with each new generation of strained alkyne reagents is to increase ring strain thus leading to quicker reaction times and faster labelling of biomolecules while still being stable in biological enviroments.[51] The need for increased reaction speed comes from a desire to minimize use of excess strained alkyne reagents to drive the labelling to completion, and thus minimize the cost associated with synthesizing the strained alkyne and any associated toxicity.[51]
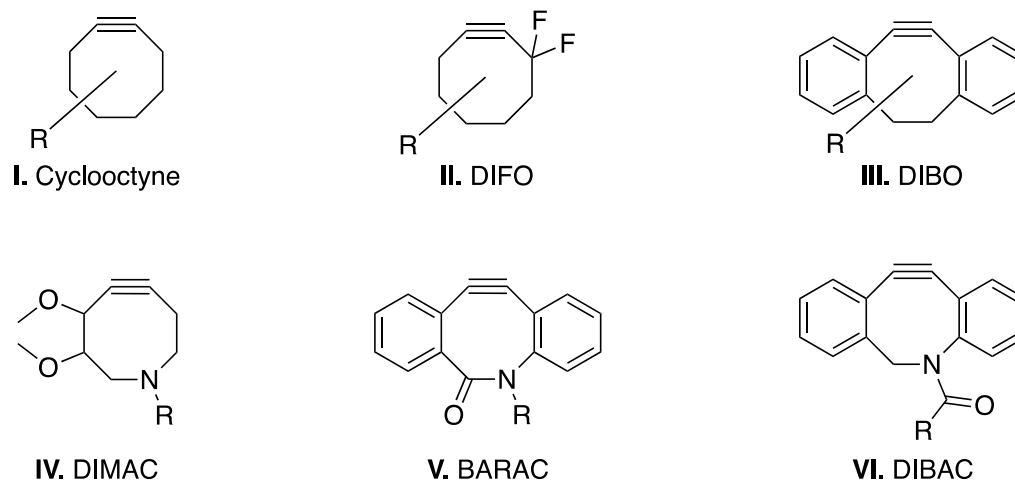
Figure 1.10: Chemical structures of cyclooctyne (**I**), difluorinated cyclooctyne (DIFO, **II**), dibenzocyclooctynes (DIBO, **III**), 6,7-dimethoxyazacyclooct-4-yne (DIMAC, **IV**), biarylazacyclooctynone (BARAC, **V**), aza-dibenzocyclooctyne (DIBAC, **VI**)

For the purposes of this project, (1α, 8α, 9α)-bicyclo[6.1.0]non-4-yn-9-ol (BCN, **Figure 1.11**) was chosen as a model strained alkyne due to its synthetic procedure that is high-yielding and uses commercially available chemicals and has the alcohol function that can be used as a handle for the attachment of functional payloads to the strained alkyne.[52] Other notable features of BCN include the increased ring-strain caused by the cyclopropyl group, giving it an increased reactivity compared to cyclooctyne and similar to other modified cyclooctyne systems, while at the same time being stable enough for long-term storage and prolonged exposure to thiols.[52] Additionally, BCN has been previously used as an organic linker on some nanomaterials. In 2012, an ethyl squaramyl-functionalized BCN (**Figure 1.11**) was used as a link to bind the biomolecule transferrin to quantum dots with a CdSe/ZnS core–shell structure that had been modified to have surface azide functionalities.[53] This demonstrated a modifiable method of binding still functional proteins to quantum dots which could be used to monitor the activity and uptake of the protein by, for example, cancer cells.[53] More recently, a BCN linker was used in heterogeneous catalysis to link a silica particle with azide functionalized shell to a diene in order to immobilize the resulting chiral rhodium catalyst on reaction of the diene-

functionalized silica particle with a chlorobis(ethylene)rhodium dimer, $[Rh(C_2H_4)_2Cl]_2$.[54] This heterogenous catalyst (**Figure 1.11**) could catalyze the asymmetric 1,4-addition reaction, one of the most important asymmetric C-C bond forming reactions, of phenylboronic acid to ethyl 4-methylcinnamate better than the homogenous catalyst owing to a site isolation effect preventing the catalytic rhodium metals from dimerizing, and the catalyst could be recovered from solution and reused 10 times without suffering loss of catalytic activity.[54] Taken all together, BCN is an easily synthesized and versatile linker which has already been employed in linking nanoparticle materials to important functionalities via the SPAAC reaction, and so would be a good candidate to use in this project.

I. exo-BCN (Ref. 52)

II. CdSe/ZnS Quantum Dot Linked to Transferrin via Ethyl Squaramate-Functionalized BCN, Schieber, Donnelly, Williams, Mulvaney *et al.*, **2012** (Ref. 53)

III. Silica/Polystyrene Nanoparticl Linked to Rh Catalyst via Diene-Functionalized BCN, Kobayashi *et al.,* **2021** (Ref. 54)
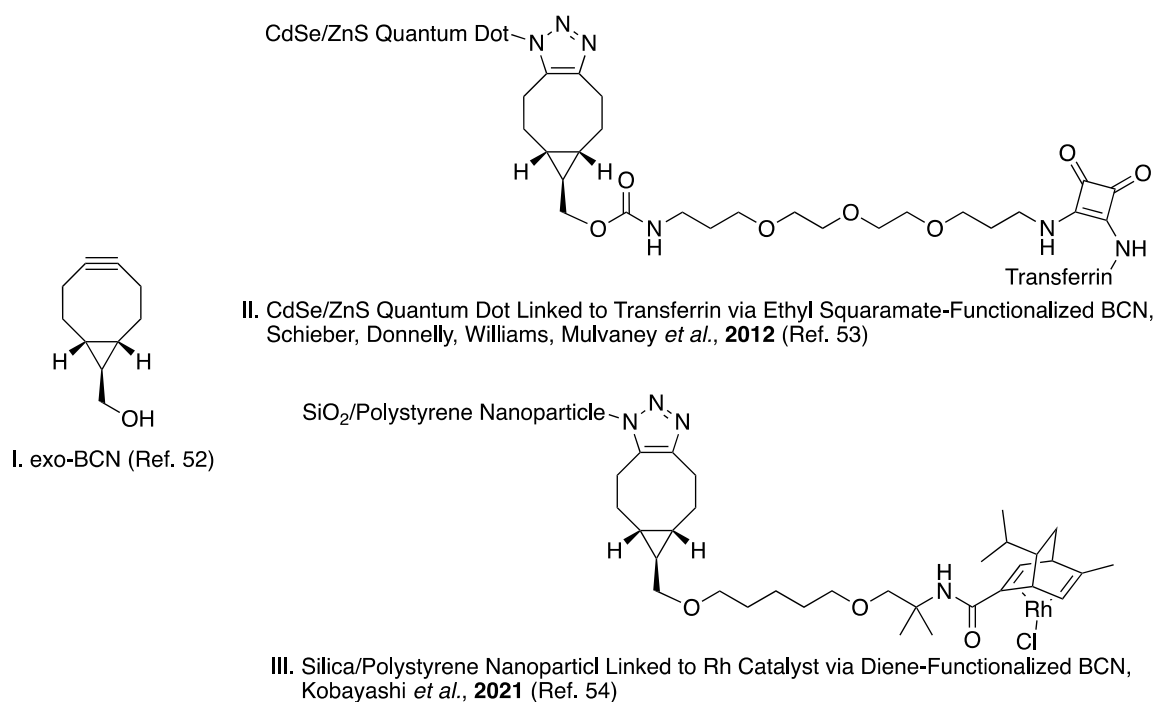
Figure 1.11: Chemical structures of (1α, 8α, 9α)-bicyclo[6.1.0]non-4-yn-9-ol (BCN, **I**),[52] ethyl squaramate-functionalized BCN linking a quantum dot to transferrin (**II**),[53] and diene-functionalized BCN linking a silica quantum dot to an immobilized rhodium catalyst (**III**).[54]

One key limitation to be mindful of when employing the use of azide functionalized ligands in the synthesis of nanocluster materials is the possibility to reducing the azide moiety via the Staudinger reaction (**Scheme 1.2**).[55] Commonly used stabilizing ligands, such as phosphanes and N-heterocyclic carbenes, should therefore be avoided during synthesis of an azide functionalised nanocluster, as their use can lead to side reactions and eliminate the intended surface modification,[55] though they may prove useful in obtaining an amine functionalized cluster on subsequent reaction of the azide functionalized cluster once it has been isolated.
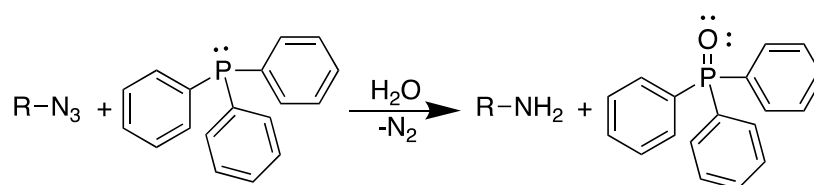
Scheme 1.2: Staudinger Reaction

1.6 Project Objectives

Post-assembly modification has been demonstrated by our group for gold nanoclusters based on the $[Au_{25}(SR)_{18}]^{0/-1}$ framework using stabilizing azide-functionalized thiolate ligands.[36] These gold nanoclusters were able to undergo cluster surface strain-promoted azide-alkyne click (CS-SPAAC) reactions in order to install (Z)-cyclooct-1-ene-5-yne and *exo*-bicyclo[6.1.0]non-4-yn-9-ylmethanol (BCN) on the surface of the nanocluster without changing the core configuration when the azidophenylethanethiol ligand was *para* or *meta* substituted.[36] There have been no reports of an analogous system based on a silver nanocluster framework, likely due to the synthetic challenges inherent in silver chemistry and in the assembly of silver nanoclusters where the use of stabilizing N-heterocyclic carbene and phosphine ligands is precluded due to their reactivity with azide functional groups. Similar to gold nanoclusters, silver nanoclusters show great potential in a variety of fields but are likewise hindered by a lack of easy post-assembly modifiability that can tailor their properties towards specific applications. To this end, we herein present the synthesis and characterization of silver(I) nanoclusters with azide functionalized surfaces,

and subsequent CS-SPAAC reactivity towards selected strained cycloalkynes. The development of the nanoclusters presented herein builds off the previously mentioned highly robust [(CO$_3$)@Ag$_{20}$(S^{t}Bu)$_{10}$(NO$_3$)$_8$(DMAc)$_4$] framework developed by Gao and Zang *et al.*, where the surface nitrates could be exchanged for carboxylic acids. To realize the goal of an azide functionalized silver(I) nanocluster, *m*-azidobenzoic acid and *p*-azidobenzoic acid were prepared from literature and used following the cluster synthesis reported by Gao and Zang *et al.* to afford the corresponding surface azide decorated silver(I) nanoclusters, [CO$_3$@Ag$_{20}$(S^{t}Bu)$_{10}$((*m*-N$_3$-C$_6$H$_4$COO)$_8$(DMF)$_4$] and [CO$_3$@Ag$_{20}$(S^{t}Bu)$_{10}$((*p*-N$_3$-C$_6$H$_4$COO)$_8$(DMF)$_4$] in a one-pot synthesis. As with the surface azide-functionalized gold nanoclusters previously reported by our group, the ability to undergo CS-SPAAC reactions was probed. In this case we utilized BCN, as well as a ferrocene functionalized version of BCN that takes advantage of the hydroxy group in BCN as a handle to introduce functionality.

Chapter 2 discusses in a manuscript format the synthesis and characterization of the first known clickable azide-functionalized silver nanoclusters by UV-Vis., FT-IR, and NMR spectroscopies, and SCXRD and XPS analysis. The click products of the azide-functionalized clusters with BCN and the ferrocene-functionalized BCN are also reported and characterized by UV-Vis., FT-IR, and NMR spectroscopies and XPS. From this investigation, the azide-functionalized silver nanoclusters are structurally characterized, allowing for the audience to see a refined molecular structure where the azide moiety is clearly present. Subsequent reactions with BCNs monitored by IR spectroscopy show that all azide moieties react completely, showing that all azide units are accessible for post-assembly modification as this project set out to demonstrate.

Chapter 3 provides an outlook on future work that can be investigated, such as other using strained alkynes that can deliver a functional payload for applications, other bioorthoganol click reactions that can be employed to create different linkages, and structural changes that can be made to give a greater variety of silver(I) thiolate clusters with reactive surfaces. Of particular interest here is the serendipitous discovery that the degree to which nitrate

ligands are replaced by carboxylate ligands can be finely controlled by the stoichiometry of the cluster synthesis, allowing for the isolation of silver(I) nanoclusters which retain nitrate ligands at specific positions. This can allow the creation of bifunctional materials since once functionality can be installed via CS-SPAAC while the other is installed via substitution of the remaining nitrate ligands for different carboxylate ligands. Other structural changes discussed include the possibility of functionalizing the stabilizing thiolate ligand and transforming the azide into other functional group with which linkages can be created (for example, obtaining the amine functionalized cluster via the Staudinger-Bertozzi ligation to create amide linkages).

1.7 References

1. Tropper, P. and Zori, C. *J. Archaeol. Sci.* **2013**, *40* (8), 3282-3292

2. Gordon, R. and Knopf, R. *J. Archaeol. Sci.* **2007**, *34* (1), 38-47

3. Meschel, S. V. *Jew. Bible Q.* **2019**, *47* (4), 217-224

4. Corbet, S.; O'Connor, F. *Finance Res. Lett.* **2021**, *39*, 101626

5. Benentuno, M. A. Silver. In *Metals and Alloys: Industrial Applications*. De Gruyter: Berlin, Germany, 2016; pp. 37-42

6. Satsuma, S. English Expansion into Spanish America and the Development of a Pro-Maritime War Argument. In *Britain and Colonial Maritime War in the Early Eighteenth Century: Silver, Seapower and the Atlantic.* Boydell & Brewer: Woodbridge, UK., 2013; pp. 15-36

7. Alexander, J. W. *Surg. Infect.* **2009**, *10* (3), 289-292

8. Medici, S.; Peana, M.; Nurchi, V. M.; Zoroddu, M. A. *J. Med. Chem.* **2019**, *62* (13), 5923-5943

9. Saxby, G. The Silver Halide Process. In *The Science of Imaging: An Introduction*, 2nd Ed. CRC Press: Boca Raton, FL, US, 2011; pp. 143-156

10. Medici, S.; Peana, M.; Crisponi, G.; Nurchi, V. M.; Lachowicz, J. I.; Remelli, M.; Zoroddu, M. A. *Coord. Chem. Rev.* **2016**, *327-328*, 349–359

11. Park, H. J.; Shin, D. J.; Yu, J. *J. Chem. Educ.* **2021**, *98* (3), 703-709

12. Zhang, Y.; Liu, Y.; Li, C.; Chen, X.; Wang, Q. *J. Phys. Chem. C* **2014**, *118* (9), 4918-4923

13. Liu, B.; Wang, D.; Zhang, Y.; Fan, H.; Lin, Y.; Jiang, T.; Xie, T. *Dalton Trans.* **2013**, *42* (6), 2232-2237

14. Zhang, Y.; Liu, B.; Wang, D.; Lin, Y.; Xie, T.; Zhai, J. *Mater. Chem. Phys.* **2012**, *133* (2-3), 834-838

15. Khanchandani, S.; Srivastava, P. K.; Kumar, S.; Ghosh, S.; Ganguli, A. K. *Inorg. Chem.* **2014**, *53* (17), 8902-8912

16. Li, C.; Zhang, Y.; Wang, M.; Zhang, Y. Chen, G.; Li, L.; Wu, D.; Wang, Q. *Biomaterials* **2014**, *35* (1), 393-400

17. Zhang, Y.; Hong, G.; Zhang, Y.; Chen, G.; Li, F.; Dai, H.; Wang, Q. *ACS Nano* **2012**, *6* (5), 3695-3702

18. Wang, C.; Wang, Y.; Xu, L.; Zhang, D.; Liu, M.; Li, X.; Sun, H.; Lin, Q.; Yang, B.; *Small* **2012**, *8* (20), 3137-3142

19.Du, Y.; Xu, B.; Fu, T.; Cai, M.; Li, F.; Zhang, Y.; Wang, Q. *J. Am. Chem. Soc.* **2010**, *132* (5), 1470-1471

20. Jiang, P.; Zhu, C.-N.; Zhang, Z.-L.; Tian, Z.-Q.; Pang, D.-W. *Biomaterials* **2012**, *33* (20), 5130-5135

21. Steigerwald, M. L.; Brus, L. E. *Annu. Rev. Mater. Sci.* **1989**, *19*, 471-495

22. Xie, Y.-P.; Jin, J.-L.; Duan, G.-X.; Lu, X.; Mak, T. C. W. *Coord. Chem. Rev.* **2017**, *331*, 54-72

23. Yan, B.-J.; Du. X.-S.; Huang, R.-W.; Yang, J.-S.; Wang, Z.-Y.; Zang, S.-Q.; Mak, T. C. W. *Inorg. Chem.* **2018**, *57* (9), 4828−4832

24. Cheng, L.-P.; Wang, Z.; Wu, Q.-Y.; Su, H.-F.; Peng, T.; Luo, G.-G.; Li, Y.-A.; Sun, D.; Zheng, L.-S. *Chem. Commun.* **2018**, *54* (19), 2361-2364

25. Fang, J.; Zhang, B.; Yao, Q.; Yang, Y.; Xie, J.; Yan, N. *Coord. Chem. Rev.* **2016**, *322*, 1-29

26. Li, G.; Lei, Z.; Wang, Q.-M. *J. Am. Chem. Soc.* **2010**, *132* (50), 17678-17679

27. Sun, Q.-Q.; Li, Q.; Li, H.-Y.; Zhang, M.-M.; Sun, M.-E.; Li, S.; Quan, Z.; Zang, S.-Q. *Chem. Commun.* **2021**, *57* (19), 2372-2375

28. Bootharaju, M. S.; Burlakov, V. M.; Besong, T. M. D.; Joshi, C. P.; AbdulHalim, L. G.; Black, D. M.; Whetten, R. L.; Goriely, A.; Bakr, O. M. *Chem. Mater.* **2015**, *27* (12), 4289-4297

29. Bootharaju, M. S.; Joshi, C. P.; Alhilaly, M. J.; Bakr, O. M. *Chem. Mater.* **2016**, *28* (10), 3292-3297

30. Li, S.; Wang, Z.-Y.; Gao, G.-G., Li, B.; Luo, P.; Kong, Y.-J.; Liu, H.; Zang, S.-Q. *Angew. Chem. Int. Ed.* **2018**, *57* (39), 12775–12779

31. Liu, Y.; Najafabadi, B. K.; Fard, M. A.; Corrigan, J. F. *Angew. Chem. Int. Ed.* **2015**, *54* (16), 4832-4835

32. Nitschke, C.; Wallbank, A. I.; Fenske, D.; Corrigan, J. F. *J. Cluster Sci.* **2007**, *18* (1), 131-140

33. MacDonald, D. G.; Corrigan, J. F. *Phil. Trans. R. Soc. A* **2010**, *368* (1915), 1455-1472

34. Wallbank, A. I.; Borecki, A.; Taylor, N. J.; Corrigan, J. F. *Organometallics* **2005**, *24* (5), 788-790

35. Nitschke, C.; Fenske, D.; Corrigan, J. F. *Inorg. Chem.* **2006**, *45* (23), 9394-9401

36. Gunawardene, P. N.; Martin, J.; Wong, J. M.; Ding, Z.; Corrigan, J. F.; Workentin, M. S. *Angew. Chem. Int. Ed.* **2022**, *61* (29), e202205194

37. Jin, R.; Zeng, C.; Zhou, M.; Chen, Y. *Chem. Rev.* **2016**, *116* (18), 10346−10413

38. Chen, Y.; Zeng, C.; Kauffman, D. R.; Jin, R. *Nano Lett.* **2015**, *15* (5), 3603−3609

39. Krebs, B.; Henkel, G. *Angew. Chem. Int. Ed.* **1991**, *30* (7), 769-788

40. Xie, Y.-P.; Jin, J.-L.; Duan, G.-X.; Lu, X.; Mak, T. C. W. *Coord. Chem. Rev.* **2017**, *331*, 54–72

41. Li, S.; Du, X.-S.; Li, B.; Wang, J.-Y.; Li, G.-P.; Gao, G.-G.; Zang S.-Q. *J. Am. Chem. Soc.* **2018**, *140* (2), 594-597

42. Li, Y.-L.; Zhang, W.-M.; Wang, J.; Tian, Y.; Wang, Z.-Y.; Du, C.-X.; Zang S.-Q.; Mak, T. C. W. *Dalton Trans.* **2018**, *47* (42), 14884-14888

43. Kolb, H. C.; Finn, M. G.; Sharpless, K. B. *Angew. Chem. Int. Ed.* **2001**, *40* (11), 2004−2021

44. Fantoni, N. Z.; El-Sagheer, A. H.; Brown, T. *Chem. Rev.* **2021**, *121* (12), 7122-7154

45. Agard, N. J.; Prescher, J. A.; Bertozzi, C. R. *J. Am. Chem. Soc.* **2004**, *126* (46), 15046-15047

46. Johnson, J. A.; Baskin, J. M.; Bertozzi, C. R.; Koberstein, J. T.; Turro, N. J. *Chem. Commun.* **2008**, 3064–3066

47. Ning, X.; Guo, J.; Wolfert, M. A.; Boons, G.-J. *Angew. Chem. Int. Ed.* **2008**, *47* (12), 2253–2255

48. Sletten, E. M.; Bertozzi, C. R. *Org. Lett.* **2008**, *10* (14), 3097–3099

49. Jewett, J. C.; Sletten, E. M.; Bertozzi, C. R. *J. Am. Chem. Soc.* **2010**, *132* (11), 3688–3690

50. Debets, M. J.; van Berkel, S. S.; Schoffelen, S.; Rutjes, F. P. J. T.; van Hest, J. C. M.; van Delft, F. L. *Chem. Commun.* **2010**, *46* (1), 97–99

51. Patterson, D. M.; Nazarova, L. A.; Prescher, J. A. *ACS Chem. Biol.* **2014**, *9* (3), 592–605

52. Dommerholt, J.; Schmidt, S.; Temming, R.; Hendriks, L. J. A.; Rutjes, F. P. J. T.; van Hest, J. C. M.; Lefeber, D. J.; Friedl, P.; van Delft, F. L. *Angew. Chem. Int. Ed.* **2010**, *49* (49), 9422 –9425

53. Schieber, C.; Bestetti, A.; Lim, J. P.; Ryan, A. D.; Nguyen, T.-L.; Eldrige, R.; White, A. R.; Gleeson, P. A.; Donnelly, P. S.; Williams, S. J.; Mulvaney, P. *Angew. Chem. Int. Ed.* **2012**, *51* (42), 10523 –10527

54. Kuremoto, T.; Sadatsune, R.; Yasukawa, T.; Kobayashi, S. *ACS Catal.* **2021**, *11* (22), 14026–14031

55. Lohani, C. R.; Taylor, S. D. *Org. Lett.* **2016**, *18* (17), 4412-4415

<div align="center">Chapter 2</div>

2   Ag$_{20}$ Nanoclusters with Surface Azides as an Easily Functionalized Platform for Diverse Chemical Applications

2.1   Introduction

Nanocluster materials have attracted intense research interest since the 1990's.[1,2] Nanoclusters are typically made of noble metals and have core diameters of less than 2 nm, giving them intermediate properties between bulk metals and small metal molecules.[1,3,4,5] Atomic precision is a key feature of nanoclusters, allowing for relationships between the structure, composition, and size-dependant optical and electronic properties to be monitored and tailored atom-by-atom. Nanoclusters have affected several different fields and are potential candidates for applications in photovoltaics[6], sensing[7], imaging[8], and as building blocks in metal-organic frameworks[9].

One key challenge hindering broad applicability of nanoclusters is the lack of easy post-assembly modification.[10] Surface modification to tailor the nanocluster towards specific properties involves the delicate interplay between the functionalized surface ligands and the characteristics of the cluster core. Simply changing one ligand for another can result in a core with a different structure or composition because of different stabilizing effect ligands have, and thus altered physiochemical properties.[11] Progress has been made in this area using direct synthesis methods[12] as well as by employing post-synthetic ligand exchange[11]. Both techniques have some limitations in terms of targeting specific nanocluster frameworks and retaining compositions and structural properties, including not being able to target certain cores via direct synthesis[13], property altering core rearrangements during ligand exchange[11], or incompatibility between the desired ligand and synthetic route to certain nanocluster frameworks (i.e. reduction).

One way to circumvent these limitations is to incorporate post-assembly modifiability onto the surface ligands. This approach was investigated recently by our group[14,15] and Khang

and coworkers,[10] for several gold clusters with reactive cluster surface azide functionalities. Azides are selectively reactive with certain substrate classes and can form a variety of linkages like triazoles (with alkynes)[16], iminophosphoranes (with phosphines)[17], or amides (with ortho-ester arylphosphines)[18]. Due to this, azides are also used in a variety of bioorthoganol reactions that couple two moieties in complex biological environments without disturbing biochemical pathways or being destroyed by biological reagents.[19] Most bioorthoganol reactions are examples of click chemistry, as they proceed quickly under mild conditions with easily separable by-products,[19,20] which is advantageous for clusters with clickable functions as it allows for easy removal of excess reagents and the mild conditions make core rearrangements less likely. Of particular interest is the ability to perform cluster-surface strain-promoted azide alkyne cycloaddition (CS-SPAAC) reactions because it eliminates the need for a copper catalyst which could be cytotoxic in biological systems[19] and could participate in metal exchange with the silver core which modifies the core properties of the cluster[21]. With such a wide variety of possible substrate classes it is possible to build a large library of functionalized clusters from the same azide-parent nanocluster while preserving the properties of the metal-based core.

Gold thiolate nanoclusters are highly stable and incorporate thiolate ligands, which can be easily designed to include azide moieties.[22] The superatom model predicts that silver thiolate nanoclusters should be stable,[23] and extending CS-SPAAC research to these systems presents a boon because silver is comparatively less expensive than gold. Gao and Zang *et al.* developed a remarkably robust platform based on a templated silver thiolate nanocluster, $[(CO_3)@Ag_{20}(S^tBu)_{10}(DMF)_6(NO_3)_8]$, reported by Sun *et al.*[24], where the cluster surface can be easily changed by introducing carboxylic acids to displace the surface nitrates, while retaining the same Ag_{20} core assembly.[25] Building off this, we report two novel regioisomeric Ag_{20} silver nanoclusters decorated with aryl azide surfaces obtained in a one-pot synthetic approach. The nanoclusters $[CO_3@Ag_{20}(S^tBu)_{10}(m\text{-}N_3\text{-}C_6H_4COO)_8(DMF)_4]$ (**1-*m***) and $[CO_3@Ag_{20}(S^tBu)_{10}(p\text{-}N_3\text{-}C_6H_4COO)_8(DMF)_4]$ (**1-*p***) were prepared readily and then screened for further surface modifiability in reactions with a model strained alkyne, *exo*-bicyclo[6.1.0]non-4-yn-9-ylmethanol (BCN), whose -alkyne

participates in CS-SPAAC and the OH group acts as a handle to deliver additional functionality illustrated by *exo*-bicyclo[6.1.0]non-4-yn-9-ylmethylferrocenecarboxylate (FcBCN). FcBCN was chosen to illustrate the general feasibility of post-assembly surface modification with a larger group that can bring additional functionality. The click product and parent clusters were analyzed by NMR, FT-IR, and UV-Vis. spectroscopy and XPS to confirm that the click reaction proceeds, and the parent clusters were analyzed by SCXRD to illustrate details of the core and surface aryl-azides.

2.2   Results and Discussion

To synthesize **1-*p*** and **1-*m***, *p*-azidobenzoic acid and *m*-azidobenzoic acid were prepared from the corresponding aminobenzoic acid, through the standard diazotization reaction, in nearly quantitative yields.[26,27] These azidobenzoic acid ligands were added to a DMF/MeCN solution of $AgNO_3$ and $[Ag(S^tBu)]_n$ (synthesized according to literature, see Appendix A) in a molar ratio of 8:10:10 to yield the nanoclusters, in a one pot synthesis, based on the process outlined by Gao and Zang *et al*.[25]. The yields were 80% for the *p*-azidobenzoate decorated cluster **1-*p*** and 78% in the case of the *m*-azidobenzoate decorated **1-*m***. These clusters can be easily made in 100 mg quantities at a time.

Crystals for SCXRD analysis were grown by slow evaporation in darkness over 1-2 days, resulting in colourless block crystals for both **1-*p*** and **1-*m***. Both clusters crystallize in the triclinic space group *P*-1, and have cluster cores similar to those described previously (**Figure 2.1** and **Figure 2.2** for **1-*p***, **Figure 2.3** and **Figure 2.4** for **1-*m***).[24,25] The Ag-Ag and Ag-S bond lengths within the core of each cluster fall within the ranges of Ag-Ag and Ag-S bonds reported previously,[25] though bond lengths were longer when the surface is decorated with *p*-azidobenzoate (Ag-Ag = 2.9120(7)-3.343(12) Å, avg. = 3.139 Å; Ag-S = 2.4225(9)-2.657(7) Å, avg. = 2.505 Å) than with *m*-azidobenzoate (Ag-Ag = 2.9429(4)-3.3655(4) Å, avg. = 3.119 Å; Ag-S = 2.4188(7)-2.5980(6) Å, avg. = 2.502 Å). Compared to the model benzoate decorated Ag_{20} cluster[25] (Ag-Ag = 2.962(8)-3.218(5) Å, Ag-S = 2.437(3)-2.581(7) Å), **1-*p*** and **1-*m*** have shorter Ag-Ag and Ag-S bond lengths but over a broader range, likely due to the electronic effect of the azide substituent. There are 4

molecules of DMF ligated to the Ag_{20} core in each case, as well as a carbonate template within the Ag_{20} core which results from the fixation of atmospheric CO_2 as previsouly described by Sun and coworkers.[24] This gives rise to 3 different types of Ag-O bonds (**Figure 2.5**) resulting from the carbonate template (Ag-O$_{template}$), carboxylate ligand (Ag-O$_{ligand}$), and coordinated DMF (Ag-O$_{solvent}$). Transmission electron microscopy (TEM) images of **1-*p*** and **1-*m*** showed diameter of about 2-3 nm consistent with the results of single crystal X-ray diffraction, although some larger agglomerates were observed due to the nature of the sample preparation (**Figure 2.12**, **Figure 2.13**, and **Figure 4.25A - Figure 4.33A**).
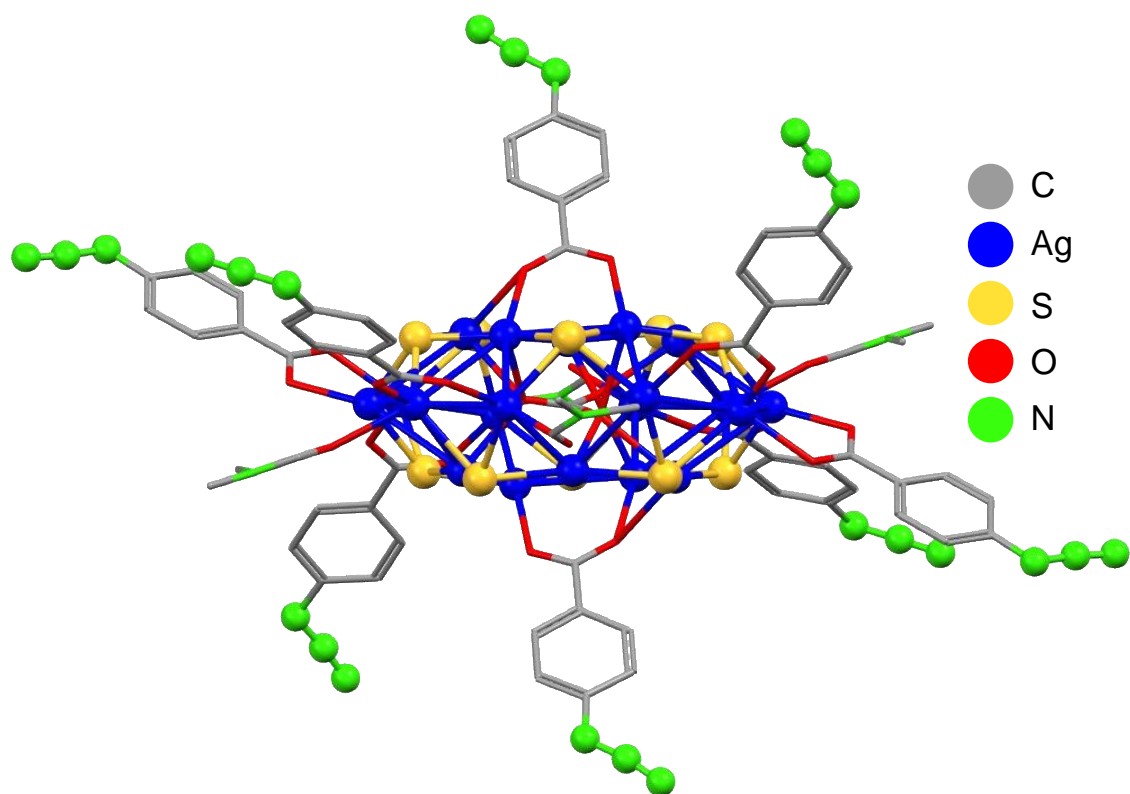
Figure 2.1: Molecular structure of $[CO_3@Ag_{20}(S^tBu)_{10}(p\text{-}N_3\text{-}C_6H_4COO)_8(DMF)_4]$, **1-*p***, viewed from the side. For clarity and to emphasize the azide decorated surface, hydrogen atoms and tert-butyl groups have been omitted.
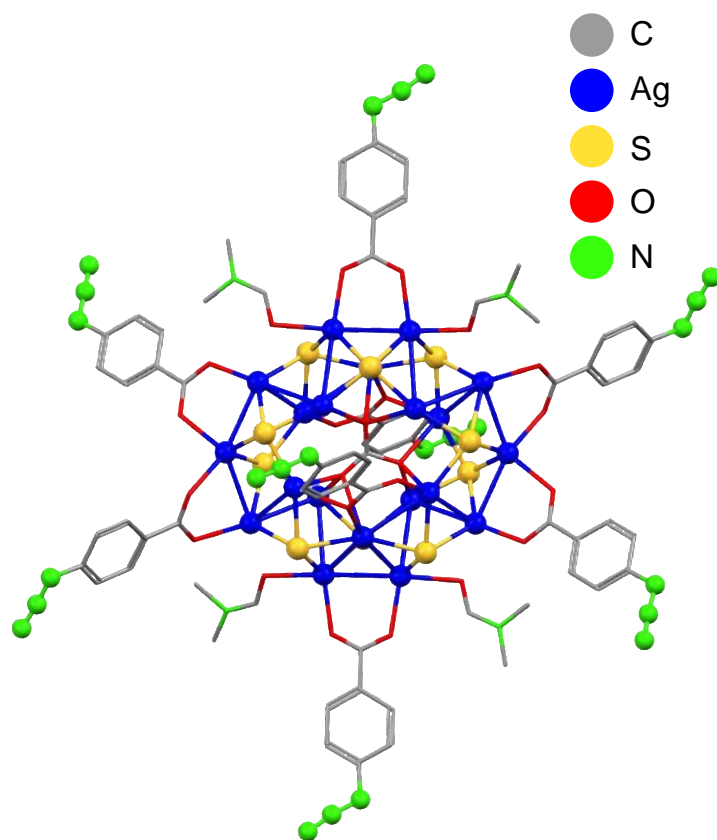
Figure 2.2: Molecular structure of [CO_3@Ag_{20}(S^tBu)$_{10}$(p-N_3-C_6H_4COO)$_8$(DMF)$_4$], **1-p**, viewed from above. For clarity and to emphasize the azide decorated surface, hydrogen atoms and tert-butyl groups have been omitted.
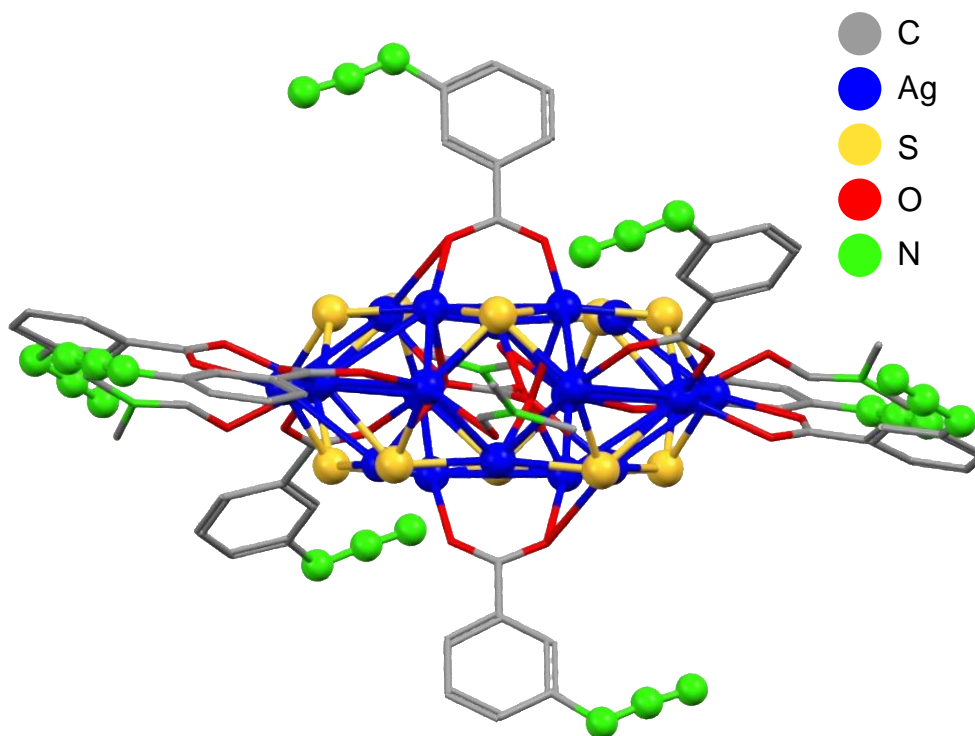
Figure 2.3: Molecular structure of $[CO_3@Ag_{20}(S^tBu)_{10}(m\text{-}N_3\text{-}C_6H_4COO)_8(DMF)_4]$, **1-*m***, viewed from the side. For clarity and to emphasize the azide decorated surface, hydrogen atoms and tert-butyl groups have been omitted.
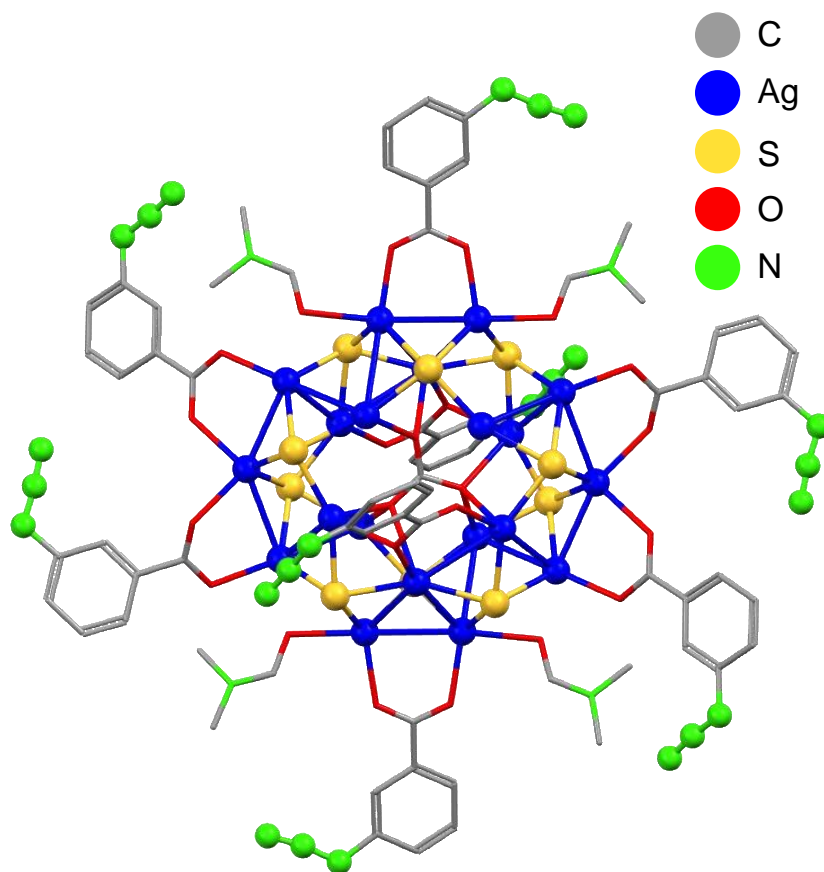
Figure 2.4: Molecular structure of [CO$_3$@Ag$_{20}$(S^{t}Bu)$_{10}$(m-N$_3$-C$_6$H$_4$COO)$_8$(DMF)$_4$], **1-m**, viewed from above. For clarity and to emphasize the azide decorated surface, hydrogen atoms and tert-butyl groups have been omitted.
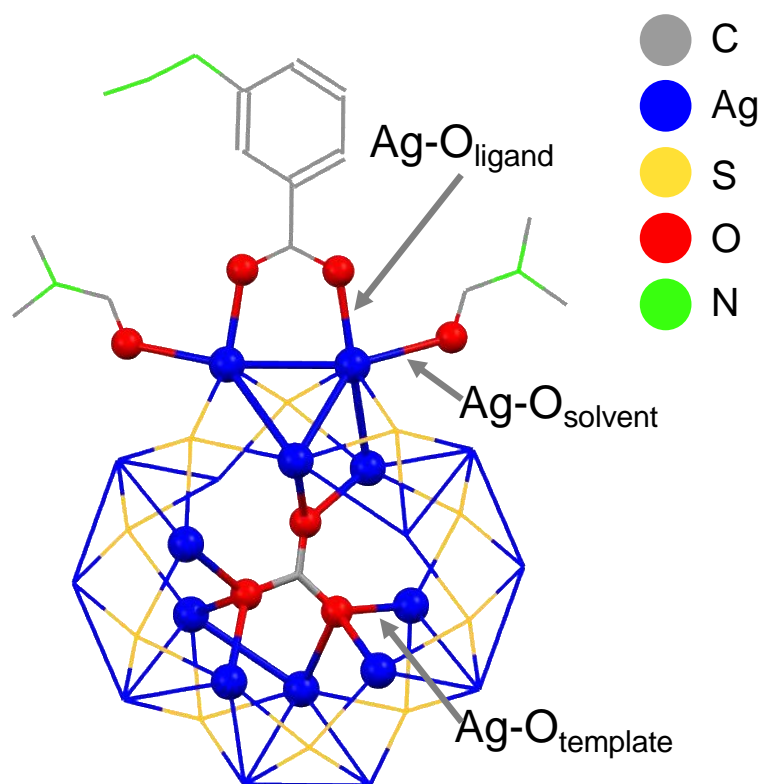
Figure 2.5: Illustration of Ag-O bond types present in $[CO_3@Ag_{20}(S^tBu)_{10}(p\text{-}N_3\text{-}C_6H_4COO)_8(DMF)_4]$ (**1-*p***), and $[CO_3@Ag_{20}(S^tBu)_{10}(m\text{-}N_3\text{-}C_6H_4COO)_8(DMF)_4]$ (**1-*m***). For clarity, only one benzoate and two solvent moieties are show, while tert-butyl groups and hydrogen atoms are omitted.

The FT-IR spectrum of each azide functionalized cluster displays similar features, and so for this discussion only **1-*p*** is discussed (see **Figure 2.7** for **1-*m***). The diagnostic asymmetric azide peak at around 2100 cm^{-1} (**Figure 2.6★**) and the presence of the carbonate anion in the cluster is indicated by the band at 1455 cm^{-1} (**Figure 2.6■**).
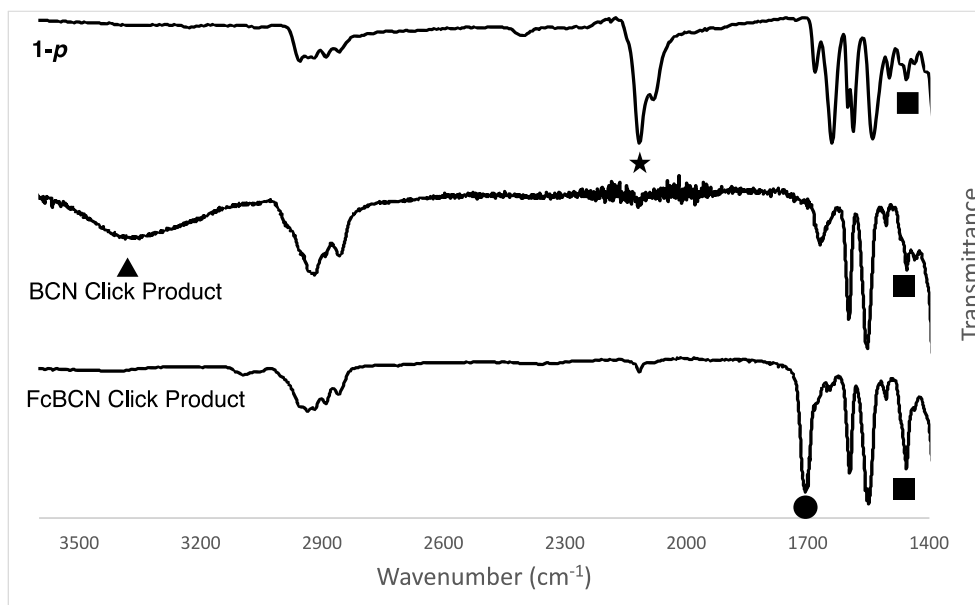
Figure 2.6: Staggered FTIR spectra of **1-*p*** and its reaction products with BCN and FcBCN. A successful click reaction is indicated by the loss of the azide stretch (★) and the appearance of new stretches associated with the clicked moiety, such as the OH stretch (▲) for BCN or ester stretch for FcBCN (●). The carbonate template (■) is retained after click reactions.
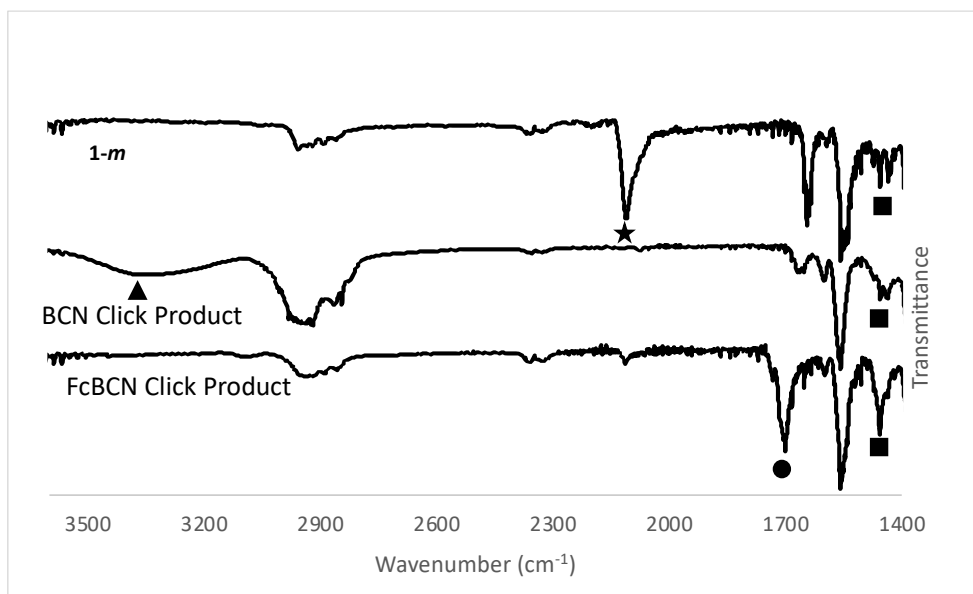
Figure 2.7: Staggered FTIR spectra of **1-*m*** and its reaction products with BCN and FcBCN. A successful click reaction is indicated by the loss of the azide stretch (★) and the appearance of new stretches associated with the clicked moiety, such as the OH stretch (▲) for BCN or ester stretch for FcBCN (●). The carbonate template (■) is retained after click reactions.

Both clusters were analyzed by ^{1}H and ^{13}C{^{1}H} NMR spectroscopy in CDCl$_3$ solutions (**Figures 4.1A - Figure 4.13A**). In the ^{1}H NMR spectra (**Figure 2.8** and **Figure 2.9**), the *t*-butyl resonance is seen as a single resonance at 1.66 ppm in the case of **1-*p*** but as several resonances at 1.59, 1.62 and 1.66 ppm in the case of **1-*m***. This behaviour had been seen before in such carboxylate decorated nanoclusters.[25] In **1-*p*** and **1-*m***, the aromatic proton peaks of the benzoates are shifted compared to the corresponding free acid. For example, the aromatic peaks for the **1-*p*** appear as 2 sets of doublets at 8.16 ppm and 7.06 ppm, compared to doublets at 8.11 ppm and 7.11 ppm in free *p*-N$_3$C$_6$H$_4$COOH. The coupling pattern for aromatic protons is more complex in **1-*m*** and *m*-azidobenzoic acid. In **1-*m*** the aromatic protons appear as a doublet at 7.93 ppm, a singlet at 7.86 ppm, a triplet at 7.39 ppm and a doublet at 7.11 ppm. For detailed assignments see Figure S4. The integration

supports the expected integration of 32 (16 + 16 for **1-p**, 8 + 8 + 8 + 8 for **1-m**) aromatic hydrogens, 28 (4 + 12 + 12) DMF ligands, and 90 *t*-butyl hydrogen atoms.
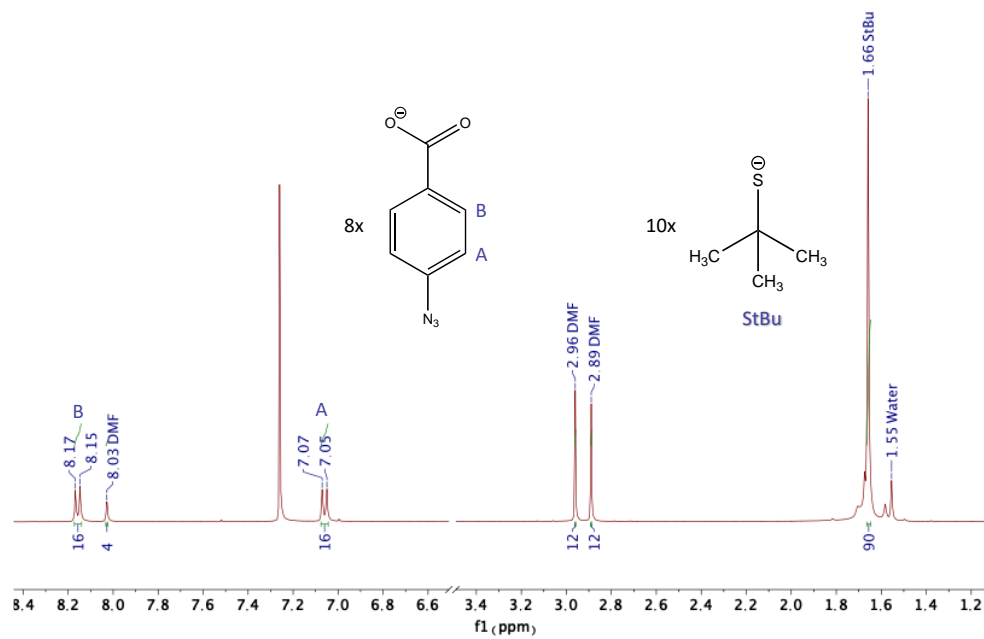
Figure 2.8: ^{1}H NMR spectrum of [(CO$_3$)@Ag$_{20}$(S^{t}Bu)$_{10}$(*p*-N$_3$-C$_6$H$_4$COO)$_8$(DMF)$_4$] (**1-p**) in CDCl$_3$.
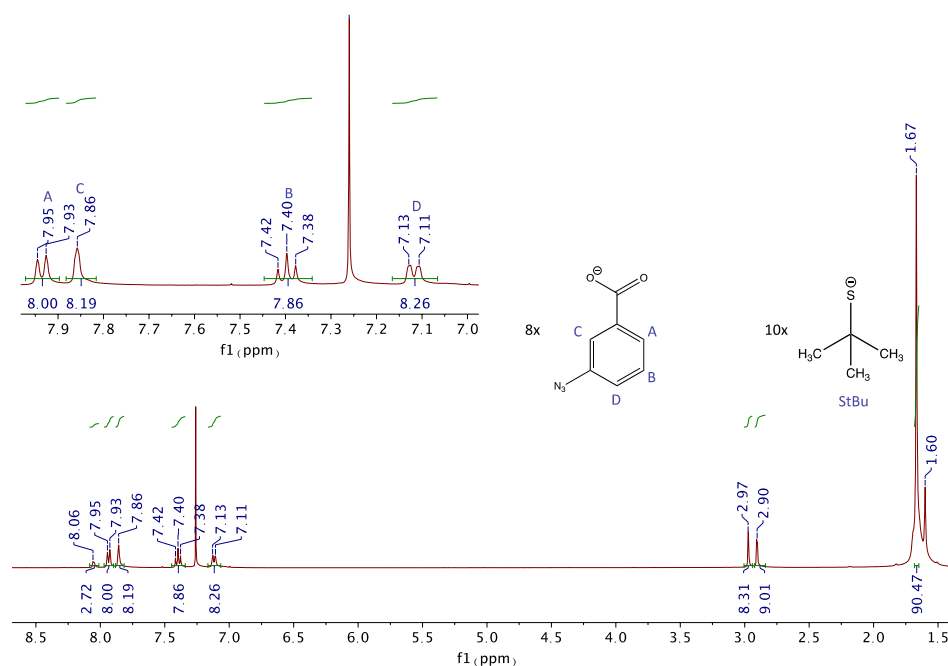
Figure 2.9: ^{1}H NMR spectrum of [(CO$_3$)@Ag$_{20}$(S^{t}Bu)$_{10}$(*m*-N$_3$-C$_6$H$_4$COO)$_8$(DMF)$_4$] (**1-*m***) in CDCl$_3$.

The UV-Vis. absorption spectra (**Figure 4.15A**) of **1-*p*** (0.0043 mM in CH$_2$Cl$_2$, ε = 218 000) show a 11.5-fold increase in maximum absorbance over the free *p*-azidobenzoic acid (0.0048 mM in DMSO, 19 000 L mol^{-1} cm^{-1}), which correlates to the presence of 8 *p*-azidobenzoate moieties on the cluster. Cluster **1-*p*** is weakly emitting at room temperature as previously reported,[24] and shows a reduced emission intensity at 300 - 310 nm compared to *p*-azidobenzoic acid, likely due to quenching by the silver thiolate core.

To probe the reactivity of the azide functionalized clusters towards strained alkynes, BCN was used as a model reagent (**Scheme 2.1**). To do this, clear, colourless solutions of either the **1-*p*** or **1-*m*** were a CH$_2$Cl$_2$ solution containing an excess of BCN was added dropwise. Within 5 minutes, the solution became opaque as the colourless reaction product precipitated. The reaction of **1-*p*** will be discussed here but characterization of the **1-*m*** reaction product can be found in the Appendix A. The FT-IR spectrum of the solution and precipitate indicates the loss of the azide peak, demonstrating the reactivity of all surface

azide moieties and the appearance of new peaks from the BCN, including the OH at 3350 cm^{-1} (**Figure 2.6▲**).
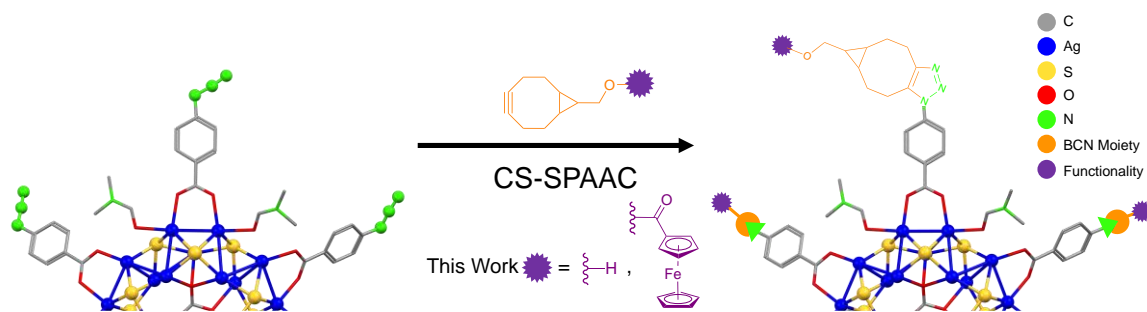
Scheme 2.1: Reaction of azide decorated cluster (1-*p*) with a functionalized BCN molecule, resulting in a triazole linkage which binds the functionalized BCN to the cluster surface.

Direct comparison between the ^{1}H NMR spectrum of **1-*p*** and its BCN click product is complicated by the latter's lack of solubility in the same solvent. The aromatic peaks of the click product are 8.21 ppm and 7.51 ppm. For comparison, the free *p*-azidobenzoic acid displays doublets at 7.96 and 7.22 ppm when measured in DMSO-d_6. Furthermore, the click product no longer shows aromatic doublets but broad singlets. The same broadening effect can be seen with peaks characteristic of BCN, such as the doublet of doublets, triplet of triplets, and doublet of triplets at 2.45, 2.32, and 2.19 ppm which have shifted and lost any discernable multiplicity from the broadening effect. This broadening is due to modification of the cluster surface and shows both the aromatic and BCN protons being incorporated into the click product.

Both clusters were reacted with an excess of FcBCN to install ferrocene moieties on the surface of the cluster via the CS-SPAAC. As can be seen in **Figure 2.6★**, the azide stretch in **1-*p*** before CS-SPAAC is no longer present, indicating that the azide moieties reacted quantitatively. Additionally, the ester linkage in FcBCN appears at 1706 cm^{-1} (**Figure**

2.6 ●). Reaction products were analyzed by ^{1}H NMR spectroscopy to confirm the presence of ferrocene on the cluster surface (**Figure 2.10** + **Figure 4.7A**). The spectra show incorporation of FcBCN due to the broadening of the peaks when compared to the free FcBCN, as seen before in the BCN click product. Crystals of the product could not be grown under various conditions attempted. UV-Vis. spectroscopy was used to further confirm the structure of the product. At low concentration, the absorbance band at 274 nm is no longer present, which possibly corresponds to the transformation of the azide moiety into a triazole linkage. At high concentration an absorbance band corresponding to ferrocene can be observed (**Figure 4.17A**).
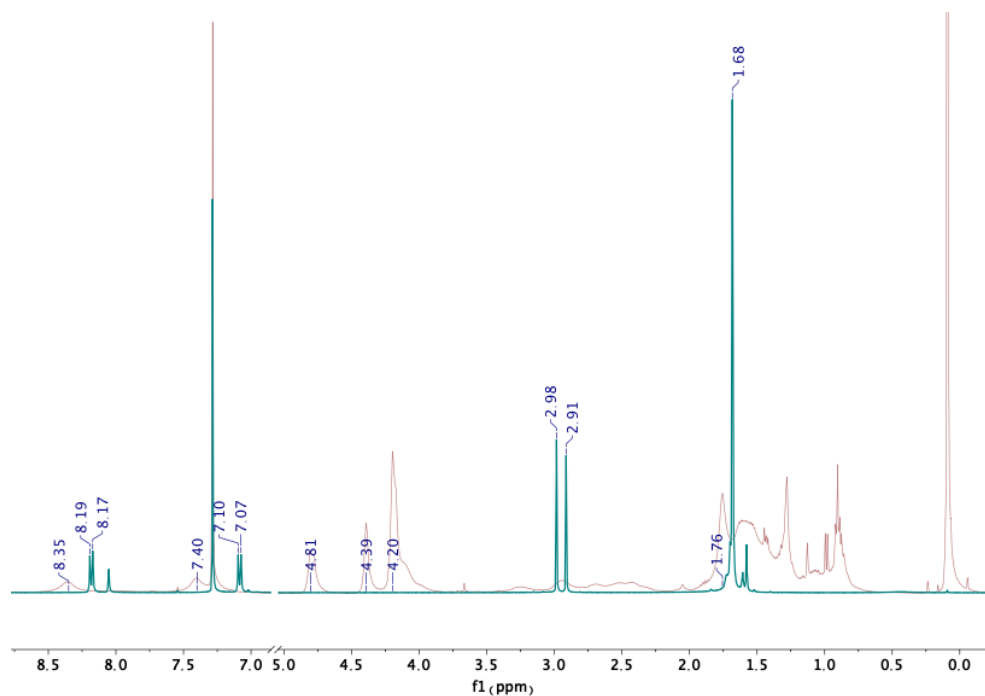
Figure 2.10: Superimposed ^{1}H NMR spectra for **1-p** (green trace) and **1-p** + FcBCN reaction product (red trace), both collected in CDCl$_3$.

The click products of **1-p** and **1-m** with FcBCN were analyzed by cyclic voltammetry and differential voltammetry. The differential and cyclic voltammograms are shown in **Figure 2.11** and clearly show the redox of the incorporated ferrocene moieties with the oxidation peak occurring at 0.30 V and the reduction peak occurring at –0.20 V for **1-p** vs. the

ferrocene/ferrocenium couple, respectively. For **1-*m***, oxidation peak occurs at 0.10 V and the reduction peak occurs at -0.01 V vs. the ferrocene/ferrocenium couple. These half wave potentials ($E_{1/2}$ = +0.05 V for **1-*p***, +0.05 for **1-*m***) are shifted to slightly more positive potentials relative to free ferrocene, which was used as a reference. The broader redox waves may be due to slightly different redox potentials of the ferrocenyl groups on the cluster, or due to some fouling of the electrode as a film was observed at the conclusion of the experiment. Compared to free ferrocenyl esters[28a] as well as ferrocenyl esters ligated to other silver nanocluster frameworks,[25,28b,28c] these values are lower.
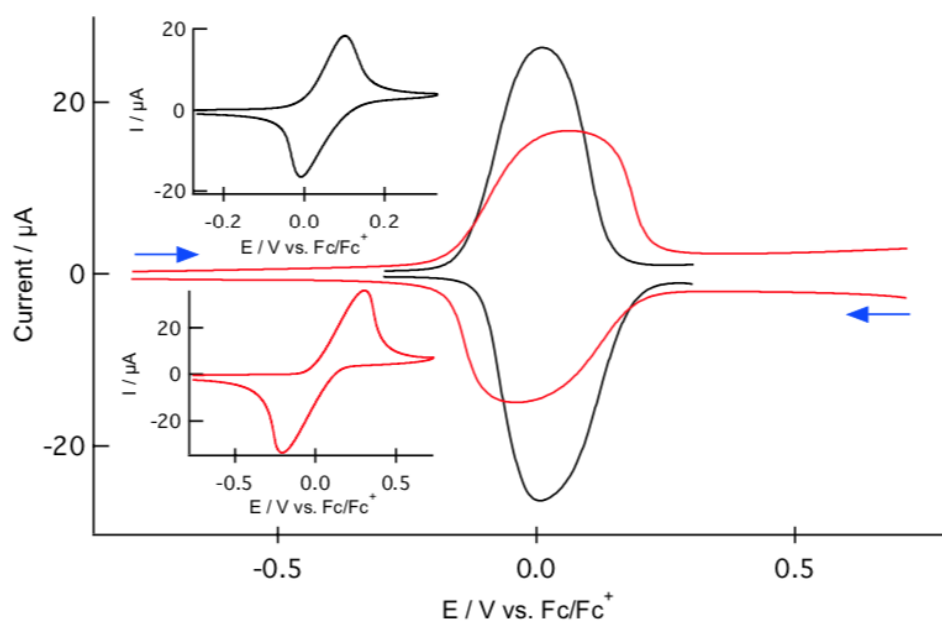
Figure 2.11: Differential pulse voltammograms (DPVs) of 1 mM **1-*p*** (red curves) and **1-*m*** (black curves) collected in dichloromethane containing 0.1 M tetra-*n*-butylammonium hexafluorophosphate (TBAPF$_6$). A 3-mm glassy carbon (GC) electrode served as working electrode. DPVs collected at peak amplitude of 50 mV, a pulse width of 0.05 s, 4 mV increment per cycle, and a pulse period of 0.2 s were applied to obtain DPVs. The arrows indicate potential scan directions. The insets display cyclic voltammograms (CVs) of the same solutions recorded at 50 mV/s scan rate.

Transmission electron microscopy (TEM) imaging was used to confirm that the cluster core remains intact after clicking with BCN or FcBCN. As illustrated by **Figure 2.12** and **Figure 2.13**, core diameters remain unchanged after the click reaction for **1-*p*** (see **Figure 4.21A - Figure 4.24A** for **1-*m*** reaction products and reaction product between **1-*p*** and BCN). X-ray photoelectron spectroscopy (XPS) analyses were performed confirm CS-SPAAC reactivity. For **1-*p***, the N1s region was recorded at different exposure times given the well-known degradation of azido groups under X-ray radiation.[29] At the initial time (t = 10 min.) it is possible to fit three components at 399.35 eV, 400.94 eV and 405.86 eV, with the latter two corresponding to the lateral N^- atoms and the central N^+ atom in the azido group, respectively (**Figure 2.14**), consistent with a previous report by Chehimi and coworkers.[29] The N^-/N^+ peak ratio is 1.6, which is slightly lower than the expected value of 2 for the number of N in the azido group due to loss of N_2 from photodegradation.[30] For the reaction of (**1-*p***) and FcBCN the N1s region supports the CS-SPAAC transformation of azide into triazole (**Figure 2.15**). In addition to the disappearance of the signal for N^+, three components were fitted at the N1s region that can be assigned to the triazole moiety based off previous work by Unger, Schalley, and coworkers.[30] The component at 399.52 eV is due to N=C, the component at 400.06 eV is assigned to N=N in the triazole ring. The component at 401.48 eV could be assigned to NH^+ groups and N^+ in the triazole ring.[31] The peak in the $Fe2p_{3/2}$ region of the click product at 707.93 eV supports the incorporation of ferrocene moiety into the product.[32] For additional XPS data for the Ag3d, C1s, O1s, and S2p regions of (**1-*p***) and its click product with FcBCN, see **Figure 4.25A - Figure 4.33A**.
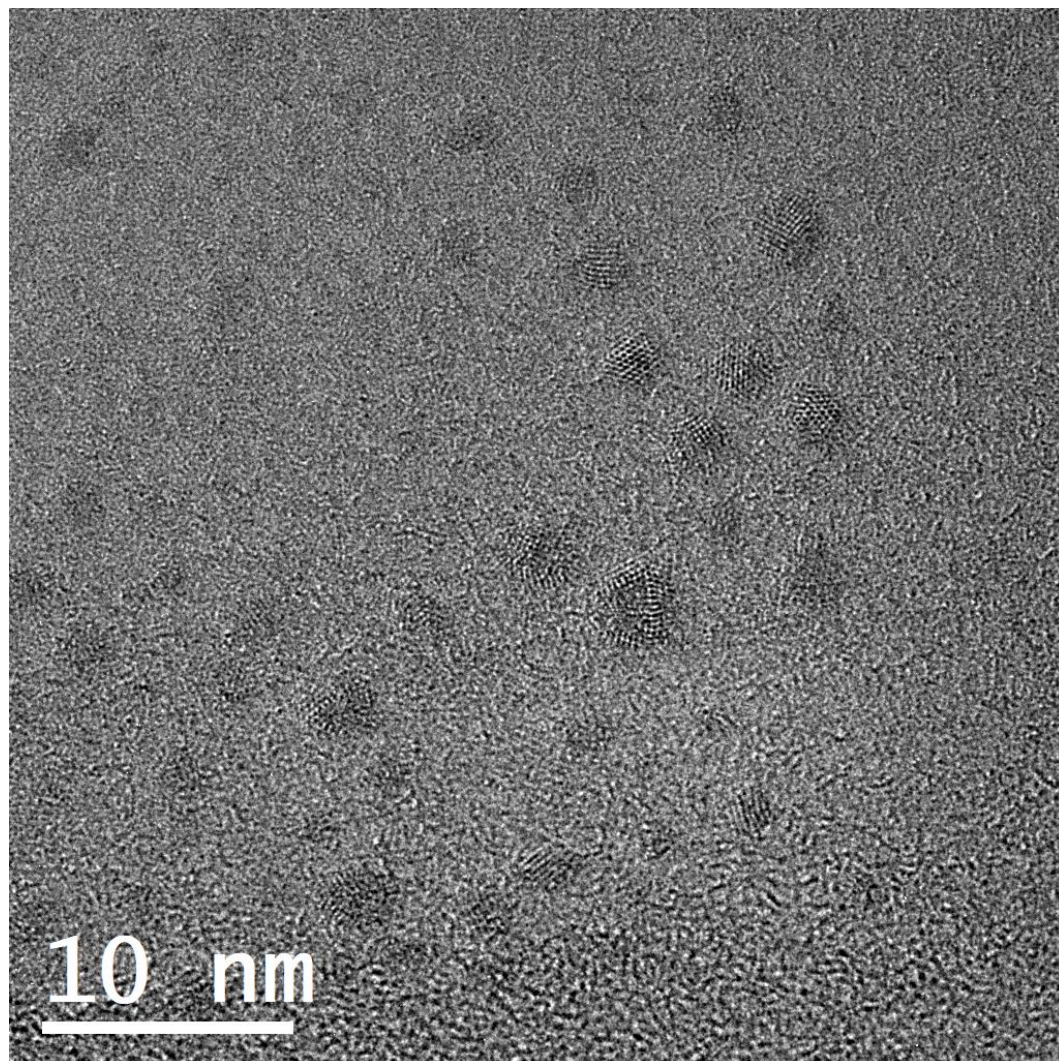
Figure 2.12: Transmission electron microscopy (TEM) image of **1-*p***. The sample shows cluster species on the size regime of 2 – 3 nm (expected; 1.07 nm for $CO_3@Ag_{20}S_{10}$ core, 2.35 nm for benzoate – benzoate distance).
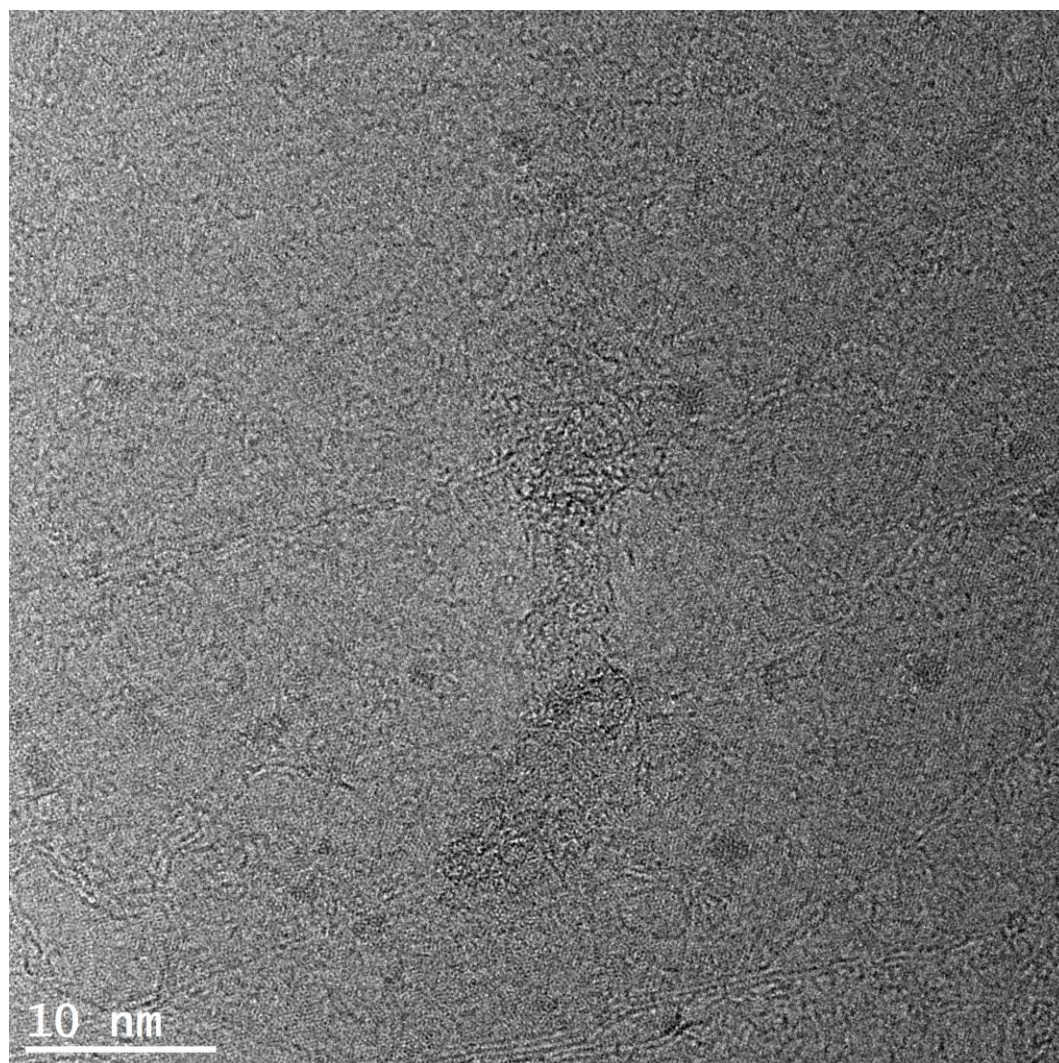
Figure 2.13: Transmission electron microscopy (TEM) image of the reaction product from the reaction of **1-*p*** + FcBCN. The sample shows cluster species on the size regime of 2 – 3 nm (expected; 1.07 nm for $CO_3@Ag_{20}S_{10}$ core, 2.35 nm for benzoate – benzoate distance).
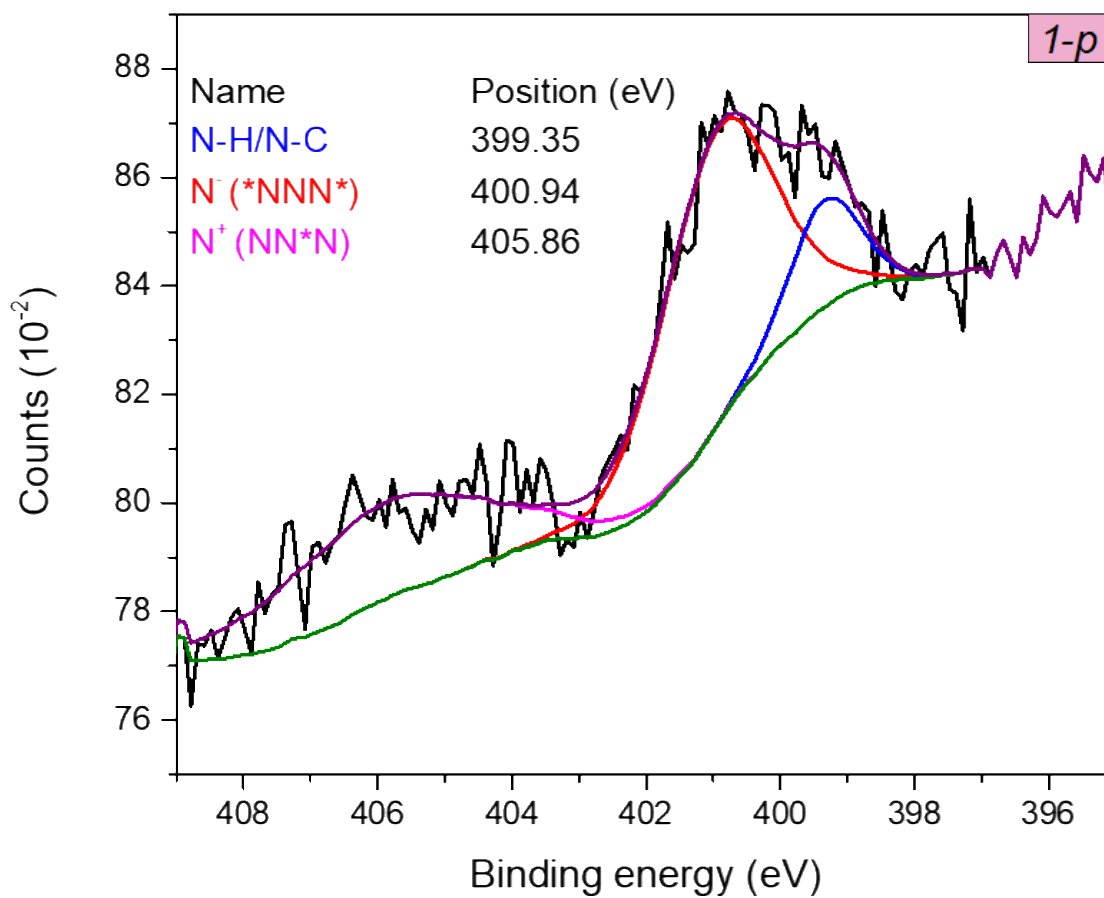
Figure 2.14: XPS spectrum of the N1s region for **1-*p***, showing peaks corresponding to different nitrogen bonding modes, such as N-$\underline{N}^+$-N⁻ at 405.86 eV, N-N⁺-$\underline{N}$⁻ at 400.94 eV, and N-C at 399.35 eV.
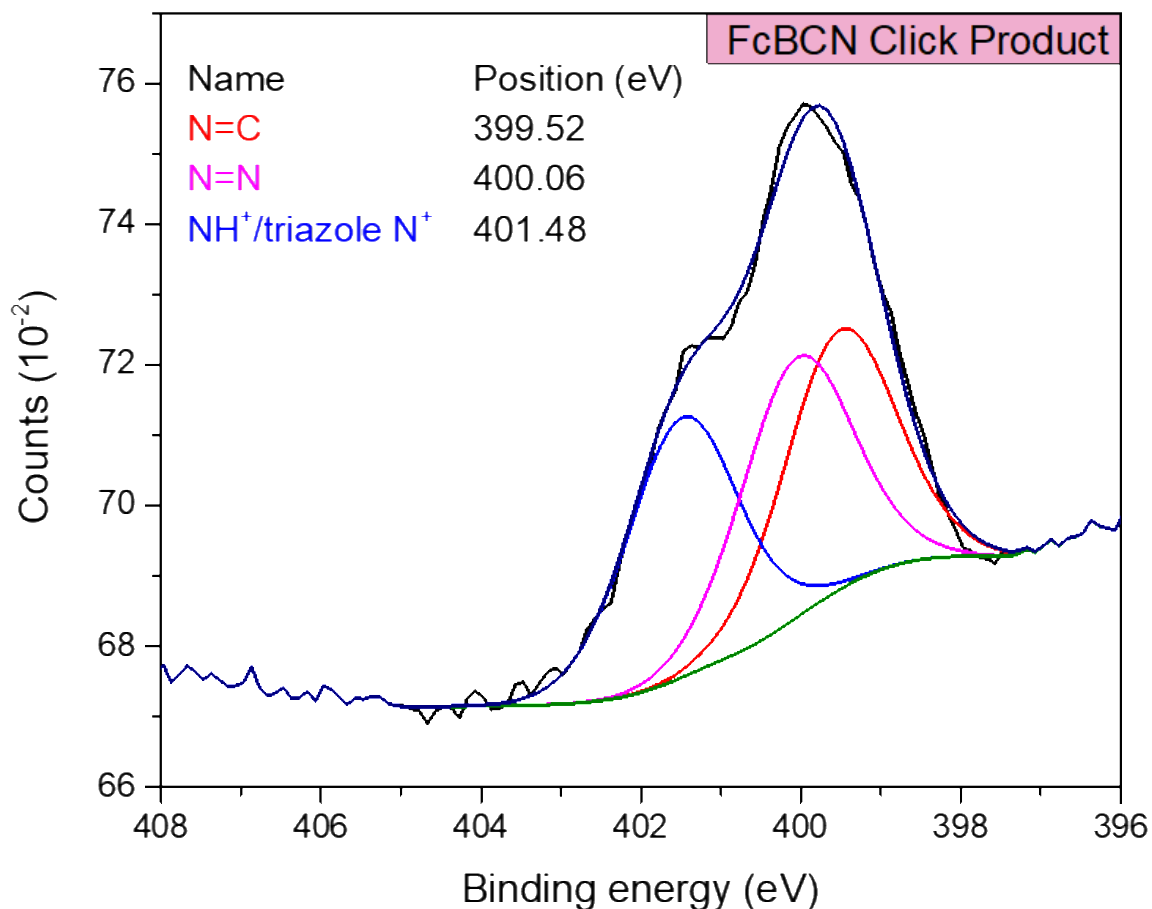
Figure 2.15: XPS spectrum of the N1s region for the product of **1-*p*** + FcBCN, showing peaks corresponding to different nitrogen bonding modes, such as N^+ (triazole) at 401.48 eV, N=N at 400.06 eV, and N=C at 399.52 eV.

Two remarkably stable novel Ag_{20} clusters were synthesized that are decorated with 8 (*p*-/*m*-)azidobenzoate ligands. These are the first examples of silver nanoclusters which possess an azide surface moiety. It was further demonstrated that these clusters undergo the rapid CS-SPAAC reaction under mild conditions, as shown via reactions with the model BCN strained alkyne. Given the alcohol handle the BCN possesses, these nanoclusters with a BCN surface could be functionalized a variety of different ways by

installing a functional group though esterification. A functionalized BCN, FcBCN, was also successfully installed on the cluster surface, further demonstrating how easily the cluster surface can be functionalized. This ease of functionalization allows for the surface of the nanocluster to be finely tailored, which in turn enhances its applicability in various fields.

2.3 References

1. Park, H. J.; Shin, D. J.; Yu, J. *J. Chem. Educ.* **2021**, *98* (3), 703−709

2. Steigerwald, M. L.; Brus, L. E. *Annu. Rev. Mater. Sci.* **1989**, *19* (1), 471−495

3. Chakraborty, I; Pradeep, T. *Chem. Rev.* **2017**, *117* (12), 8208−8271

4. Corrigan, J. F.; Fuhr, O.; Fenske, D. *Adv. Mater.* **2009**, *21* (18), 1867–1871

5. Brus, L. *J. Phys. Chem.* **1986**, *90* (12), 2555-2560

6. (a) Liu, B.; Wang, D.; Zhang, Y.; Fan, H.; Lin, Y.; Jianga, T.; Xie, T. *Dalton Trans.* **2013**, *42* (6), 2232–2237.; (b) Khanchandani, S.; Srivastava, P. K.; Kumar, S.; Ghosh, S.; Ganguli, A. K. *Inorg. Chem.* **2014**, *53* (17), 8902−8912

7. Zhang, Y.; Liu, B.; Wang, D.; Lin, Y.; Xie, T.; Zhai, J. *Mater. Chem. Phys.* **2012**, *133* (2-3), 834– 838

8. (a) Jia, X.; Li, D.; Li, J.; Wang, E. *RSC Adv.* **2015**, *5* (99), 80929-80932; (b) Gao, Z.; Liu, F.; Hu, R.; Zhaob, M.; Shao, N. *RSC Adv.* **2016**, *6* (70), 66233–66241; (c) Wang, X.; Wang, N.; Li, L.; Xiao, R.; Yuan, L.; Yang, X.; Li, N. *RSC Adv.* **2017**, *7* (52), 32536–32542

9. (a) Dong, X.-Y.; Huang, H.-L.; Wang, J.-Y.; Li, H.-Y.; Zang, S.-Q. *Chem. Mater.* **2018**, *30* (6), 2160−2167; (b) Du, X.-S.; Yan, B.-J.; Wang, J.-Y.; Xi, X.-J.; Wang, Z.-Y.; Zang, S.-Q. *Chem. Commun.* **2018**, *54* (42), 5361-5364

10. Kang, X.; Ren, M.; Zhu, M.; Zhang, K. *Chem. Mater.* **2020**, *32* (15), 6736–6743

11. (a) Kang, X.; Zhu, M. *Chem. Mater.* **2019**, *31* (24), 9939−9969; (b) Bootharaju, M. S.; Burlakov, V. M.; Besong, T. M. D.; Joshi, C. P.; AbdulHalim, L. G.; Black, D. M.; Whetten, R. L.; Goriely, A.; Bakr, O. M. *Chem. Mater.* **2015**, *27* (12), 4289−4297

12. Li, Y.-L.; Zhang, W.-M.; Wang, J.; Tian, Y.; Wang, Z.-Y.; Du, C.-X.; Zang, S.-Q.; Mak, T. C. W. *Dalton Trans.* **2018**, *47* (42), 14884–14888

13. (a) Bootharaju, M. S.; Kozlov, S. M.; Cao, Z.; Harb, M.; Parida, M. R.; Hedhili, M. N.; Mohammed, O. F.; Bakr, O. M.; Cavallo, L.; Basset, J.-M. *Nanoscale* **2017**, *9* (27), 9529–9536; (b) Bootharaju, M. S.; Joshi, C. P.; Parida, M. R.; Mohammed, O. F.; Bakr, O. M. *Angew. Chem. Int. Ed.* **2016**, *55* (3), 922–926; *Angew. Chem.* **2016**, *128* (3), 934–938

14. Gunawardene, P. N.; Corrigan, J. F.; Workentin, M. S. *J. Am. Chem. Soc.* **2019**, *141* (30), 11781−11785

15. Gunawardene, P. N.; Martin, J.; Wong, J. M.; Ding, Z.; Corrigan, J. F.; Workentin, M. S. *Angew. Chem. Int. Ed.* **2022**, *61*, e202205194; *Angew. Chem.* **2022**, *134*, e202205194

16. (a) Agard, N. J.; Prescher, J. A.; Bertozzi, C. R. *J. Am. Chem. Soc.* **2004**, *126* (46), 15046-15047; (b) Rostovtsev, V. V.; Green, L. G.; Fokin, V. V.; Sharpless, K. B. *Angew. Chem. Int. Ed.* **2002**, *41* (14), 2596-2599; (c) Zhang, L.; Chen, X.; Xue, P.; Sun, H. H. Y.; Williams, I. D.; Sharpless, K. B.; Fokin, V. V.; Jia. G. *J. Am. Chem. Soc.* **2005**, *127* (46), 15998-15999

17. (a) Staudinger, H.; Meyer, J. *Helv. Chim. Acta* **1919**, *2* (1), 635−646; (b) Taylor, S. D.; Lohani, C. R. *Org. Lett.* **2016**, *18* (17), 4412−4415

18. Lin, F. L.; Hoyt, H. M.; van Halbeek, H.; Bergman, R. G.; Bertozzi, C. R. *J. Am. Chem. Soc.* **2005**, *127* (8), 2686-2695

19. Patterson, D. M.; Nazarova, L. A.; Prescher, J. A. *ACS Chem. Biol.* **2014**, *9* (3), 592−605

20. Kolb, H. C.; Finn, M. G.; Sharpless, K. B. *Angew. Chem. Int. Ed.* **2001**, *40* (11), 2004−2021

21. Kim, M.; Weerawardene, K. L. D. M.; Choi, W.; Han, S. M.; Paik, J.; Kim, Y.; Choi, M.-G.; Aikens, C. M.; Lee, D. *Chem. Mater.* **2020**, *32* (23), 10216–10226

22. (a) Jin, R.; Zeng, C.; Zhou, M.; Chen, Y. *Chem. Rev.* **2016**, *116* (18), 10346−10413; (b) Nasaruddin, R. R.; Chen, T.; Yan, N.; Xie, J. *Coord. Chem. Rev.* **2018**, *368*, 60–79; (c) Dainese, T.; Black, D. M.; Agrachev, M.; Antonello, S.; Fortunelli, A.; Badocco, D.; Gascón, J.; Venzo, A.; Whetten R. L.; Maran, F. *Chem. Sci.* **2018**, *9* (47), 8796–8805

23. Goh, J.-Q.; Malola, S.; Häkkinen, H.; Akola, J. *J. Phys. Chem. C* **2015**, *119* (3), 1583−1590

24. Yuan, S.; Deng, Y.-K.; Wang, X.-P.; Sun, D. *New J. Chem.* **2013**, *37* (10), 2973-2977

25. Li, S.; Du, X.-S.; Li, B.; Wang, J.-Y.; Li, G.-P.; Gao, G.-G.; Zang, S.-Q. *J. Am. Chem. Soc.* **2018**, *140* (2), 594−597

26. Yamashina, M.; Suzuki, H.; Kishida, N.; Yoshizawa, M. *Angew. Chem. Int. Ed.* **2021**, *60* (33), 17915-17919; *Angew. Chem.* **2021**, *133* (33), 18059-18063

27. Smith, P. A. S.; Hall, J. H.; Kan, R. O. *J. Am. Chem. Soc.* **1962**, *84* (3), 485-489

28. (a) Debroy, P.; Naskar, D.; Roy, S. *Inorg. Chim. Acta* **2006**, *359* (4), 1215-1221. (b) Liu, K.-G.; Rouhani, F.; Shan, Q.-D.; Wang, R.; Li, J.; Hu, M.-L.; Cheng, X.; Morsali, A. *Ultrason Sonochem* **2019**, *56*, 305-312. (c) Liu, Y.; Najafabadi, B. K.; Fard, M. A.; Corrigan, J. F. *Angew. Chem. Int. Ed.* **2015**, *54* (16), 4832-4835

29. Saad, A.; Abderrabba, M.; Chehimi, M. M. *Surf. Interface Anal.* **2017**, *49* (4), 340-344

30. Heinrich, H.; Traulsen, C. H.-H.; Darlatt, E.; Richter, S.; Poppenberg, J.; Traulsen, N. L.; Linder, I.; Lippitz, A.; Dietrich, P. M.; Dib, B.; Unger, W. E. S.; Schalley, C. A. *RSC Adv*. **2014**, *4* (34), 17694-17702

31. Saad, A.; Vard, C.; Abderrabba, M.; Chehimi, M. M. *Langmuir* **2017**, *33* (28), 7137-7146

32. Woodbridge, C. M.; Pugmire, D. L.; Johnson, R. C.; Boag, N. M.; Langell, M. A. *J. Phys. Chem. B* **2000**, *104* (14), 3085-3093

Chapter 3

3   Future Work and Conclusion

The previous chapter discussed how the first known example of an azide-decorated silver(I) thiolate nanocluster was synthesized, probed for click reactivity with BCN and FcBCN, and how both the parent clusters and click products were confirmed by various characterization methods. By contrast, this chapter seeks to lay out in detail how this azide-functionalized nanocluster framework can be expanded upon by focusing on different ways in which the surface reactivity can be taken advantage of, as well as on what structural changes can performed to generate a greater variety of surface reactive silver(I) thiolate nanoclusters.

3.1   Future Work

The first and most straightforward modification to perform would be to change the strained alkyne used to perform the CS-SPAAC reaction. A variety of strained alkyne platforms exist as previously mentioned, with handles that make for easy functionalization. Given this, it is easy to imagine that almost any functionalization could be installed on the $CO_3@Ag_{20}$ nanocluster's surface, with the proper strained alkyne platform and reaction conditions (**Figure 3.2**, (1)). As mentioned previously, the click products of **1-*p*** and **1-*m*** with BCN and FcBCN were unable to be crystallized with sufficient size and quality for characterization by single crystal x-ray diffraction (SCXRD). Choosing a more rigid strained alkyne, such as dibenzocyclooctyne (DIBO), may allow for future click products to be crystallized such that it can be structurally characterized by SCXRD to show that all azide functionalities are converted to triazole, instead of relying on IR and NMR spectroscopy to prove this. Looking towards the $CO_3@Ag_{20}$ cluster framework's applicability to biomedicine, and specifically bioimaging, it's disappointing that the azide decorated cluster, like benzoate decorated cluster,[1] has no fluorescence at room temperature. However, because the surface of the cluster can be easily modified, and because our group has already developed a derivative of Rhodamine B which incorporated

BCN[2] (**Figure 3.1**) which, as shown above, reacts with **1-*p*** and **1-*m***, making the installation of 8 moieties of the chromophore onto the cluster surface facile without needing to develop new methodologies. This should overcome two obstacles to using the using the cluster in bioimaging. First, it will make the cluster framework fluorescent, making it possible to detect the cluster *in vivo* with non-invasive exposure to light. Second, Rhodamine B is known to have excellent aqueous solubility which it could confer onto the nanocluster framework, the solubility of which can be heavily modified depending on the clicked substrate but is only soluble in chloroform or dichloromethane as **1-*p*** and **1-*m***. The benefits of using a cluster in bioimaging applications as opposed to the free chromophore is that it should octuple the emission intensity compared to the free chromophore, which allows a lower dosage to be used for imaging which in turn lowers any toxic effects so long as the toxicity of the cluster is not octuple that of the free chromophore. Additionally, binding multiple chromophores to a stable surface can aid in signal detection as it prevents the bound chromophores from diffusing from one-another until the signal from a single chromophore is too weak to discriminate from background noise. There have also several materials which have been alkyne functionalized to make them amenable to click chemistry, notably single-walled carbon nanotubes (SWCNT)[3] and nano-diamonds[4], which are of interest due to their electronic properties and stability. Click chemistry was applied to SWCNTs in order to graft polystyrene onto their surface and consequently overcome their limited solubility by making the clicked SWCNT soluble in solvents which dissolve polystyrene such as tetrahydrofuran.[3] In the case of nano-diamonds, click chemistry offers an easy route to surface functionalization which is difficult to achieve due to their stability.[4] In their study, Kreuger *et al.* were able to make nano-diamonds decorated with both surface aryl azides and aryl carboxylic acids, with which they were able to make a dually emissive material by attaching two different dyes to the SWCNT, one through a copper(I) catalyzed azide-alkyne cycloaddition and the other though amidation of the carboxylic acid with an amine functionalized dye.[4] The azide-decorated nanoclusters, **1-*p*** and **1-*m***, could be beneficial to the surface functionalization of carbonaceous materials. This is because of the alkyne moieties on SWCNTs and nanodiamonds are isolated from each other over the entire surface, which in turn means that **1-*p*** or **1-*m*** could be clicked to the surface of the

material and still have up to seven more azide moieties for further reaction, potentially septupling the number of appended functional moieties to the nanotube or nanodiamond, so long as alkyne functionalized dyes or polystyrene are available.
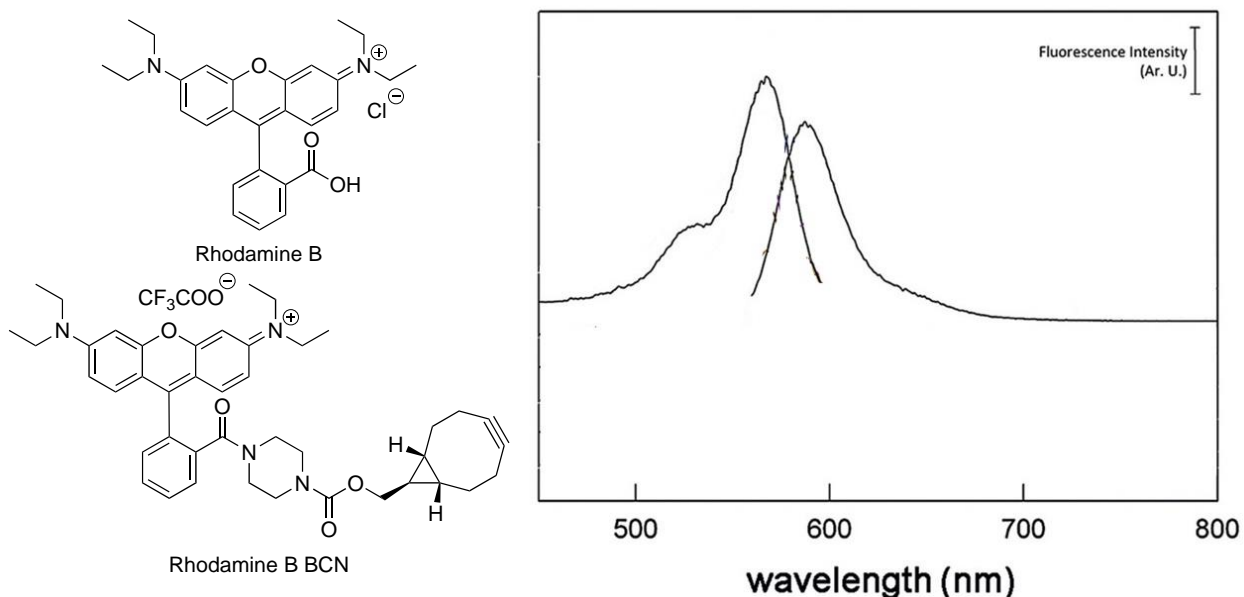
Figure 3.1: Structure of Rhodamine and Rhodamine B BCN, and the excitation (left trace) and emission (right trace) spectrum of Rhodamine BCN. Adapted with permission from Gobbo, P.; Gunawardene, P.; Luo, W.; Workentin, M. S. *Synlett* **2015**, *26* (9), 1169-1174. Copyright 2015 Wiley-VCH Verlag GmbH & Co. KGaA, Weinheim.

The second most straightforward modification to carry out would be changing the click reaction performed to modify the cluster surface. Above the cluster surface strain promoted azide-alkyne cycloaddition is discussed. In addition to this, a cluster with a reactive azide surface could also be modified using the Staudinger-Bertozzi ligation reaction (**Scheme 3.1**), which is an alteration on the canonical Staudinger reaction (**Scheme 3.2**) where a triarylphosphine with an ortho methyl ester is reacted together with an azide to afford the amide linkage from reaction of the nucleophilic nitrogen in the iminophosphorane bond with the mildly electrophilic carbonyl carbon of the methyl ester.[5] Developed in the early 2000's, the Staudinger-Bertozzi ligation is useful because it is fast, forms a very stable

amide adduct, and in regards to biolabeling it uses two moieties, azides and phosphines, which do not naturally occur in a biological system and which do not interfere with it, instead having specific reactivity with each other only.[5,6] The Staudinger-Bertozzi ligation can also be modified to transfer certain functional groups, such as acetyl groups, from the phosphine to the resulting amide when designed such that a breakable linkage like an ester or amine is incorporated between the transferable group and the rest of the triaryl phosphine.[6] So, the Staudinger-Bertozzi can both be used to extend the substrates tolerated by **1-*p*** and **1-*m*** to ortho methyl ester triaryl phosphines for functionalities that cannot be incorporated onto a stained alkyne, and also to fine-tune the surface to the nanoclusters through functional group transfers. In addition to the Staudinger-Bertozzi ligation, the canonical Staudinger reaction[7] can also be performed to obtain the amine-decorated cluster, which so far has remained elusive through the direct synthesis method using aminobenzoic acids in place of azidobenzoic acids. The amine decorated cluster can then also be used to attach functional molecules to the cluster surface through amidation. Another click reaction that can be performed is the copper-catalysed azide-alkyne cycloaddition (CuAAC),[8] which would expand the scope of reagents to terminal alkynes, though there is the possibility of introducing copper into the reaction mixture and possibly into the cluster itself. This would limit the cluster's applicability to biological systems,[8] but may result in a different, more interesting core geometry as alloy nanoclusters have been shown in the past to possess unique photoluminescent properties.[9]
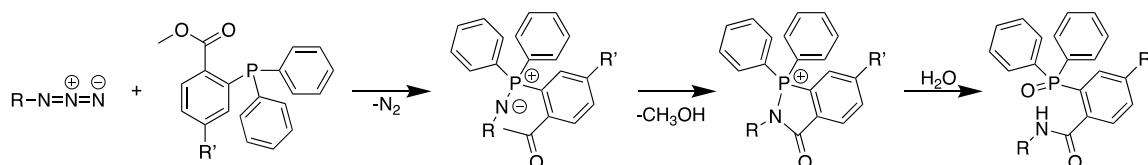
Scheme 3.1: Line diagram of the Staudinger-Bertozzi ligation reaction
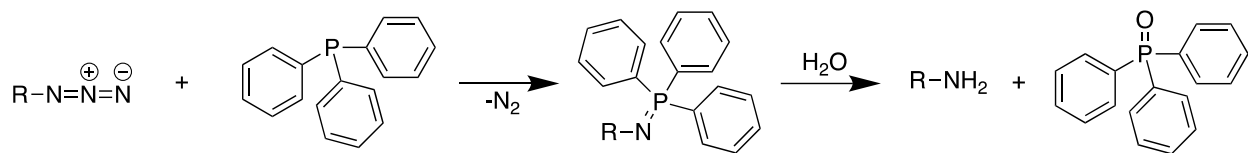
Scheme 3.2: Canonical Staudinger reaction, which produces an iminophosphorane which is quickly hydrolyzed to the corresponding amine and phosphine oxide in protic solvents.

 In addition to modifying the carboxylate ligand, there is also the possibility to modify the carboxylate and thiolate used. Given that the stabilizing thiolate used introduces a tert-butyl group close to the cluster surface, other sterically demanding thiols should be usable. If the thiol can be successfully changed, there is an opportunity to create a multifunctional cluster, with the thiol containing one functionality and the carboxylate ligand containing another. Another possibility, takes the concept of reactive azide surfaces to near its limits for the present framework, is to incorporate an azide onto the stabilizing thiol and to isolate the nitrated cluster, $[CO_3@Ag_{20}(SRN_3)_{10}(NO_3)_8]$. This cluster would be able to undergo a CS-SPAAC reaction on the azidothiolate ligands, and then a ligand displacement to introduce azidocarboxylate ligands, which could then undergo another click reaction. Using this approach, two different functionalities could be incorporated onto the same cluster. The benefit of this approach is that it allows for the cluster to be functionalized for a specific application during the first click reaction, while the second click reaction optimizes its physical properties for the system it will be used in. For example, the first click reaction could be used to install a fluorophore, while the second click reaction could surface moieties which allow for the cluster to be dissolved in a wider array of solvents, particularly in water, giving a water-soluble fluorescent marker. Another possibility is two install two functions that complement each other, leading to a composite material that is greater than its individual functionalities alone. An example would be to first click a drug on to the cluster surface followed by a fluorophore for the second click, so that the concentration of the drug carrying cluster in areas of the body can be monitored. If the drug is attached to the cluster via cleavable bond, such as one that photolyzes under UV light, then the release of the drug can be finely controlled and only take place when at the target

destination. With regards to materials, this approach maximizes points of attachment the cluster has, and so can be used to create highly cross-linked materials, or a cross-linker with additional functionality. With these different types of modifications, materials may become harder to characterize. With just the click reaction between BCN and **1-*p*** or **1-*m***, the ^{1}H NMR spectrum became very broad and messy. A particularly useful modification for ease of characterization regarding cluster click products would be to incorporate different NMR active nuclei on the cluster surface ligands with azide moieties and strained alkyne. For example, using a fluorinated surface ligand and protonated strained alkyne offers the distinct advantage in that the surface ligands of the click product can be monitored by ^{19}F NMR spectroscopy, while the strained alkyne is monitored by ^{1}H NMR spectroscopy. This simplifies both NMR spectra and allows for any problems occurring with the reaction to be associated with either the nanocluster surface (and showing in the ^{19}F spectrum), or the strained alkyne (and showing in the ^{1}H spectrum). A similar effect could also be achieved by incorporating silicon or selenium atoms as a probe close to the azide or strained alkyne moiety and monitoring the change in the respective spectrum to support the confirmation of click reactivity. Such a modification would be essential when clicking strained alkynes with complex ^{1}H NMR spectra, as the resultant broadening of the signals would make it difficult differentiate proton environments from each other if both the nanocluster surface ligand and strained functionalized alkyne were protonated.

Yet another structural modification, discovered serendipitously, is that the degree to which nitrates in the parent cluster $[CO_3@Ag_{20}(S^tBu)_{10}(NO_3)_8]$ are replaced by carboxylates in the resultant cluster $[CO_3@Ag_{20}(S^tBu)_{10}(RCOO)_{(x)}(NO_3)_{(8-x)}]$ can be controlled by the stoichiometry of the carboxylic acid added. As of yet, two 6-substituted clusters, $[CO_3@Ag_{20}(S^tBu)_{10}(p\text{-}N_3C_6H_4COO)_{(6)}(NO_3)_2(DMF)_4]$ (**2-*p***) and $[CO_3@Ag_{20}(S^tBu)_{10}(m\text{-}N_3C_6H_4COO)_{(6)}(NO_3)_2(DMF)_4]$ (**2-*m***), have been isolated and characterized. Importantly, the weakly coordinating nitrate ligands are always present at opposite sides of the cluster from each other and appear to sit on special positions at the top and bottom of the disc-shaped core (**Figure 3.3** and **Figure 3.4** for **2-*p***, **Figure 3.5** and **Figure 3.6** for **2-*m***). These 6-substituted clusters provide the opportunity to produce multifunctional clusters as there

are two distinct handles for modification. First, the six azidocarboxylates can be clicked to a functional strained alkyne. Second, the remaining nitrate ligands can be displaced by a different, functionalized carboxylate. Combined, these two handles allow for both diverse applications as well as a high degree of control over the structural properties of the cluster, allowing for fine tailoring towards specific applications. It also allows for supercluster architectures to be explored. Since the two positions left with easily displaced nitrate ligands are always opposite each other, multiple clusters could be linked together by using, for example, sebacic acid ($HOOC(CH_2)_8COOH$), to build a 1-dimentional chain of clusters. As the clusters can be functionalized before being linked, this presents a lot of interesting possibilities, such as having a chain with alternating sections which are decorated with different fluorophores, or having a chain that has alternating redox active moieties capable of 1 e$^-$ and 2 e$^-$ transfers so that a wide variety of reactions can be catalyzed.

Figure 3.2: Graphical summary of possible future directions for the developed azide decorated nanocluster system.
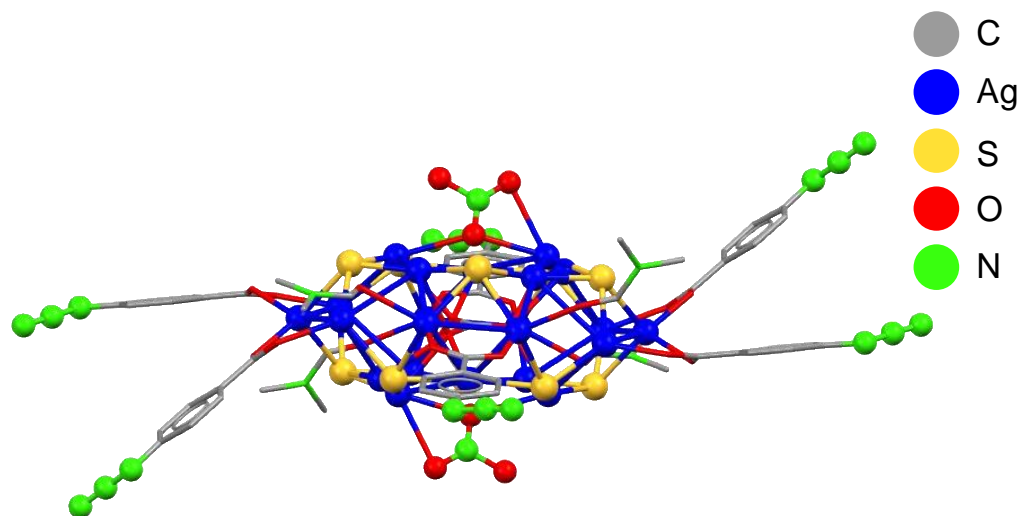
Figure 3.3: Molecular structure of [CO$_3$@Ag$_{20}$(S^{t}Bu)$_{10}$(*p*-N$_3$C$_6$H$_4$COO)$_{(6)}$(NO$_3$)$_2$(DMF)$_4$] (**2-p**), viewed from the side. For clarity, lattice solvent, *tert*-butyl groups, disordered atoms, and hydrogen atoms have been removed.
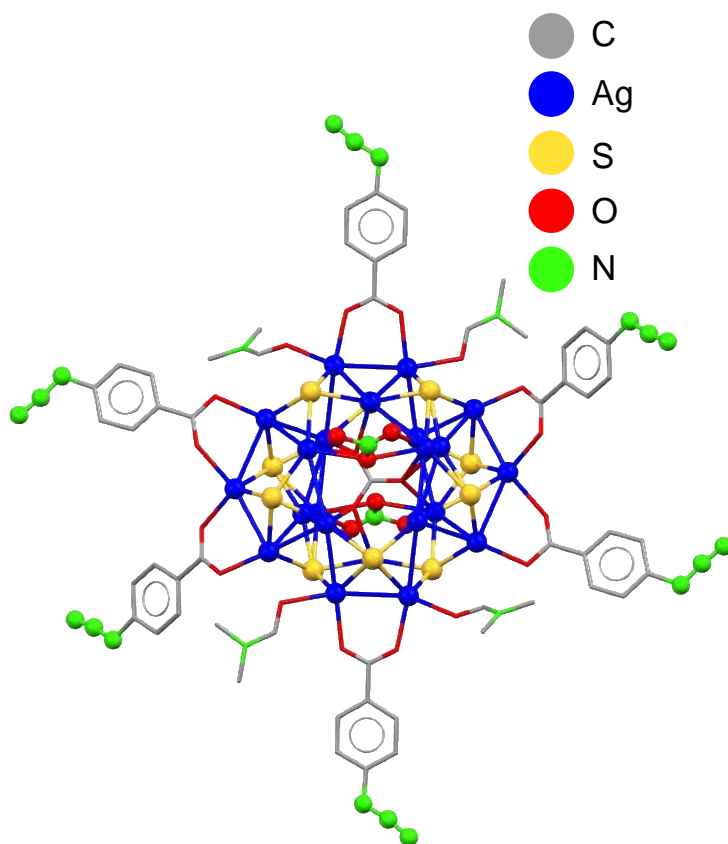
Figure 3.4: Molecular structure of $[CO_3@Ag_{20}(S^tBu)_{10}(p\text{-}N_3C_6H_4COO)_{(6)}(NO_3)_2(DMF)_4]$ (**2-p**), viewed from above. For clarity, lattice solvent, *tert*-butyl groups, disordered atoms, and hydrogen atoms have been removed.
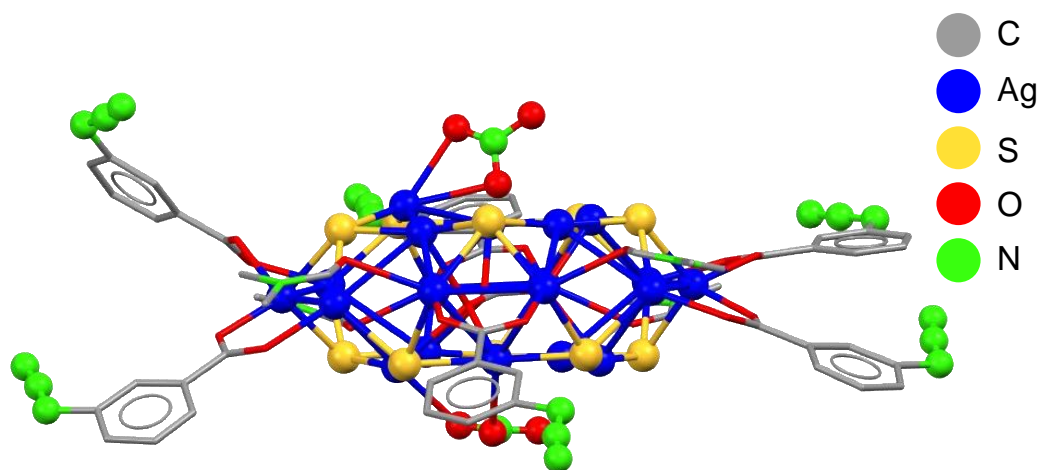
Figure 3.5: Molecular structure of $[CO_3@Ag_{20}(S^tBu)_{10}(m$-$N_3C_6H_4COO)_{(6)}(NO_3)_2(DMF)_4]$ (**2-*m***), viewed from the side. For clarity, lattice solvent, *tert*-butyl groups, disordered atoms, and hydrogen atoms have been removed.
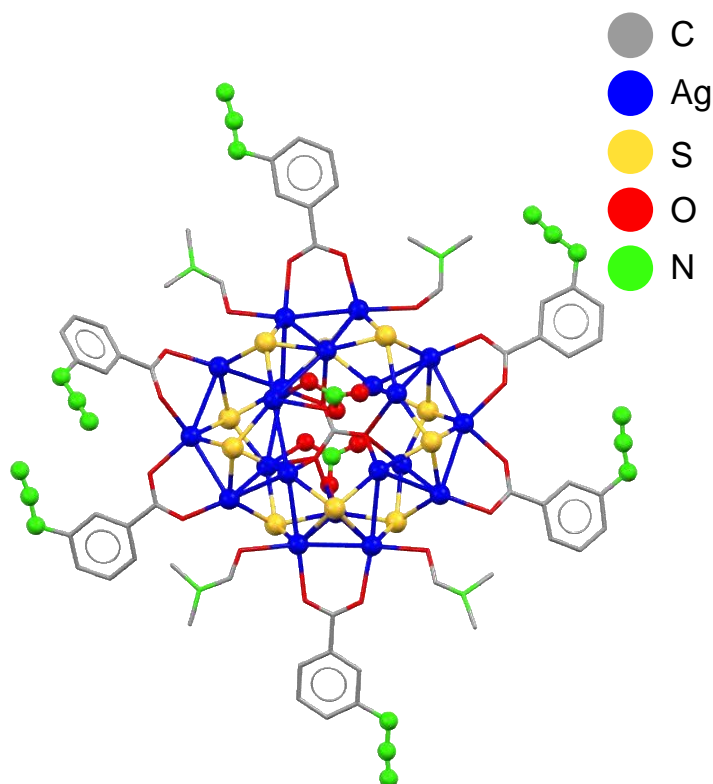
Figure 3.6: Molecular structure of [CO$_3$@Ag$_{20}$(S^{t}Bu)$_{10}$(*m*-N$_3$C$_6$H$_4$COO)$_{(6)}$(NO$_3$)$_2$(DMF)$_4$] (**2-*m***), viewed from above. For clarity, lattice solvent, *tert*-butyl groups, disordered atoms, and hydrogen atoms have been removed.

3.2 Conclusion

In conclusion, this project has been able to demonstrate for the first time an azide-decorated silver nanocluster. The surface reactivity of this cluster was probed successfully with BCN and FcBCN, showing that all surface azides are accessible and reactive. Furthermore, the reaction with FcBCN introduced electrochemical activity into the click product which was not seen in the parent cluster while maintaining the same core geometry, handily demonstrating the merit of using the azide functionality and CS-SPAAC in tandem to change the cluster surface while minimally disturbing the cluster core. It was also discovered that the degree to which carboxylate ligands are present on the cluster can be

finely controlled, giving another handle which can be used to further tailor the surface modification of the cluster towards being easily applicable in a variety of fields.

Future work for this framework will revolve around probing what other structural changes can be made to the cluster. In particular, it is of interest to confirm whether or not it is possible to modify the thiol ligand used as well, as confirmation of this will add yet another degree of modifiability into the system. Also of interest is to probe what degrees of substitution are allowed by the system, as 8-, 6-, and 0- carboxylate substituted clusters have been isolated and structurally characterized by SCXRD, but 4- and 2-carboxylate substituted cluster have yet to be attempted, nor have odd numbered substitutions (7-, 5-, 3-, 1-substituted) been attempted.

3.3   References

1. Li, S.; Du, X.-S.; Li, B.; Wang, J.-Y.; Li, G.-P.; Gao, G.-G.; Zang S-Q.. *J. Am. Chem. Soc.* **2018**, *140* (2), 594-597

2. Gobbo, P.; Gunawardene, P.; Luo, W.; Workentin, M. S. *Synlett* **2015**, *26* (9), 1169-1174

3. Li, H.; Cheng, F.; Duft, A. M.; Adronov, A. *J. Am. Chem. Soc.* **2005**, *127* (41), 14518-14524

4. Meinhardt, T.; Lang, D.; Dill, H.; Krueger, A. *Adv. Funct. Mater.* **2011**, *21* (3), 494-500

5. Saxon, E.; Bertozzi, C. R. *Science* **2000**, *287* (5460), 2007-2010

6. Saxon, E.; Armstrong, J. I.; Bertozzi, C. R. *Org. Let.* **2000**, *2* (14), 2141-2143

7. (a) Staudinger, H.; Meyer, J. *Helv. Chim. Acta* **1919**, *2* (1), 635−646; (b) Taylor, S. D.; Lohani, C. R. *Org. Lett.* **2016**, *18* (17), 4412−4415

8. Fantoni, N. Z.; El-Sagheer, A. H.; Brown, T. *Chem. Rev.* **2021**, *121* (12), 7122-7154

9. (a) Biswas, S.; Das, A. K.; Manna, S. S.; Pathak, B.; Mandal, S. *Chem. Sci.***2022**, *13* (38), 11394-11404. (b) van der Linden, M.; van Bunningen, A. J.; Amidani, L.; Bransen, M.; Elnaggar, H.; Glatzel, P.; Meijerink, A.; de Groot, F. M. F. *ACS Nano* **2018**, *12* (12), 12751-12760

<center>Appendices</center>

4 Appendix A

4.1 Reagents and Instrumentation

3-aminobenzoic acid, dimethylformamide (DMF), and sodium nitrite were purchased from Caledon. Acetonitrile (MeCN, HPLC grade), 4-aminobenzoic acid, N,N'-dicyclohexylcarbodiimide (DCC), hydrochloric acid (37% w/w), and sodium azide were purchased from Sigma-Aldrich. Silver nitrate and anhydrous magnesium sulfate was purchased from Fischer Chemical. Triethylamine was purchased from EDM Millipore. Ferrocenecarboxylic acid was obtained from Oakwood Chemical. 4-Dimethyl aminopyridine (DMAP) was obtained from Alfa-Aesar. Common laboratory solvents (ethyl acetate, dichloromethane (DCM)) were sourced from Fischer Chemical and Sigma-Aldrich. All reagents and solvents were used as received without further purification.

Silver *tert*-butylthiolate was synthesized according to a literature procedure.[1] *Exo*-bicyclo[6.1.0]non-4-yn-9-ylmethanolol (BCN) was also prepared according to a literature procedure.[2]

IR Spectra were collected on a PerkinElmer Spectrum Two FT-IR Spectrometer in the 500 – 4000 cm^{-1} window. ^{1}H and ^{13}C{^{1}H} NMR spectra were collected on a Bruker 400 MHz spectrometer in either CDCl$_3$ or DMSO-d_6. The multiplicity of peaks seen in the ^{1}H NMR were assigned as either singlet (s), doublet (d), triplet (t), quartet (q), multiplet (m), or broad (br). UV-Vis. absorbance spectra were collected on a CARY 100. Fluorescence spectra were collected on a Photon Technology International fluorometer with MD-5020 motor controls, SC-500 shutter controls, an LPS-220B lamp power source and an 814 photomultiplier detection system.

Transmission electron microscopy (TEM) images were collected on a Titan LB operated at 300 kV. Samples were sonicated in ethanol and drops of solution were deposited ultrathin carbon grids. X-ray photoelectron spectroscopy (XPS) analyses were performed

with a Kratos Supra with a monochromatic Al Kα as an X-ray source. Charge correction and calibration to 284.8 eV was done using the component C-C/C-H C1s peak. CasaXPS Version 2.3.24PR1.0 was used to fit the spectra using Shirley background.

4.2   Synthetic Procedures

Synthesis of *p*-azidobenzoic acid, *p*-N$_3$-C$_6$H$_4$COOH
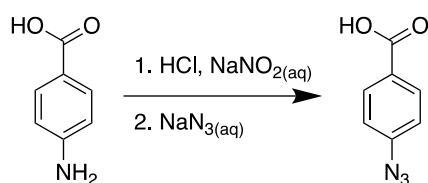
P-Azidobenzoic acid was synthesized according to a literature procedure.[3,4] In a 100 mL beaker, *p*-aminobenzoic acid (3.001 g, 21.88 mmol) and 60.0 mL 5% HCl were combined. The white suspension was stirred and cooled on ice. A solution of NaNO$_2$ (1.808 g, 26.20 mmol in 3.0 mL H$_2$O) was added dropwise, resulting in a yellow solution. After 35 mins., a solution of NaN$_3$ (2.129 g, 32.15 mmol in 3.1 mL H$_2$O) was added dropwise to the solution, and the mixture was allowed to warm to room temperature over 10 mins. The product was extracted from the aqueous mixture using ethyl acetate, dried with anhydrous magnesium sulfate, filtered, and obtained as a pale orange powder after removing the solvent via rotary evaporation. Yield = 3.552 g (>99%). ^{1}H NMR (DMSO-d_6, 400 MHz): δ (ppm) 11.69 (s, 1H), 8.11 (d, 2H), 7.11 (d, 2H). IR: 2099 cm^{-1}

Synthesis of [(CO₃)@Ag₂₀(SᵗBu)₁₀(p-N₃-C₆H₄COO)₈(DMF)₄] (1-p)

$$10 \ AgNO_3 + 10 \ [AgS^tBu]_n + 8 \quad \xrightarrow{\text{MeCN, DMF}} \quad 1 \ [CO_3@Ag_{20}(S^tBu)_{10}(p\text{-}N_3\text{-}C_6H_4COO)_8(DMF)_4]$$
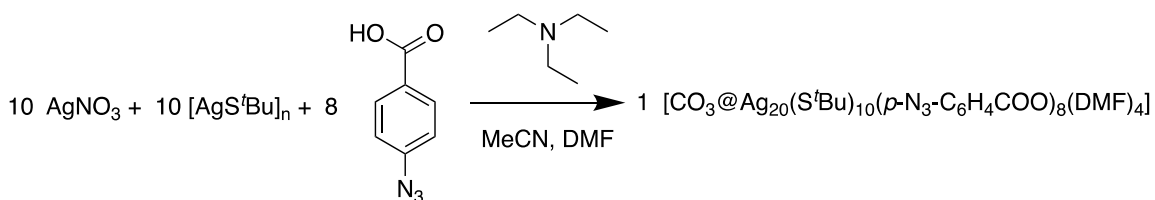
In a 600 mL beaker, AgNO₃ (105.9 mg, 0.623 mmol) and [AgSᵗBu]ₙ (122.1 mg, 0.620 mmol) were dissolved in 25.0 mL MeCN and 25.0 mL DMF. The mixture was sonicated, giving yellow solution. The solution was stirred as p-N₃-C₆H₄COOH (81.4 mg, 0.499 mmol) and 40 drops of triethylamine were added to the reaction mixture. The mixture was allowed to slowly evaporate for 2 days, yielding colourless block crystals. The crystals were washed with 3 x 10 ml Et₂O. Yield = 232.3 mg (80.0%). ¹H NMR (CDCl₃, 400 MHz): δ (ppm) 8.16 (d, 16H), 8.03 (s, 4H), 7.06 (d, 16H), 2.96 (s, 12H), 2.89 (s, 12H), 1.66 (s, 90H). ¹³C{¹H} NMR (CDCl₃, 75 MHz): 172.3, 162.8, 142.5, 133.5, 132.0, 118.5, 51.8, 37.6, 36.7, 31.6. IR: 2115 cm⁻¹. Elemental analysis calcd. (%) for C₁₀₉H₁₅₀Ag₂₀N₂₈O₂₃S₁₀ (4698.54): C, 27.86; H, 3.22; Ag, 45.92; N, 8.35; O, 7.83; S, 6.82; found: C, 28.28; H, 2.80; N, 8.12; S, 9.41.

Synthesis of [(CO₃)@Ag₂₀(4-N₃-C₆H₄COO)₆(SᵗBu)₁₀(NO₃)₂(DMF)₄] (2-p)

$$10 \ AgNO_3 + 10 \ [AgS^tBu]_n + 6 \quad \xrightarrow{\text{MeCN, DMF}} \quad 1 \ [CO_3@Ag_{20}(S^tBu)_{10}(p\text{-}N_3\text{-}C_6H_4COO)_6(NO_3)_2(DMF)_4]$$
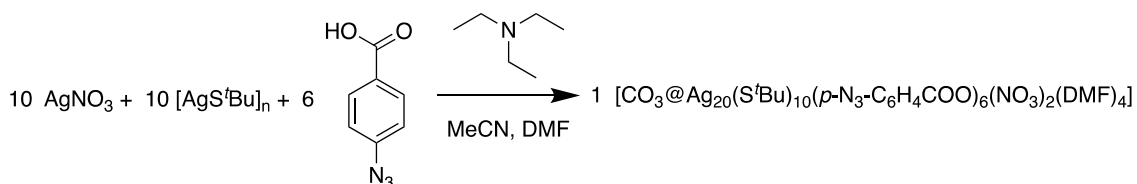
In a 125 mL Erlenmeyer flask, AgNO₃ (106.1 mg, 0.625 mmol) and [AgSᵗBu]ₙ (122.6 mg, 0.622 mmol) were dissolved in 25.0 mL MeCN and 25.0 mL DMF. The mixture was sonicated 10 sec., giving yellow solution. The solution was stirred as p-N₃-C₆H₄COOH (61.6 mg, 0.378 mmol) and 40 drops of triethylamine were added to the reaction mixture.

The mixture was allowed to slowly evaporate for 18.5 hr., yielding shiny colourless crystals. The reaction mixture was decanted into a 250 mL beaker, and the crystals were washed with 3x 25 ml Et_2O and dried under high vacuum. More crystalline product was collected by allowing the reaction mixture to evaporate for an additional 2 days. Yield = 227.1 mg (81.5%). ^1H NMR ($CDCl_3$, 400 MHz): δ (ppm) 8.18 (s, 12H), 8.07 (s, 4H), 7.08 (d, 12H), 2.99 (s, 12H), 2.93 (s, 12H), 1.68 (s, 90H). Elemental analysis calcd. (%) for $C_{95}H_{142}Ag_{20}N_{24}O_{25}S_{10}$ (4698.54): C, 25.37; H, 3.18; Ag, 47.96; N, 7.47; O, 8.89; S, 7.13; found: TBD

Synthesis of *m*-azidobenzoic, *m*-N₃-C₆H₄COOH
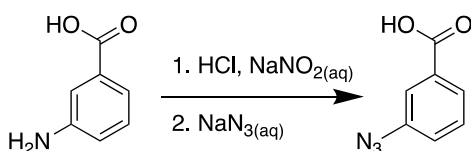
M-azidobenzoic acid was synthesized similarly to *p*-azidobenzoic acid,[3,4] except *m*-aminobenzoic acid was used in place of *p*-aminobenzoic acid. Yield = 3.021 g (84.6%) ^1H NMR (DMSO-d_6, 400 MHz): δ (ppm) 12.57 (s, 1H), 7.16 (t, 1H), 7.09 (q, 1H), 7.06 (dt, 1H), 6.75 (dt, 1H). IR: 2121 cm^{-1}

Synthesis of [(CO₃)@Ag₂₀(S^{t}Bu)₁₀(*m*-N₃-C₆H₄COO)₈(DMF)₄] (1-*m*)
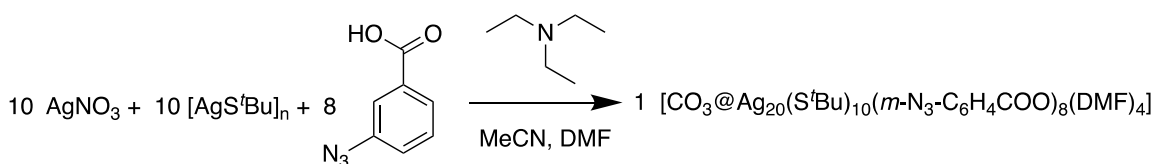
In a 125 mL Erlenmeyer flask, $AgNO_3$ (105.8 mg, 0.623 mmol) and [AgS^{t}Bu]$_n$ (122.7 mg, 0.623 mmol) were dissolved in 22.0 mL MeCN and 26.0 mL DMF. The mixture was sonicated 30 sec., giving yellow solution. The solution was stirred as *m*-N₃-C₆H₄COOH

(81.4 mg, 0.499 mmol) and 40 drops of triethylamine were added to the reaction mixture. The mixture was allowed to slowly evaporate for 5 days, yielding colourless block crystals. The crystals were washed with 3x 10 ml Et$_2$O. Yield = 226.4 mg (77.8%). ^{1}H NMR (CDCl$_3$, 400 MHz): δ (ppm) 8.06 (s, 4H), 7.94 (d, 8H), 7.86 (d, 8H), 7.40 (t, 8H), 7.12 (d, 8H), 2.97 (s, 12H), 2.90 (s, 12H), 1.67 (s, 90H). ^{13}C{^{1}H} NMR (CDCl$_3$, 75 MHz): 172.0, 162.8, 139.9, 138.6, 129.4, 128.7, 126.8, 121.5, 120.6, 51.6 – 50.9, 37.6, 36.7, 31.6. IR: 2111 cm^{-1}. Elemental analysis calcd. (%) for C$_{109}$H$_{150}$Ag$_{20}$N$_{28}$O$_{23}$S$_{10}$ (4698.54): C, 27.86; H, 3.22; Ag, 45.92; N, 8.35; O, 7.83; S, 6.82; found: TBD

Synthesis of [(CO$_3$)@Ag$_{20}$(m-N$_3$-C$_6$H$_4$COO)$_6$(S^{t}Bu)$_{10}$(NO$_3$)$_2$(DMF)$_4$] (2-*m*)

$$10 \ AgNO_3 + 10 \ [AgS^tBu]_n + 6 \quad \xrightarrow[\text{MeCN, DMF}]{} \quad 1 \ [CO_3@Ag_{20}(S^tBu)_{10}(m\text{-}N_3\text{-}C_6H_4COO)_6(NO_3)_2(DMF)_4]$$
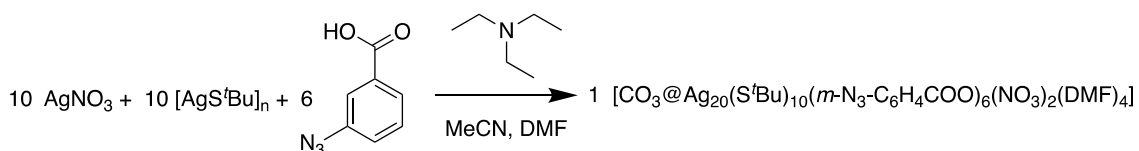
In a 600 mL beaker, AgNO$_3$ (105.4 mg, 0.620 mmol) and [AgS^{t}Bu]$_n$ (121.9 mg, 0.619 mmol) were dissolved in 25.0 mL MeCN and 25.6 mL DMF. The mixture was sonicated 30 sec., giving fine suspension. An additional 10.3 mL MeCN and 16.8 mL DMF were added, and the solution was sonicated again until a clear yellow solution was obtained. The solution was stirred as *m*-N$_3$-C$_6$H$_4$COOH (61.2 mg, 0.375 mmol) and 40 drops of triethylamine were added. The mixture covered with a watch glass and allowed to slowly evaporate for 18 hrs., resulting in a colourless powder precipitating out of solution. The solution was decanted to a separate vessel and allowed to evaporate further. The precipitate was dissolved in 50 mL chloroform and filtered via filter pipette into a 125 mL Erlenmeyer flask, separating a black solid out of the mixture. The filtered solution was allowed to evaporate until ~5 mL of solution remained, at which point the solution was store at -15 °C for 5 days. When no precipitation was evident, the contents of the flask were allowed to evaporate overnight, yielding colourless crystals. The crystals were washed with 3x 15 ml Et$_2$O and dried under high vacuum. Yield = 119.8 mg (43.0%). ^{1}H NMR (CDCl$_3$, 400

MHz): δ (ppm) 8.05 (s, 4H), 7.94 (d, 6H), 7.86 (t, 6H), 7.40 (t, 6H), 7.12 (d, 6H), 2.97 (s, 12H), 2.90 (s, 12H), 1.67 (s, 90H). Elemental analysis calcd. (%) for $C_{95}H_{142}Ag_{20}N_{24}O_{25}S_{10}$ (4698.54): C, 25.37; H, 3.18; Ag, 47.96; N, 7.47; O, 8.89; S, 7.13; found: TBD

Synthesis of [(CO₃)@Ag₂₀(S*ᵗ*Bu)₁₀(*p*-HOC₁₀H₁₃N₃-C₆H₄COO)₈(DMF)₄] (1-*p* + BCN)
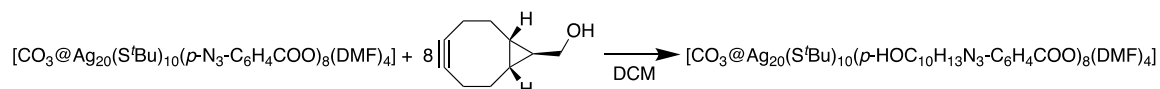
In a 5 mL vial, BCN (2.2 mg, 0.015 mmol) and **1-*p*** (7.8 mg, 0.0017 mmol) were combined and dissolved in 1 mL DCM and stirred to give a clear, colourless solution. After 5 min., the mixture becomes cloudy. After 15 min. the mixture is completely opaque and colourless. The white precipitate was isolated and washed with 5 mL DCM. Yield = 2.3 mg (23%). ^{1}H NMR (DMSO-d_6, 400 MHz): δ (ppm) 8.21 (s, 16H), 7.51 (s, 16H), 4.31 (s, 8H), 3.48 (br t, 19H), 3.05 (br, 10H), 2.87 (br, 20H), 2.63 (br, 18H), 2.10 (br, 16H), 1.63-1.58 (m, 90H), 1.00-0.80 (br m, 24H).

Synthesis of [(CO₃)@Ag₂₀(S*ᵗ*Bu)₁₀(*m*-HOC₁₀H₁₃N₃-C₆H₄COO)₈(DMF)₄] (1-*m* + BCN)
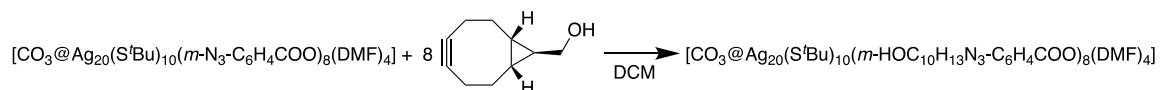
In a 5 mL vial, BCN (3.0 mg, 0.020 mmol) and **1-*m*** (4.5 mg, 0.00096 mmol) were combined and dissolved in 1 mL DCM and stirred to give a clear, pale-yellow solution. After 5 min., the mixture becomes cloudy. After 15 min. the mixture is completely opaque and light brown/yellow. The tan precipitate was isolated and washed with 5 mL DCM, giving a white solid. Yield = 1.2 mg (34%) ^{1}H NMR (DMSO-d_6, 400 MHz): δ (ppm) 8.27-8.00 (br m, 16H), 7.71 (s, 16H), 4.30 (s, 8H), 3.46 (s, 20H), 3.05 (br, 10H), 2.84 (br, 16H), 2.57 (br, 10H), 2.10 (br, 18H), 1.58-1.48 (m, 90H), 1.00-0.80 (br m, 24H).

Synthesis of *exo*-bicyclo[6.1.0]non-4-yn-9-ylmethylferrocenecarboxylate (FcBCN)
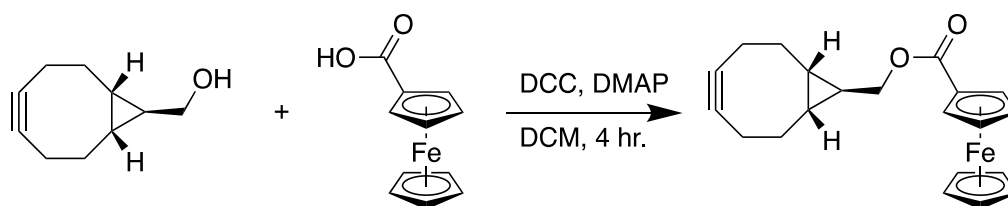
In a RBF ferrocenecarboxylic acid (100 mg, 0.435 mmol), DCC (138 mg, 0.669 mmol) and DMAP (41mg, 0.336 mmol) were combined and dissolved in 5 mL DCM. The resulting orange solution was stirred for 10 mins. before the addition of BCN (100 mg, 0.666 mmol), and then stirred a further 4 hr. The solution was concentrated and purified by column chromatography using DCM as an eluent. The product was collected as the first fraction and crystallized upon removing the solvent by rotary evaporation. Yield = 153.5 mg (68%) ^{1}H NMR (CDCl$_3$): δ (ppm) 4.81 (s, 2H), 4.39 (s, 2H), 4.21 (s, 5H), 4.15 (d, 2H, $^3J_{H-H}$ = 8 Hz), 2.47-2.44 (d, 2H), 2.32-2.19 (m, 2H), 2.19-2.16 (m, 2H), 1.44-1.41 (m, 2H), 0.90-0.70 (m, 4H). ^{13}C{^{1}H} NMR (CDCl$_3$): 171.9, 99.0, d 71.7, 71.4, 70.3, 69.9, 68.4, 33.5, 23.9, 23.2, 21.6.

Synthesis of C$_{28}$H$_{27}$FeN$_3$O$_4$
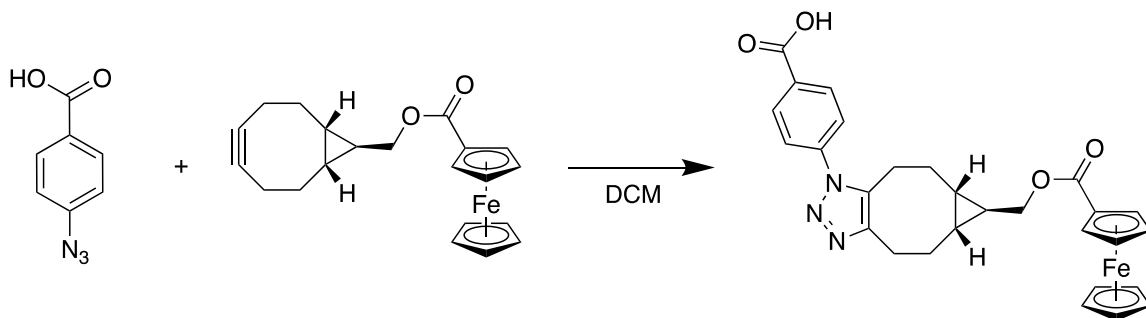
In a 5 mL vial, FcBCN (2.4 mg, 0.015 mmol) was dissolved in 30 drops of DCM, giving an orange solution. This solution was added to a solution of *p*-azidobenzoic acid (1.2 mg,

0.0074 mmol in in 30 drops DCM) in a separate 5 mL vial, and stirred for 20 min. The solvent was allowed to evaporate over 18 hr., and the resulting orange powder was washed with 5 x 2 mL EtOAc and 5 x 5 mL hexanes, and 3 x 5 mL chloroform. The product was dried using a rotary evaporator. ^{1}H NMR (CDCl$_3$, 400 MHz): δ (ppm) 8.30 (s, 2H), 7.60 (br s, 2H), 4.81 (s, 2H), 4.41 (s, 2H), 4.22 (s, 2H), 3.10-2.10 (br m, 8H), 1.57 (br m, 2H), 0.07 (m, 4H).

Synthesis of [(CO$_3$)@Ag$_{20}$(S^{t}Bu)$_{10}$(p-FeC$_{21}$H$_{24}$O$_2$N$_3$-C$_6$H$_4$COO)$_8$(DMF)$_4$] (1-p + FcBCN)
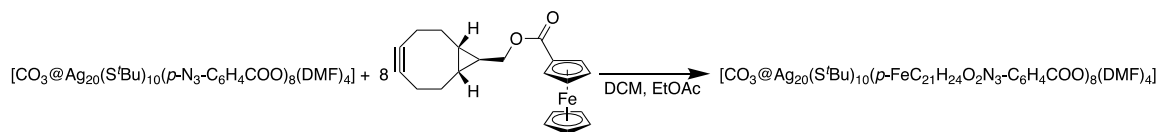
In a 5 mL vial, FcBCN (19.4 mg, 0.054 mmol) was dissolved in 2 mL DCM, giving an orange solution. This solution was added to a pale-yellow solution of **1-p** (30.4 mg, 0.0065 mmol in 0.5 mL DCM) in a separate 5 mL vial, and stirred for 20 min. The solvent was removed under high vacuum and the resulting orange solid was washed with 5 x 1 mL EtOAc and 3 x 4 mL MeCN. The product was dried under high vacuum. Yield = 19.1 mg (38.2%) ^{1}H NMR (CDCl$_3$, 400 MHz): δ (ppm) 8.36 (br s, 16H), 7.40 (br s, 16H), 4.81 (br m, 16H), 4.39 (s, 16H), 4.20-4.10 (br m, 44H), 3.24 (br, 8H), 2.94 (br, 12H), 2.70 (br, 8H), 2.55-2.40 (br, 16H), 1.76-1.48 (br, 90H), 1.37-1.21 (32H), 1.17-0.96 (m, 24H), 0.94-0.80 (m, 24H). ^{13}C{^{1}H} NMR (CDCl$_3$, 75 MHz): 172.0, 71.5, 70.3, 69.9, 37.73, 31.7, 22.8, 14.3.

Synthesis of [(CO$_3$)@Ag$_{20}$(S^{t}Bu)$_{10}$(m-FeC$_{21}$H$_{24}$O$_2$N$_3$-C$_6$H$_4$COO)$_8$(DMF)$_4$] (1-m + FcBCN)
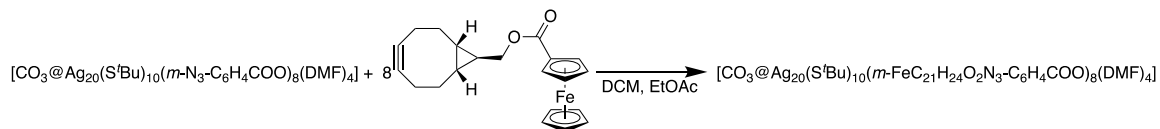
In a 5 mL vial, FcBCN (19.4 mg, 0.054 mmol) was dissolved in 2 mL DCM, giving an orange solution. This solution was added to a pale-yellow solution of **1-m** (30.1 mg, 0.0064 mmol in 0.5 mL DCM) in a separate 5 mL vial, and stirred for 35 min. The solvent was removed under high vacuum and the resulting orange solid was washed with 4 x 2 mL EtOAc and 15 mL MeCN. The product was dried under high vacuum. Yield = 32.2 mg (64.4%) ^{1}H NMR (CDCl$_3$, 400 MHz): δ (ppm) 8.25 (br s, 8H), 8.12 (br s, 8H), 7.61 (br, 8H), 7.40 (br, 8H), 4.78 (br s, 16H), 4.37 (br s, 16H), 4.20-4.10 (br m, 56H), 3.22 (br, 4H), 2.92 (br, 12H), 2.66 (br, 8H), 2.75-2.00 (br, 34H), 1.57 (s, 90H), 1.09 – 0.70 (br m, 30H), 0.07 (m, 44H). ^{13}C{^{1}H} NMR (CDCl$_3$, 75 MHz): 71.5, 70.3, 69.9, 60.6, 37.73, 23.0, 21.2, 14.3.

4.3 Characterization of Materials
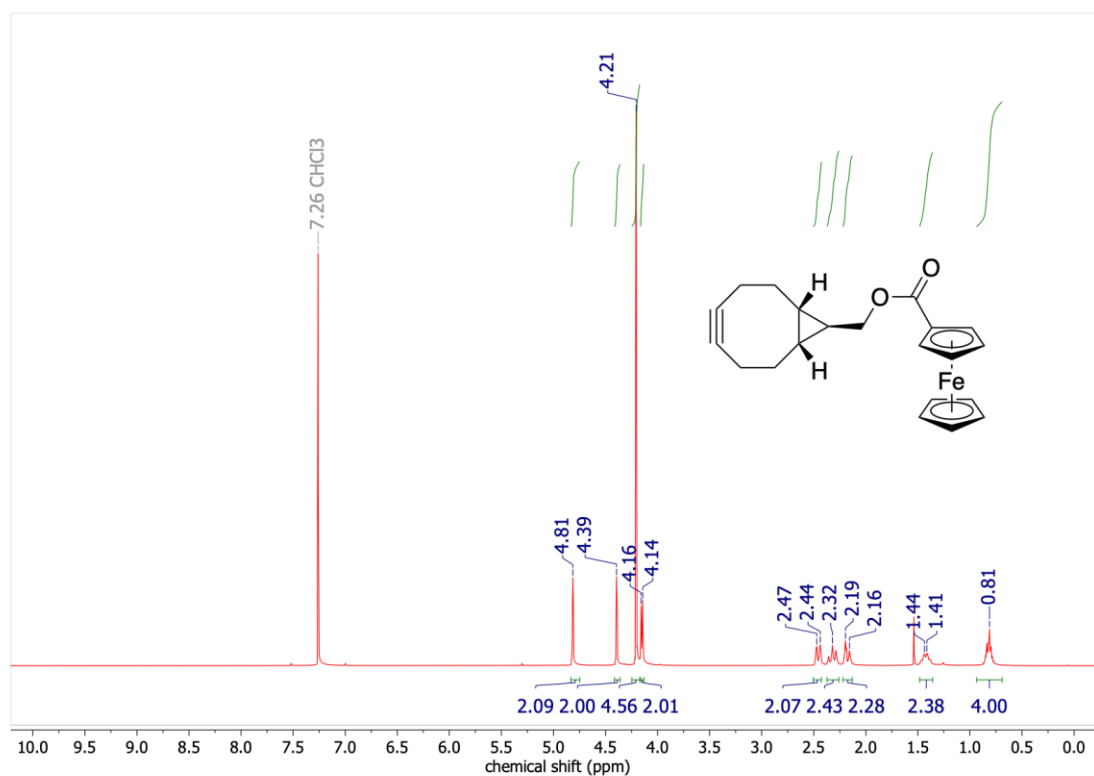
Figure 4.1A: ^{1}H NMR spectrum of *exo*-bicyclo[6.1.0]non-4-yn-9-ylmethylferrocenecarboxylate (FcBCN) in CDCl$_3$.
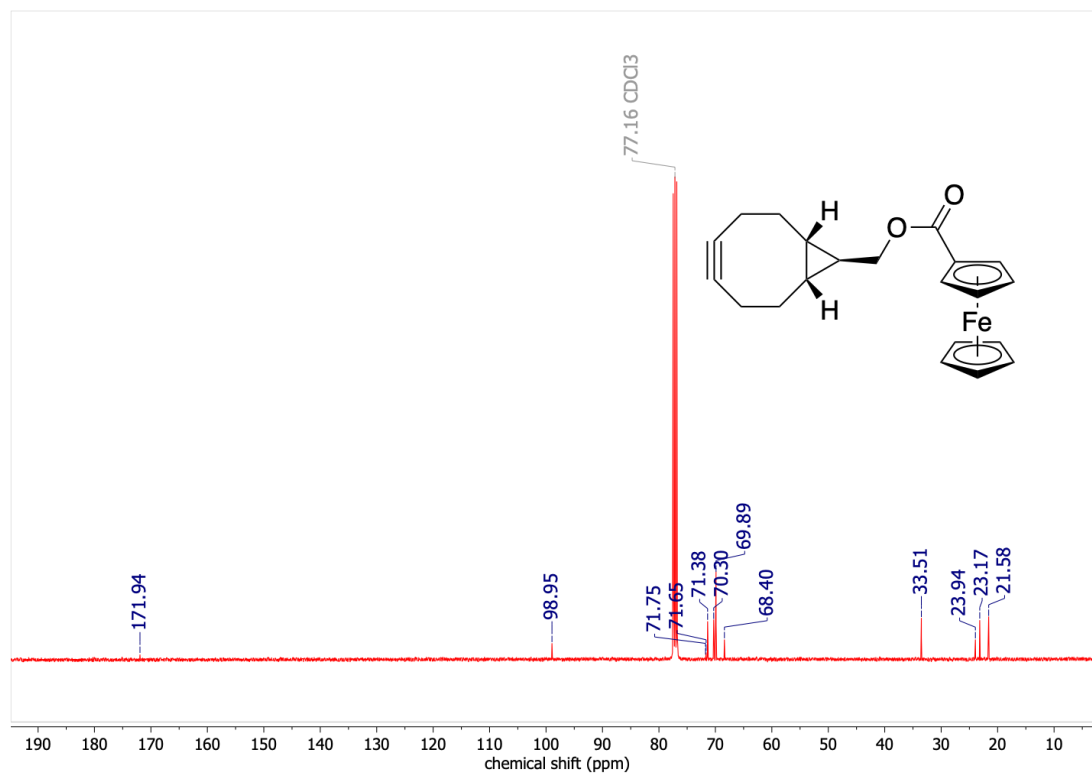
Figure 4.2A: $^{13}C\{^1H\}$ NMR spectrum of *exo*-bicyclo[6.1.0]non-4-yn-9-ylmethylferrocenecarboxylate (FcBCN) in CDCl$_3$.
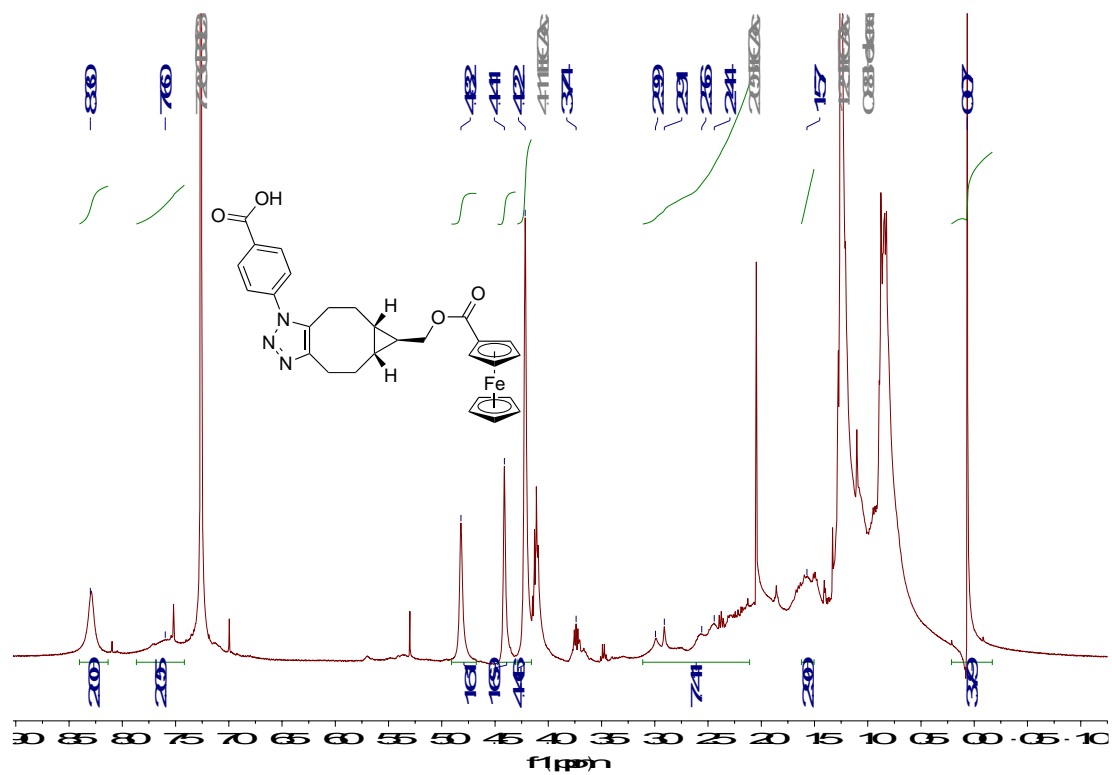
Figure 4.3A: ^{1}H NMR spectrum of *p*-azidobenzoic acid + *exo*-bicyclo[6.1.0]non-4-yn-9-ylmethylferrocenecarboxylate (FcBCN) in CDCl$_3$.
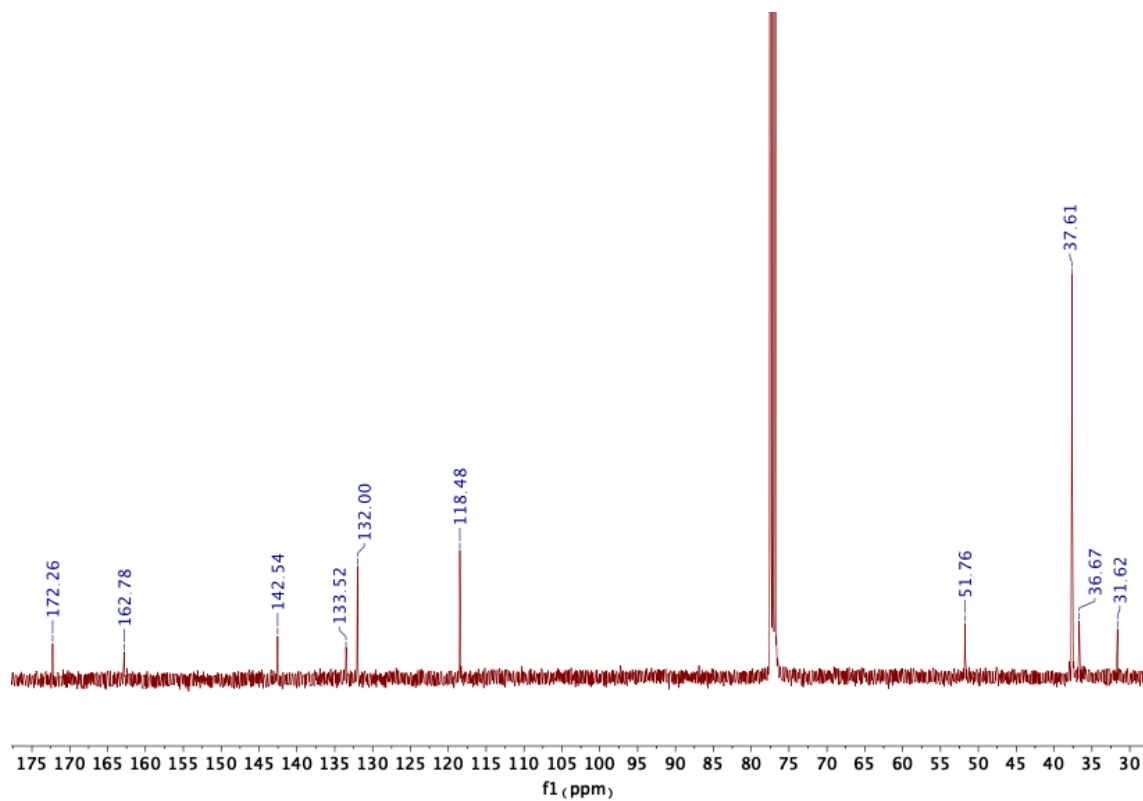
Figure 4.4A: $^{13}C\{^1H\}$ NMR spectrum of $[(CO_3)@Ag_{20}(S^tBu)_{10}(p\text{-}N_3\text{-}C_6H_4COO)_8(DMF)_4]$ (**1-p**) in $CDCl_3$.
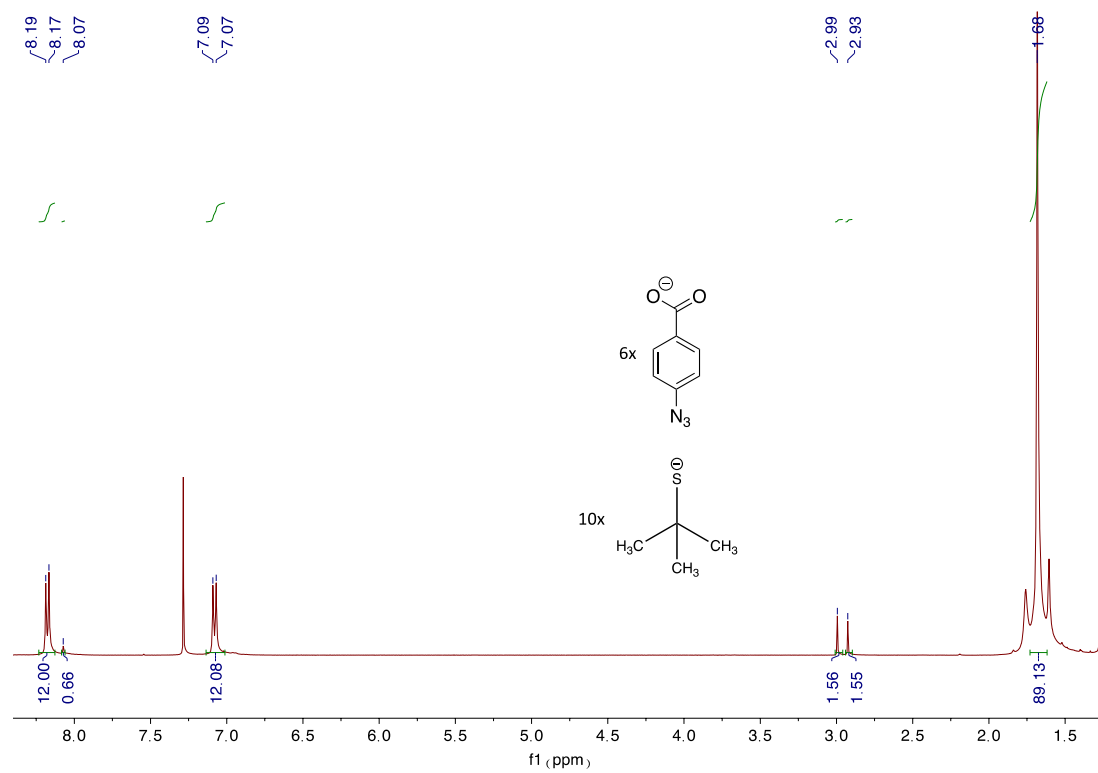
Figure 4.5A: ^{1}H NMR spectrum of [(CO$_3$)@Ag$_{20}$(S^{t}Bu)$_{10}$(*p*-N$_3$-C$_6$H$_4$COO)$_6$(NO$_3$)$_2$(DMF)$_4$] (**2-*p***) in CDCl$_3$.
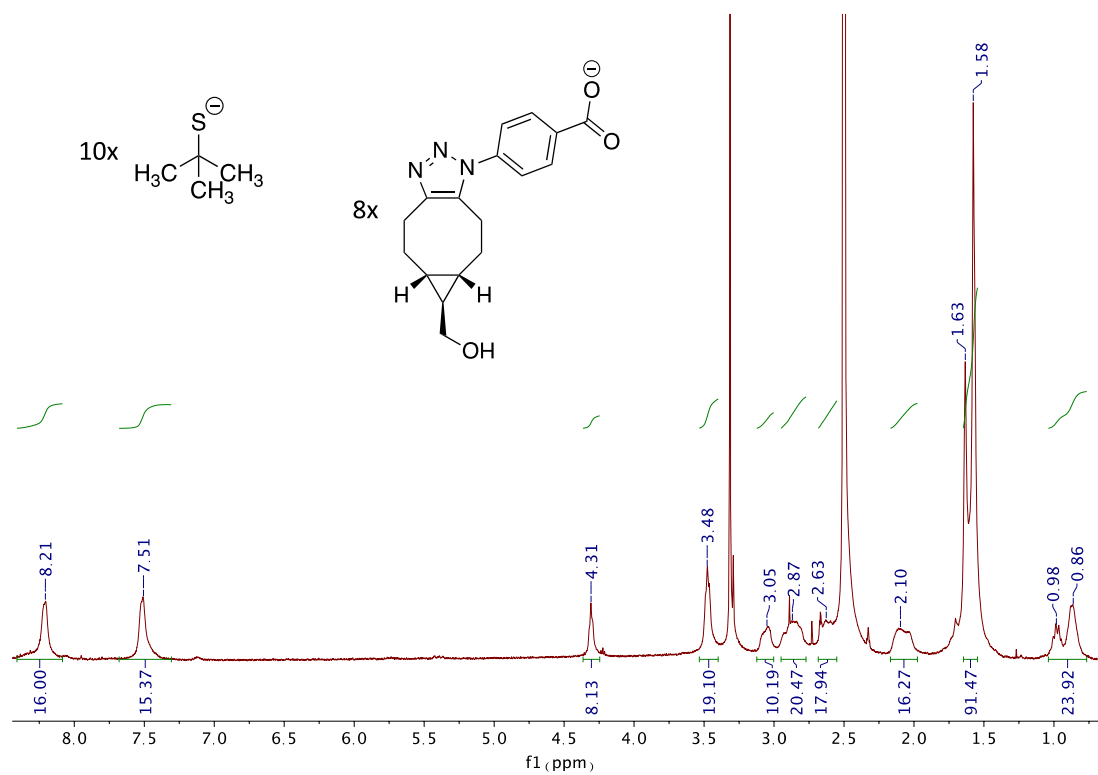
Figure 4.6A: ^1H NMR spectrum of $[(CO_3)@Ag_{20}(S^tBu)_{10}(p\text{-}HOC_{10}H_{13}N_3\text{-}C_6H_4COO)_8(DMF)_4]$ (**1-p** + BCN) in DMSO-d_6.
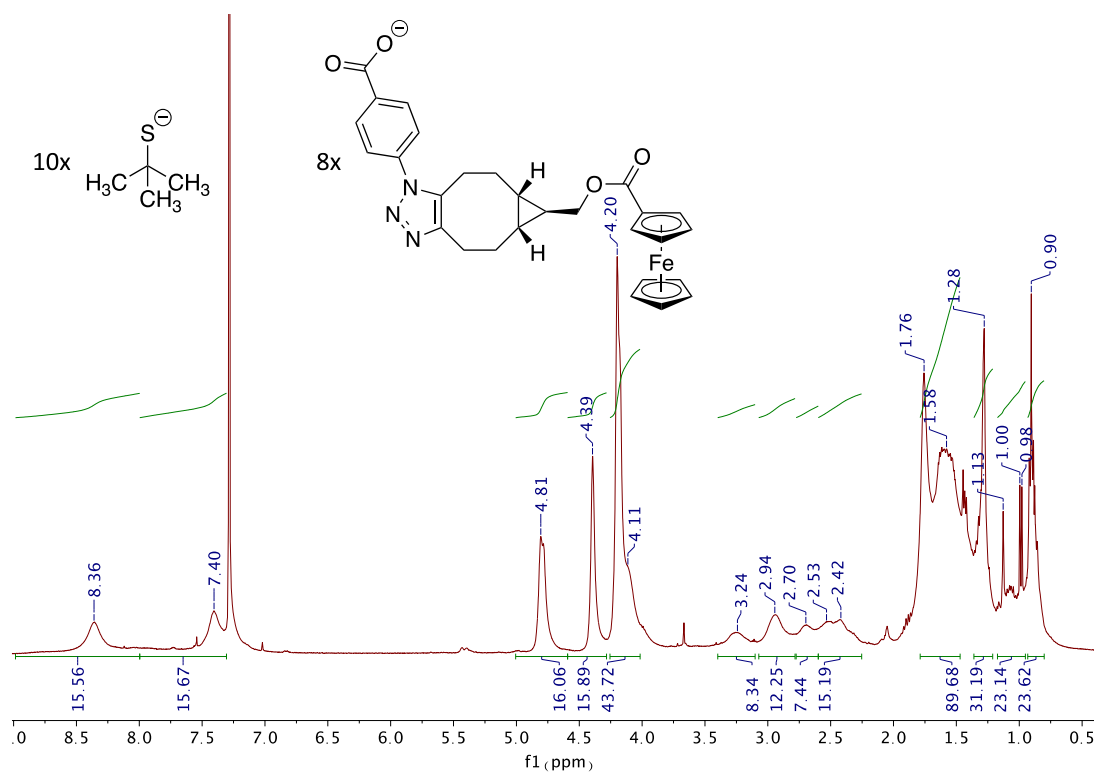
Figure 4.7A: ^{1}H NMR spectrum of $[(CO_3)@Ag_{20}(S^tBu)_{10}(p\text{-}FeC_{21}H_{24}O_2N_3\text{-}C_6H_4COO)_8(DMF)_4]$ (**1-p** + FcBCN) in CDCl$_3$.
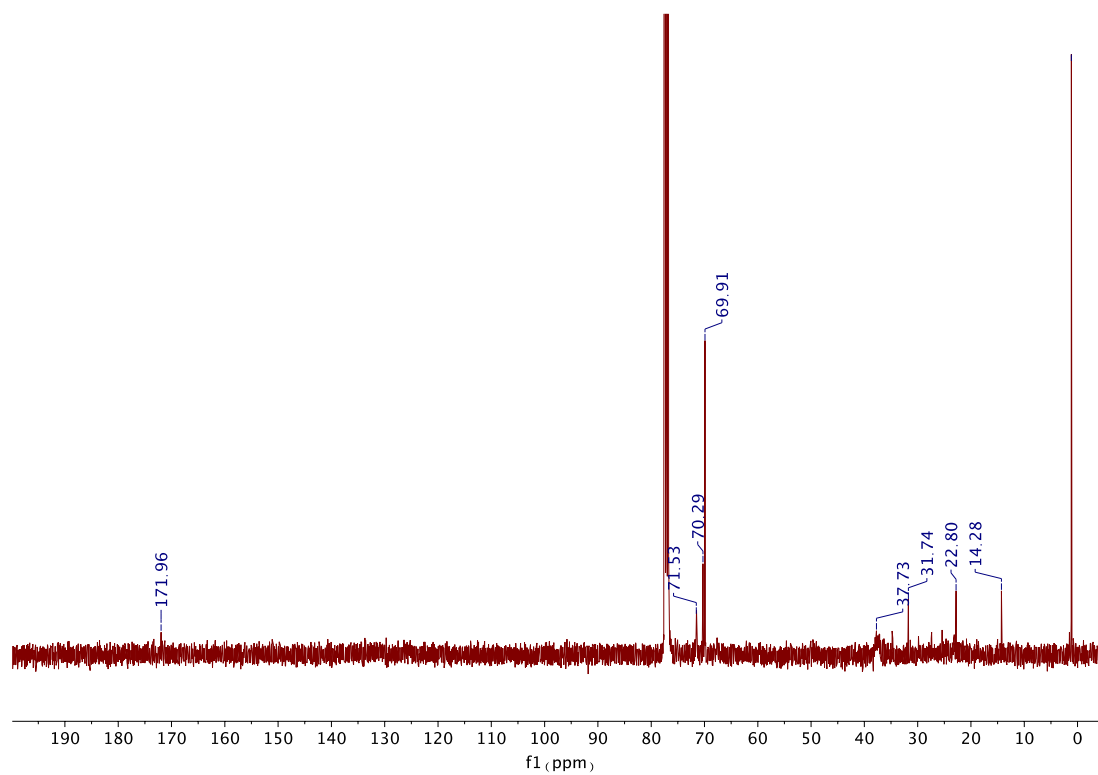
Figure 4.8A: $^{13}C\{^1H\}$ NMR spectrum of [(CO$_3$)@Ag$_{20}$(S^{t}Bu)$_{10}$(p-FeC$_{21}$H$_{24}$O$_2$N$_3$-C$_6$H$_4$COO)$_8$(DMF)$_4$] (**1-p** + FcBCN) in CDCl$_3$.
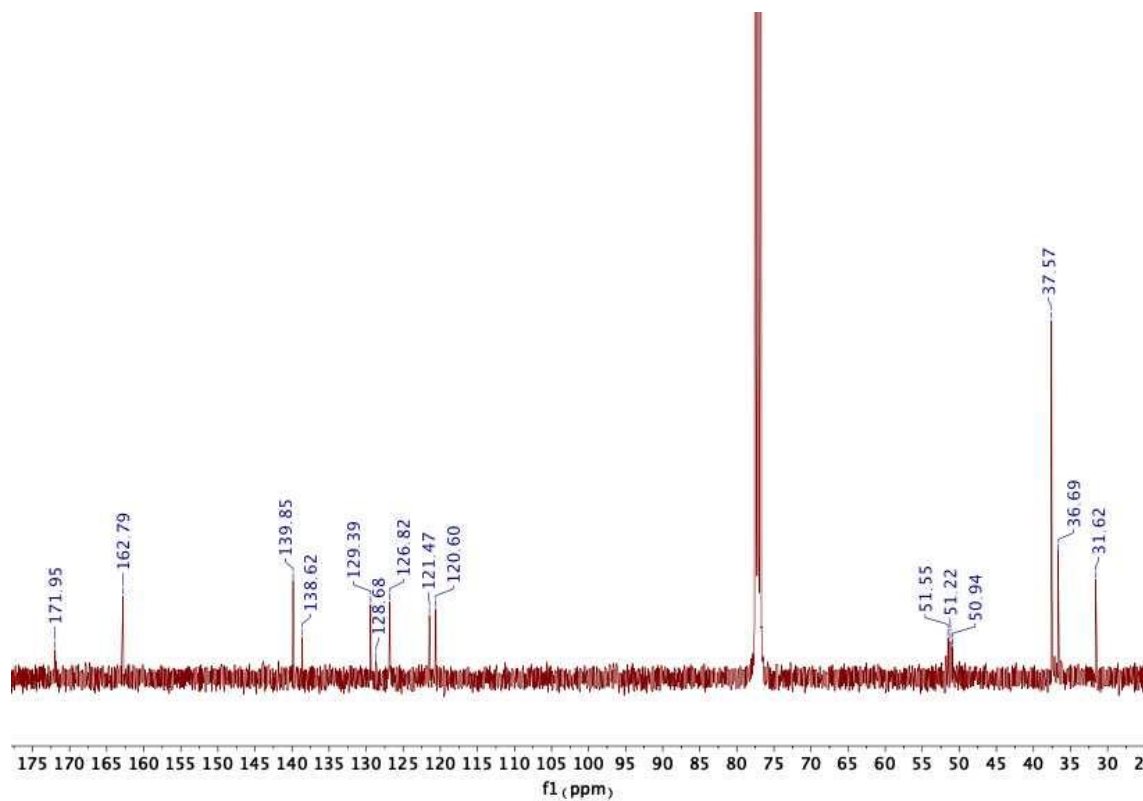
Figure 4.9A: $^{13}C\{^{1}H\}$ NMR spectrum of $[(CO_3)@Ag_{20}(S^tBu)_{10}(m\text{-}N_3\text{-}C_6H_4COO)_8(DMF)_4]$ (**1-*m***) in $CDCl_3$.
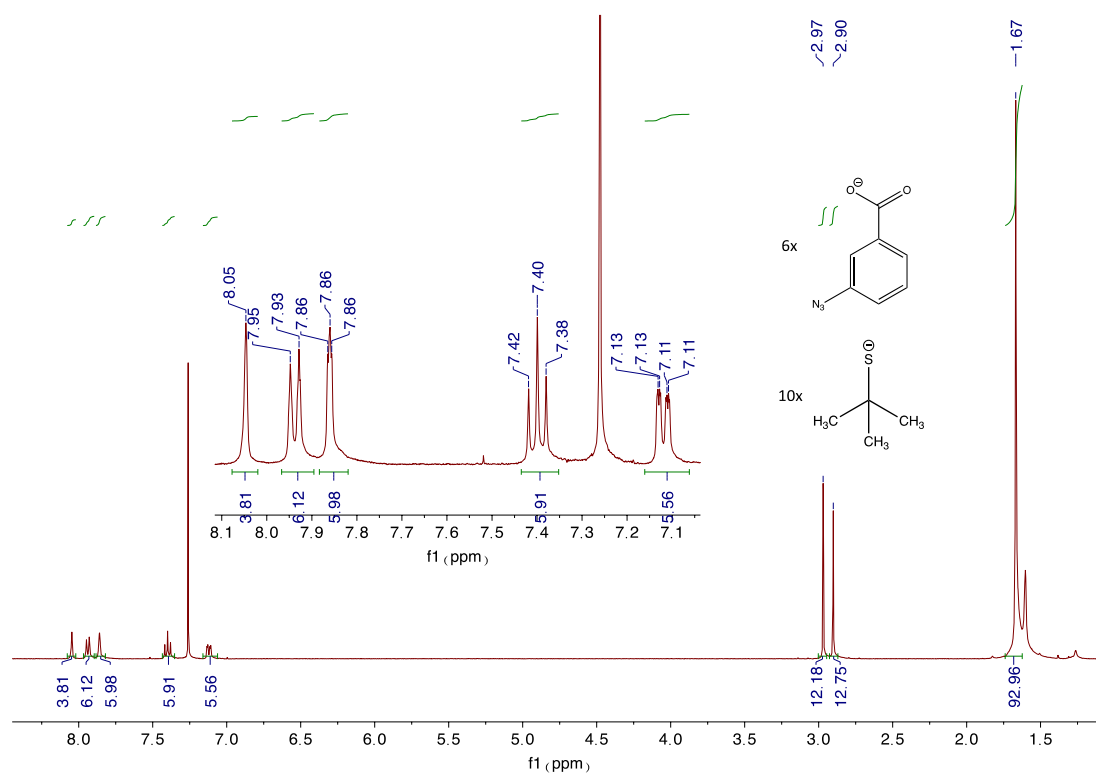
Figure   4.10A: ^{1}H   NMR   spectrum   of $[(CO_3)@Ag_{20}(S^tBu)_{10}(m\text{-}N_3\text{-}C_6H_4COO)_6(NO_3)_2(DMF)_4]$ (**2-*m***) in CDCl$_3$.
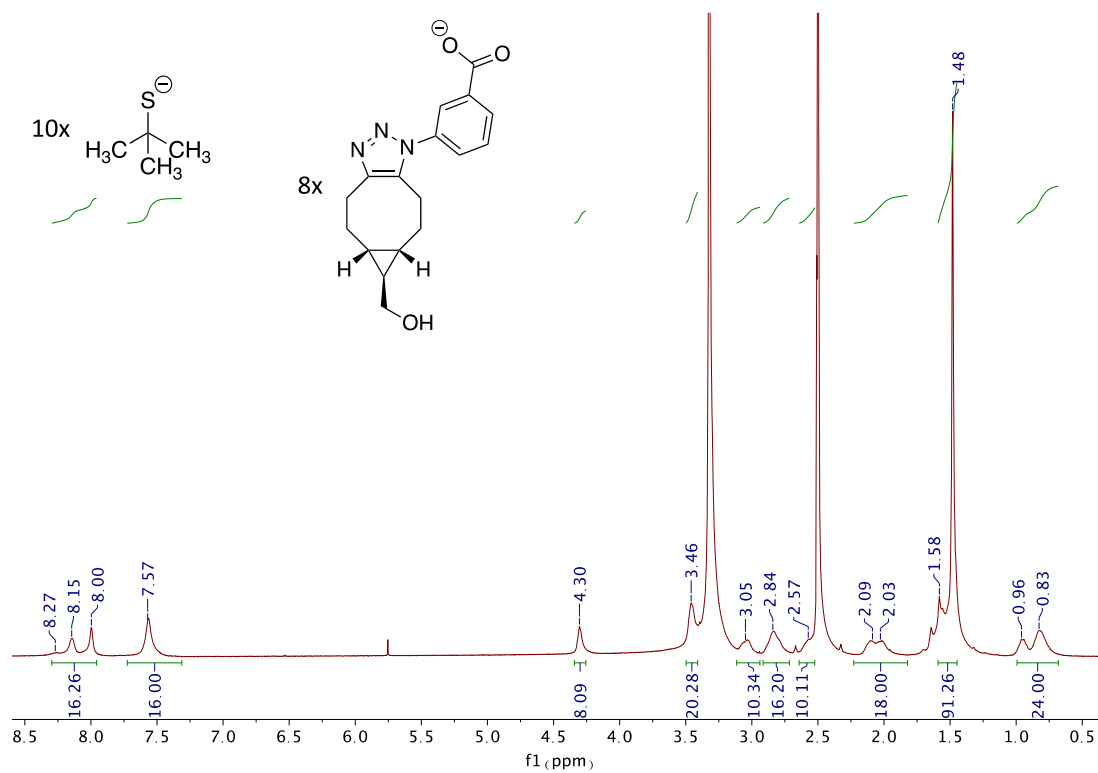
Figure 4.11A: ^{1}H NMR spectrum of $[(CO_3)@Ag_{20}(S^tBu)_{10}(m\text{-}HOC_{10}H_{13}N_3\text{-}C_6H_4COO)_8(DMF)_4]$ (**1-*m*** + BCN) in DMSO-d_6.
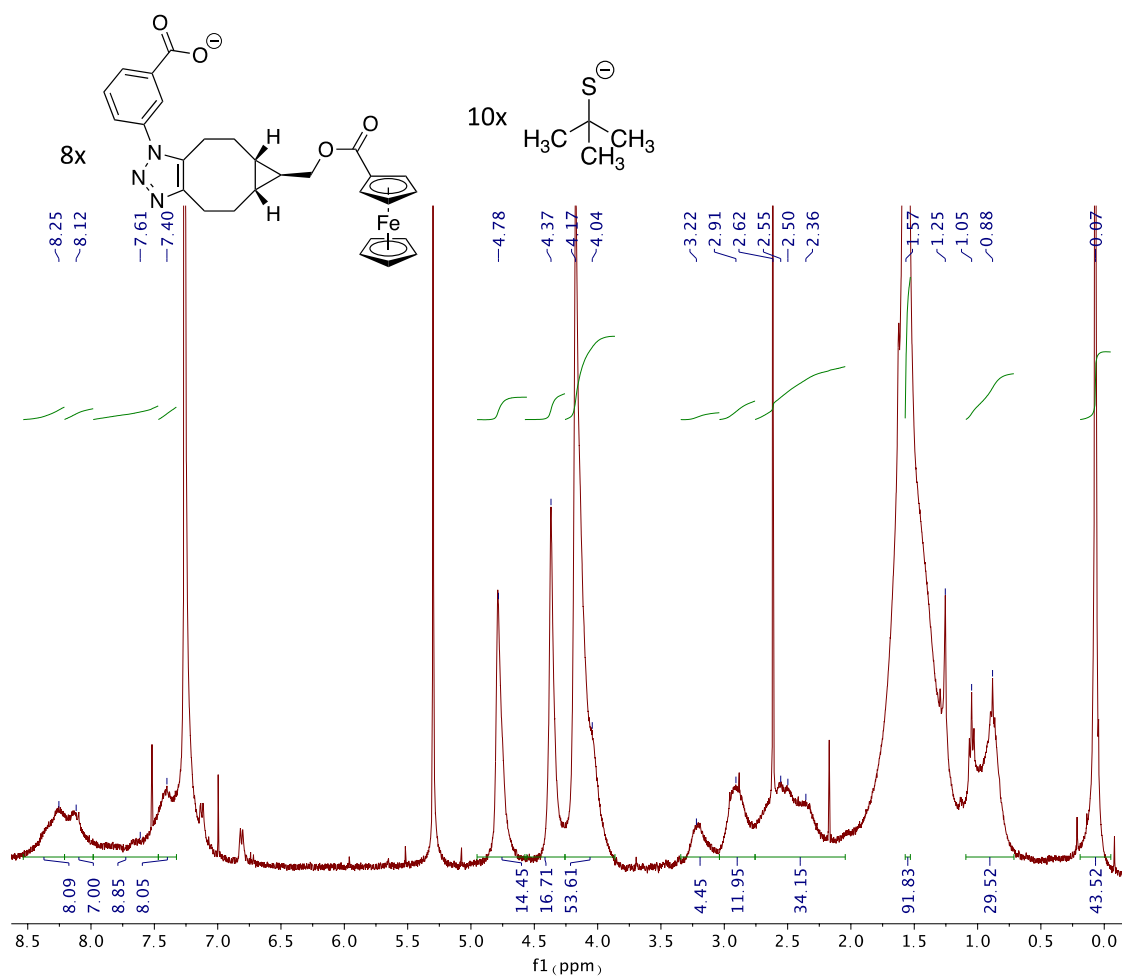
Figure 4.12A: ^{1}H NMR spectrum of $[(CO_3)@Ag_{20}(S^tBu)_{10}(m\text{-}FeC_{21}H_{24}O_2N_3\text{-}C_6H_4COO)_8(DMF)_4]$ (**1-*m*** + FcBCN) in CDCl$_3$.
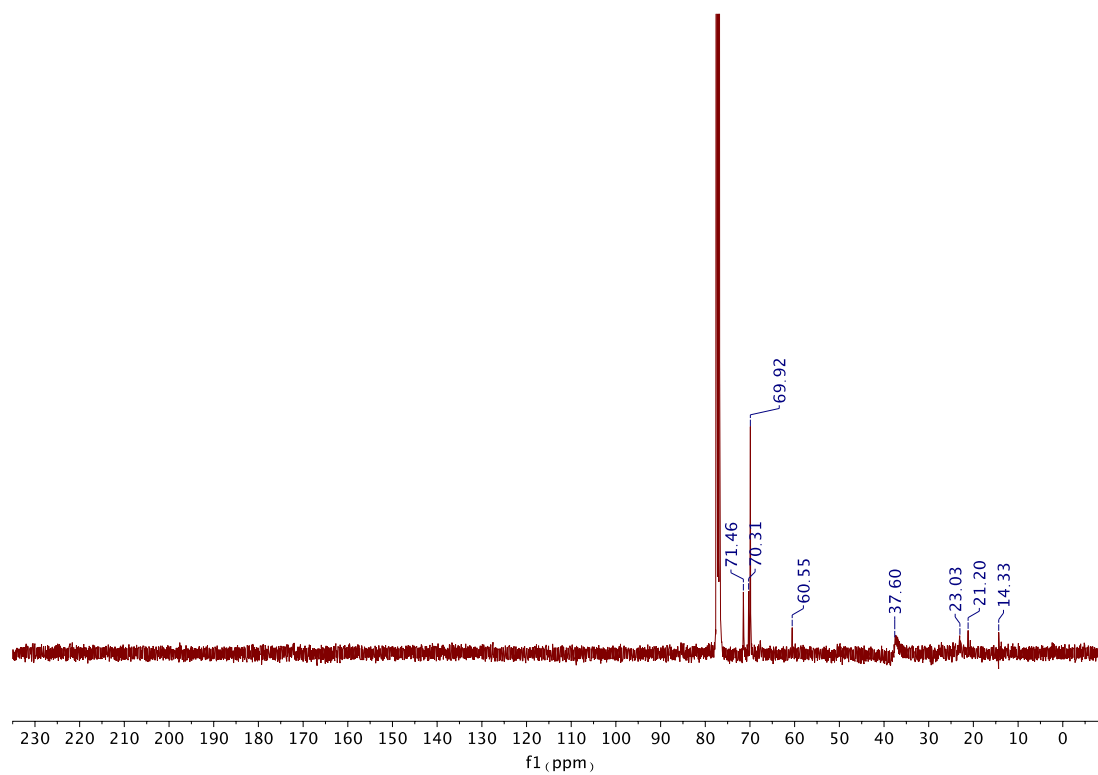
Figure 4.13A: $^{13}C\{^{1}H\}$ NMR spectrum of $[(CO_3)@Ag_{20}(S^tBu)_{10}(m\text{-}FeC_{21}H_{24}O_2N_3\text{-}C_6H_4COO)_8(DMF)_4]$ (**1-*m*** + FcBCN)in CDCl$_3$.
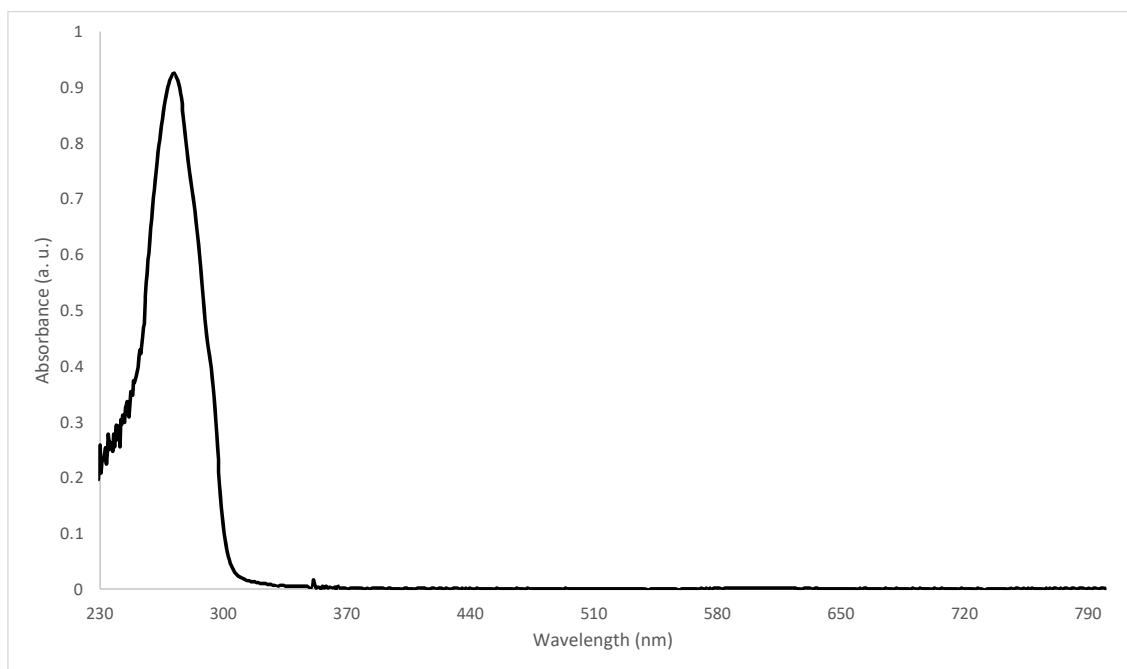
Figure 4.14A: UV-Vis. absorbance spectrum of a 0.048 mM *p*-azidobenzoic acid solution in DMSO (λ_{max} = 272 nm, ε = 19 000 L mol^{-1} cm^{-1})
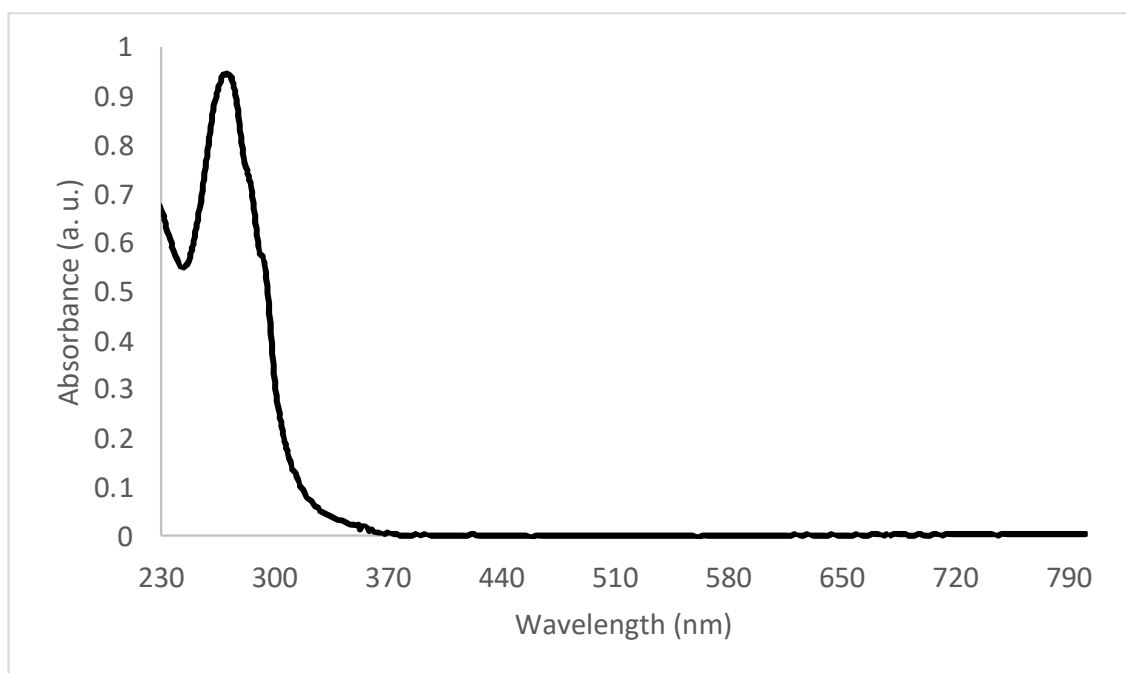
Figure 4.15A: UV-Vis. absorbance spectrum of a 0.0043 mM [(CO$_3$)@Ag$_{20}$(S^{t}Bu)$_{10}$(p-N$_3$-C$_6$H$_4$COO)$_8$(DMF)$_4$] (**1-*p***) solution in DCM (λ_{max} = 271 nm, ε = 218 000 L mol^{-1} cm^{-1})
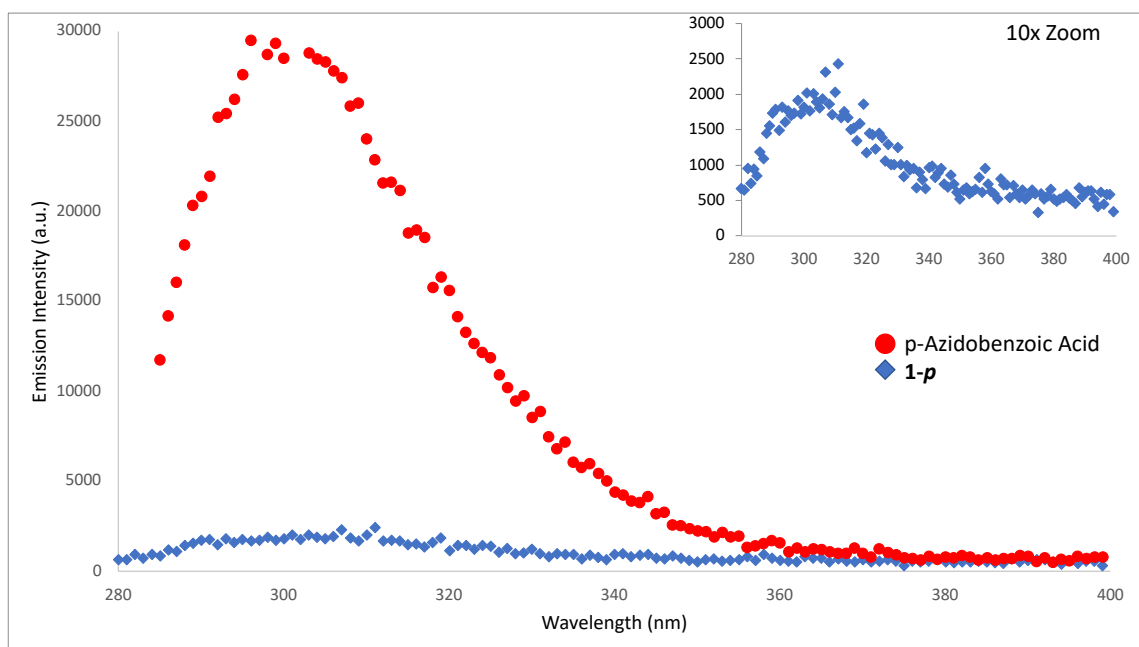
Figure 4.16A: Emission spectrum of $[(CO_3)@Ag_{20}(S^tBu)_{10}(p\text{-}N_3\text{-}C_6H_4COO)_8(DMF)_4]$ (**1-p**) ($\lambda_{\text{excitation}} = 270$ nm, $\lambda_{\text{max emission}} = 311.05$ nm) and *p*-azidobenzoic acid ($\lambda_{\text{excitation}} = 275$ nm, $\lambda_{\text{max emission}} = 297.05$ nm)
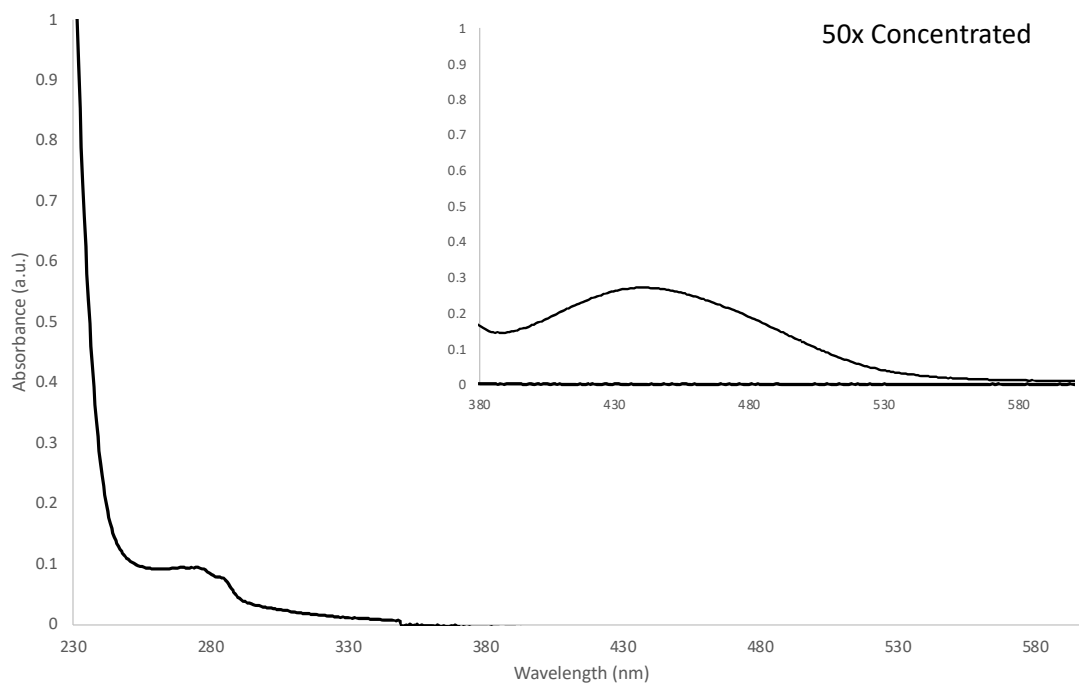
Figure 4.17A: UV-Vis. absorbance spectra of [(CO$_3$)@Ag$_{20}$(S^{t}Bu)$_{10}$(p-FeC$_{21}$H$_{24}$O$_2$N$_3$-C$_6$H$_4$COO)$_8$(DMF)$_4$] (**1-p** + FcBCN) in DCM (λ_{max}= 280 nm). Inset; Characteristic peak of ferrocene moiety centred at 445 nm.
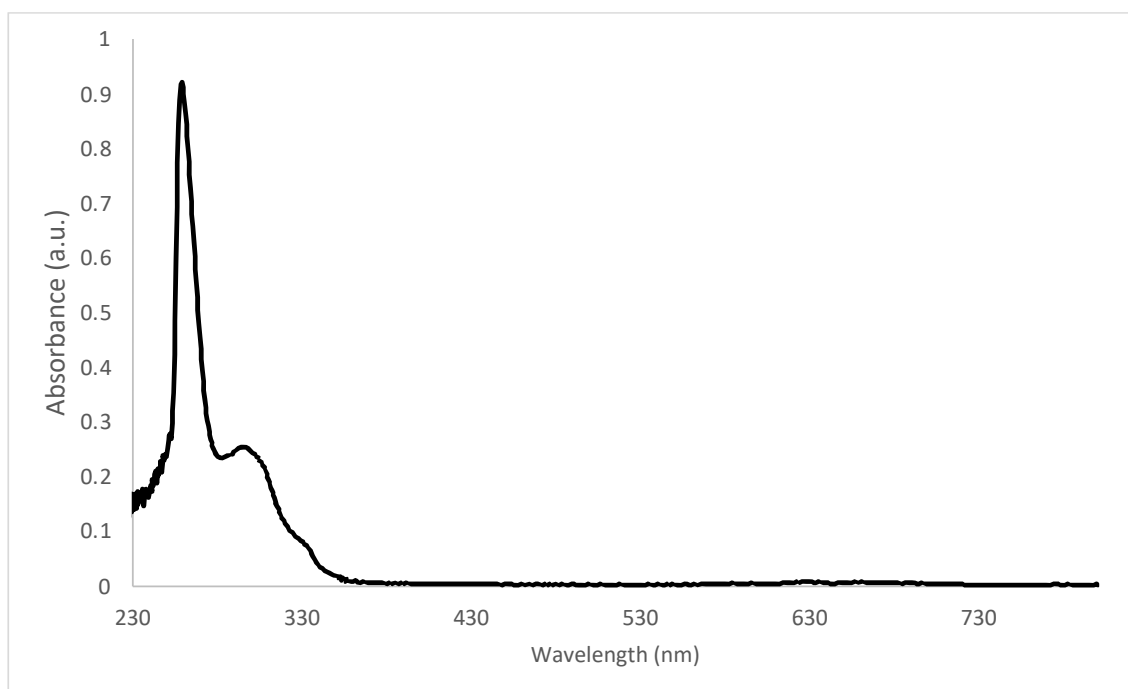
Figure 4.18A: UV-Vis. absorbance spectrum of a 0.11 mM solution of *m*-azidobenzoic acid in DMSO (λ_{max}= 260 nm, $\varepsilon = 8800$ L mol^{-1} cm^{-1}).
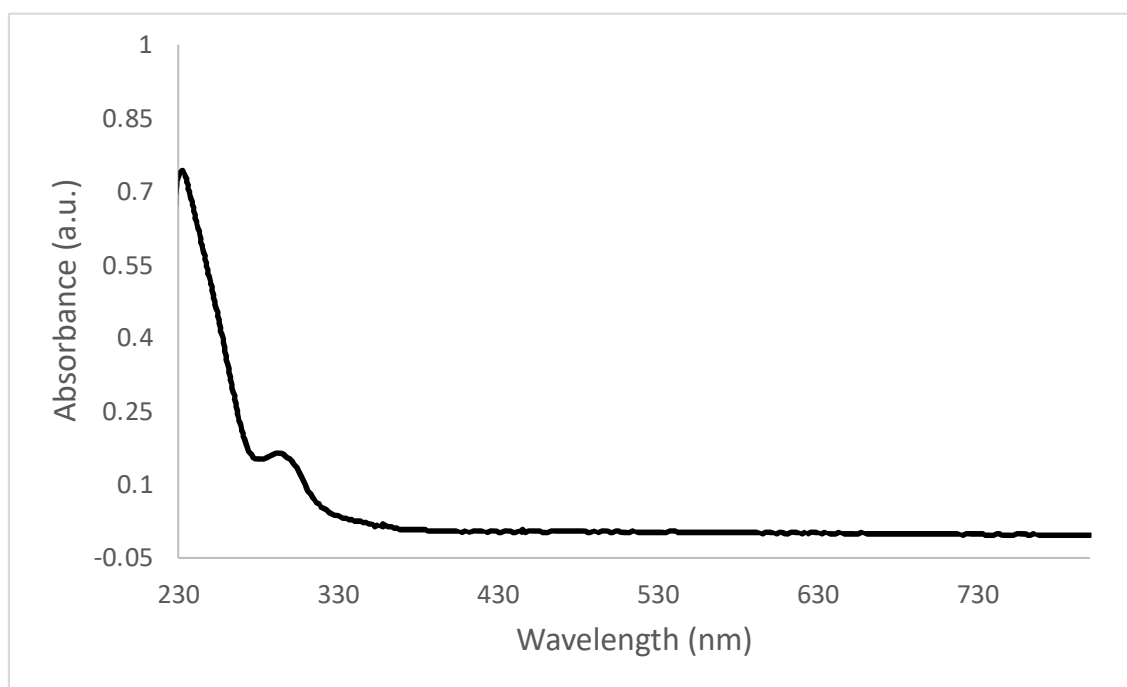
Figure 4.19A: UV-Vis. absorbance spectrum of a 0.0025 mM solution of [(CO$_3$)@Ag$_{20}$(S^{t}Bu)$_{10}$(*m*-N$_3$-C$_6$H$_4$COO)$_8$(DMF)$_4$] (**1-*m***) in DCM (λ_{max}= 293 nm, ε = 66 000 L mol^{-1} cm^{-1}).
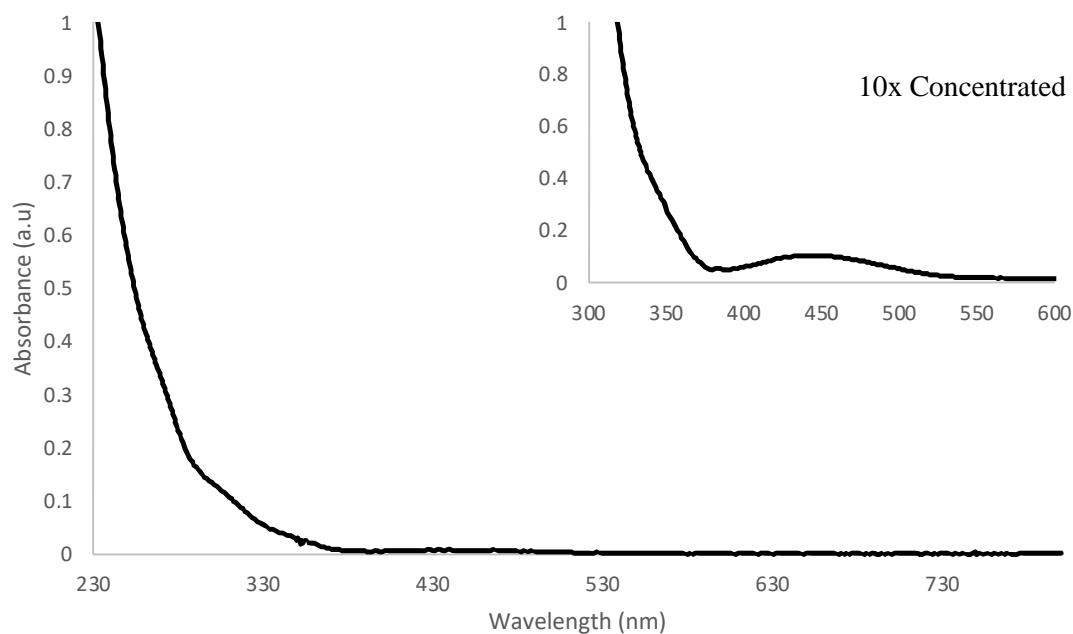
Figure 4.20A: UV-Vis. absorbance spectrum of a 0.0046 mM solution of $[(CO_3)@Ag_{20}(S^tBu)_{10}(m\text{-}FeC_{21}H_{24}O_2N_3\text{-}C_6H_4COO)_8(DMF)_4]$ (**1-*m*** + FcBCN) in DCM (λ_{max}= 267 nm, ε = 78 000 L mol^{-1} cm^{-1}). Inset; Characteristic peak of ferrocene moiety centred at 450 nm, observed at a concentration of 0.046 mM.
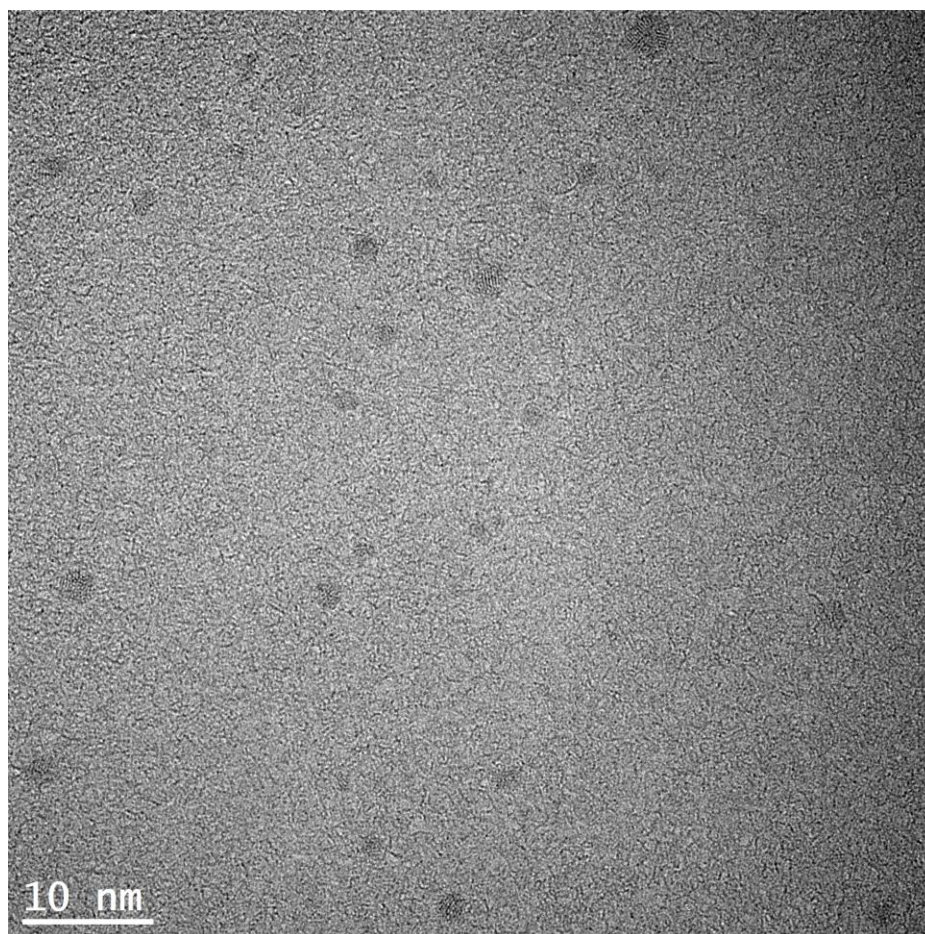
Figure 4.21A: Transmission electron microscopy images of the click product of BCN + **1-p**, Sample shows cluster species on the size regime of 2 – 3 nm (expected; 1.07 nm for $CO_3@Ag_{20}S_{10}$ core, 2.35 nm for benzoate – benzoate distance).
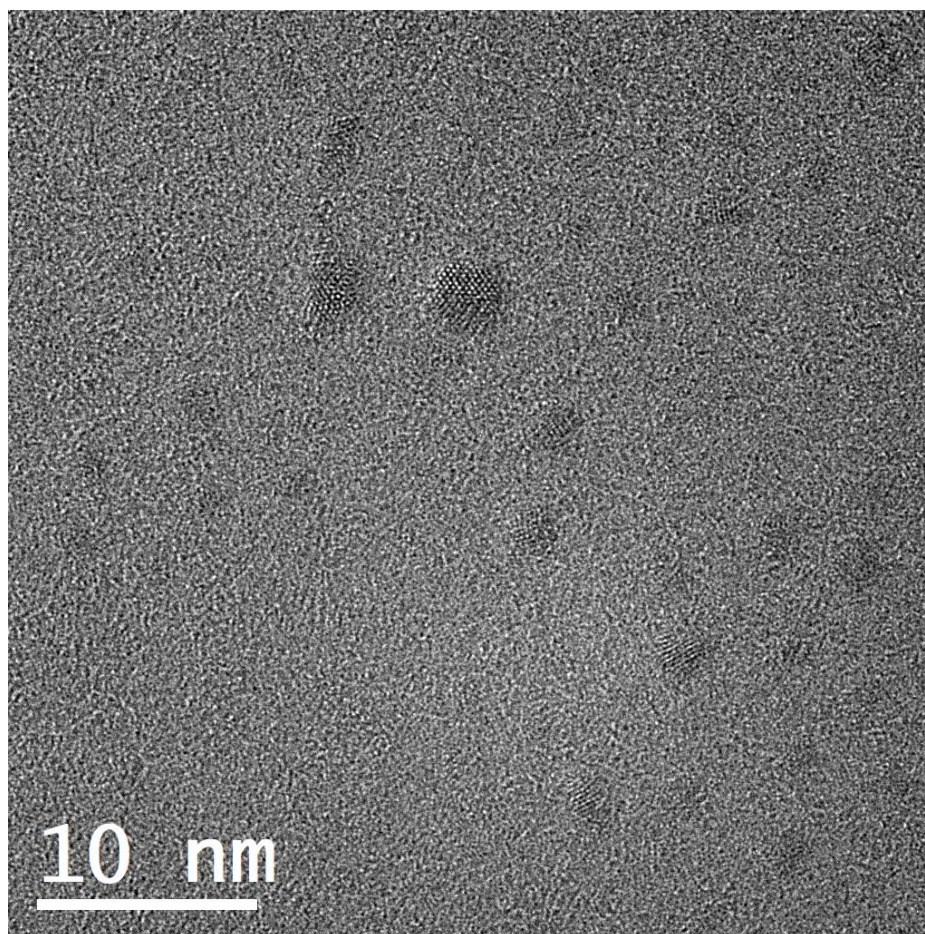
Figure 4.22A: Transmission electron microscopy images of **1-*m***, E) The click product of BCN + **1-*m***, F) The click product of FcBCN + **1-*m***. Sample shows cluster species on the size regime of 2 – 3 nm (expected; 1.07 nm for $CO_3@Ag_{20}S_{10}$ core, 2.35 nm for benzoate – benzoate distance).
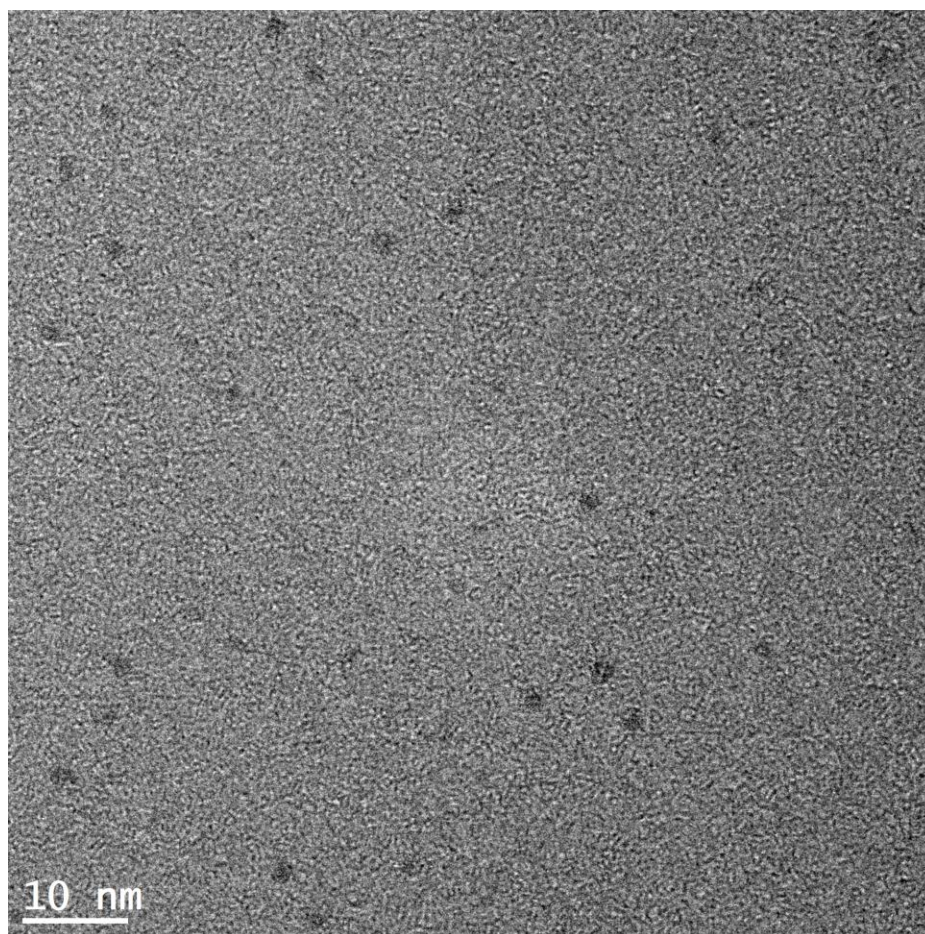
Figure 4.23A: Transmission electron microscopy images of the click product of BCN + **1-m**. Sample shows cluster species on the size regime of 2 – 3 nm (expected; 1.07 nm for $CO_3@Ag_{20}S_{10}$ core, 2.35 nm for benzoate – benzoate distance).
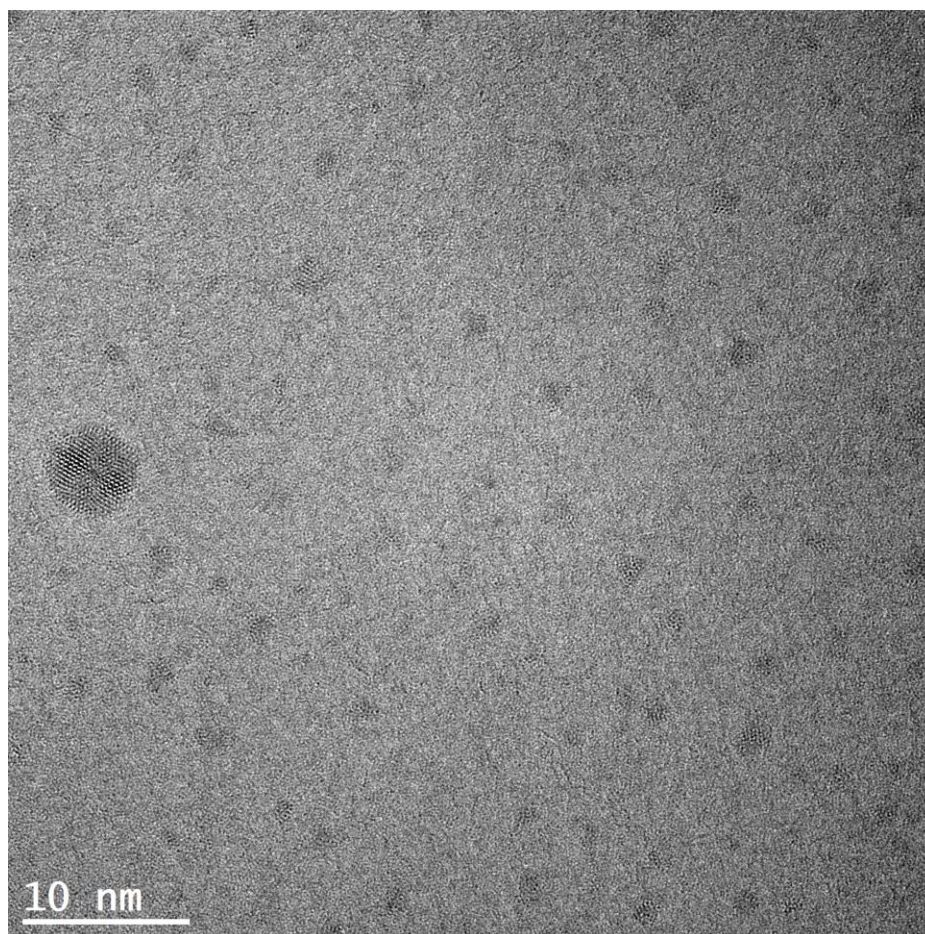
Figure 4.24A: Transmission electron microscopy images of the click product of FcBCN + **1-*m***. Sample shows cluster species on the size regime of 2 – 3 nm (expected; 1.07 nm for $CO_3@Ag_{20}S_{10}$ core, 2.35 nm for benzoate – benzoate distance), though some larger species are present due to agglomeration.
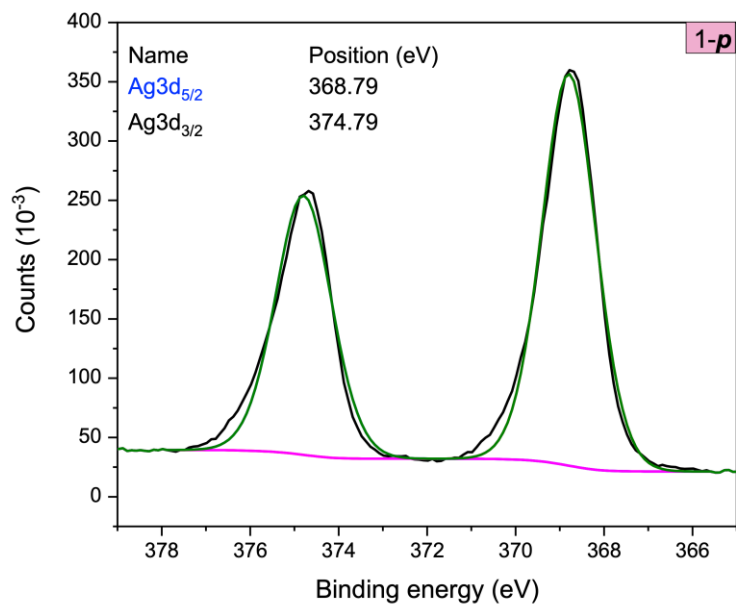
Figure 4.25A: XPS spectrum of the Ag3d region for **1-*p***, showing peaks corresponding to silver at 374.79 eV and 368.79 eV
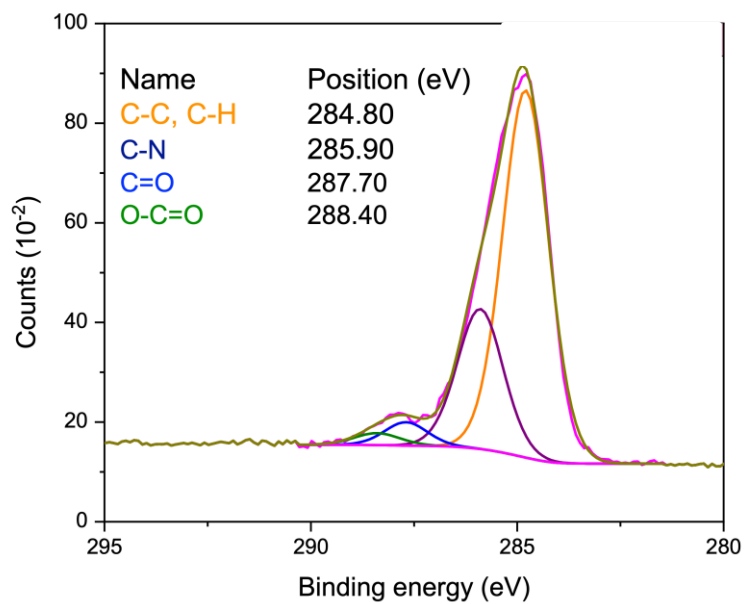
Figure 4.26A: XPS spectrum of the C1s region for **1-*p***, showing peaks corresponding to different carbon bonding modes, such as O-C=O at 288.40 eV, C=O at 287.70 eV, C-N at 285.90 eV, and C-C, C-H at 284.80 eV
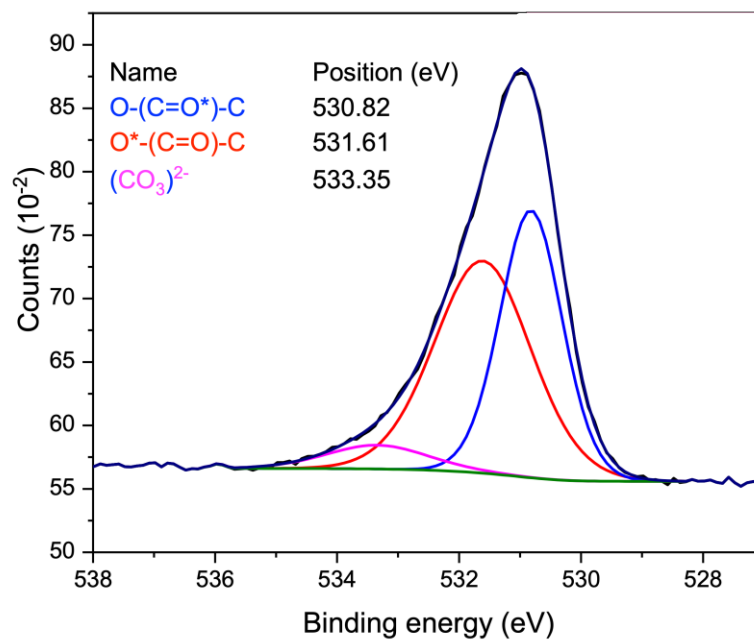
Figure 4.27A: XPS spectrum of the O1s region for **1-*p***, showing peaks corresponding to different oxygen bonding modes associated with carbonate at 533.35 eV, and carboxylates at 531.61 eV and 530.82 eV.
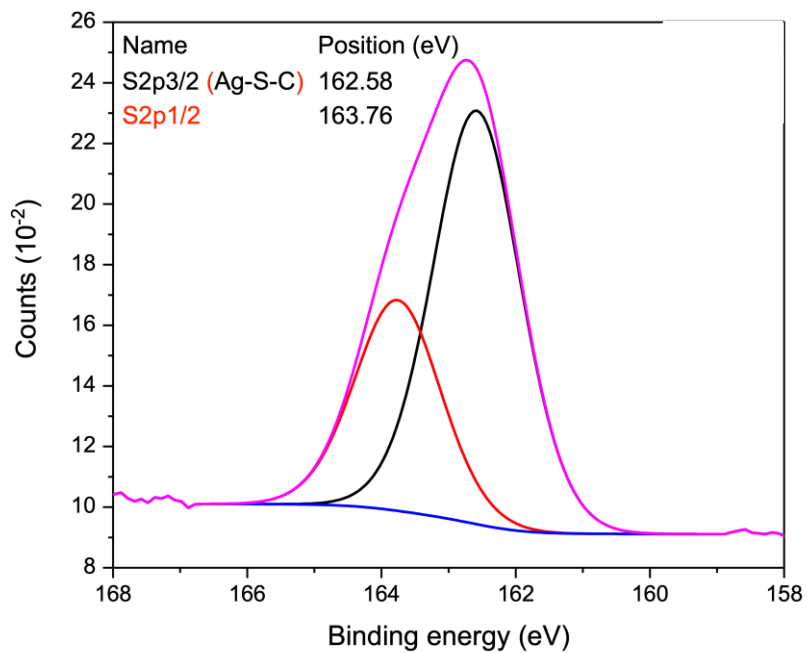
Figure 4.28A: XPS spectrum of the S2p region for **1-*p***, showing peaks corresponding to different sulfur bonding modes associated with the silver thiolate bond at 163.76 eV and 162.58 eV.
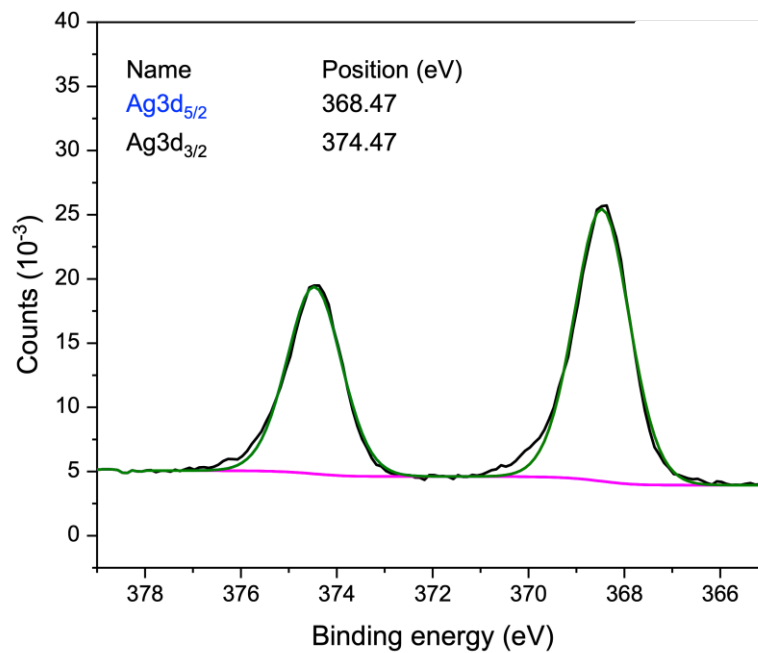
Figure 4.29A: XPS spectrum of the Ag3d region for the product of **1-*p*** + FcBCN, showing peaks corresponding to silver at 374.47 eV and 368.47 eV.
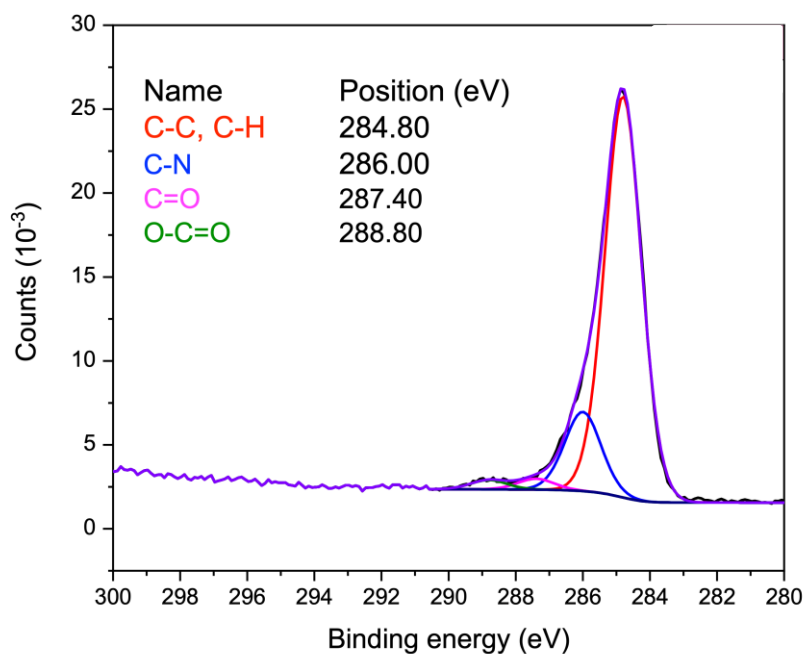
Figure 4.30A: XPS spectrum of the C1s region for the product of **1-*p*** + FcBCN, showing peaks corresponding to different carbon bonding modes, such as O-C=O at 288.80 eV, C=O at 287.40 eV, C-N at 286.00 eV, and C-C, C-H at 284.80 eV.
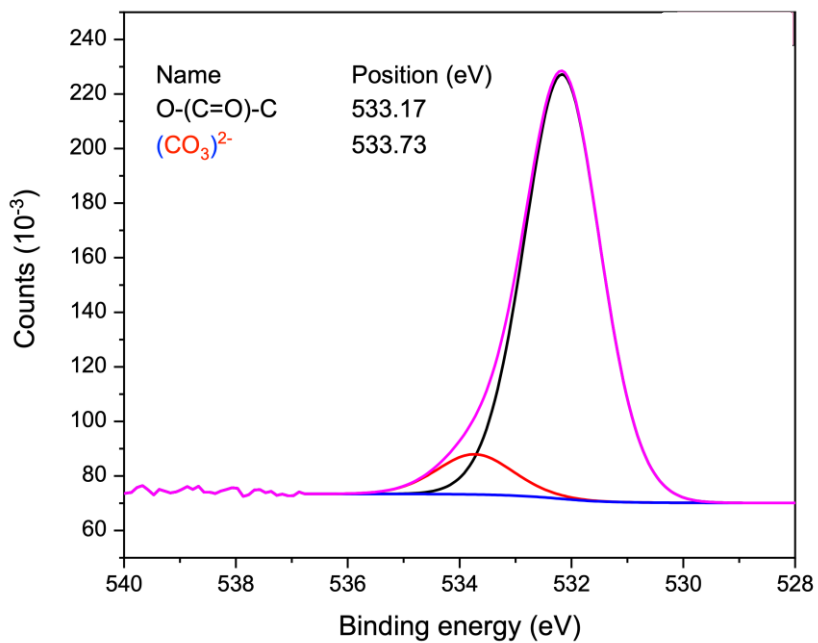
Figure 4.31A: XPS spectrum of the O1s region for the product of **1-*p*** + FcBCN, showing peaks corresponding to different oxygen bonding modes associated with carbonate at 533.73 eV and carboxylate ligands at 533.17 eV.
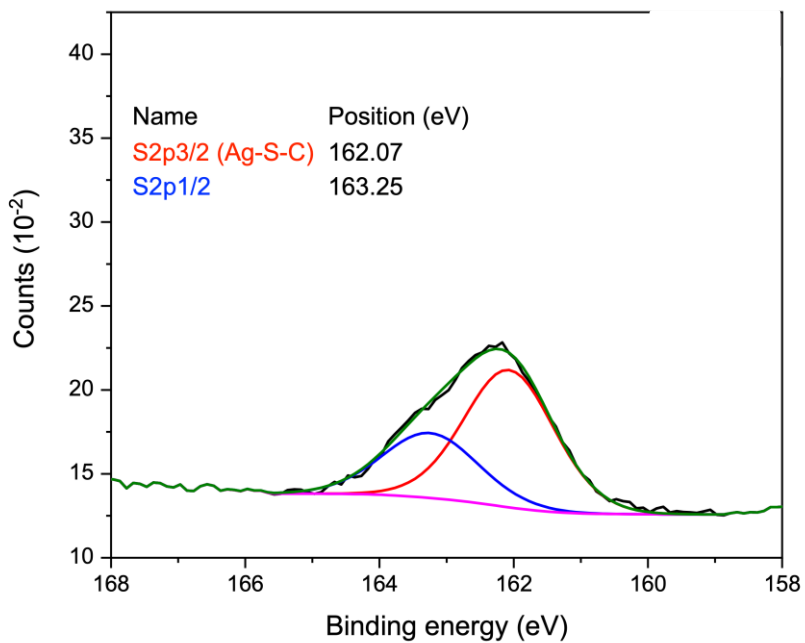
Figure 4.32A: XPS spectrum of the S2p region for the product of **1-*p*** + FcBCN, showing peaks corresponding to different sulfur bonding modes associated with the silver thiolate bond at 163.25 eV and 162.07 eV.
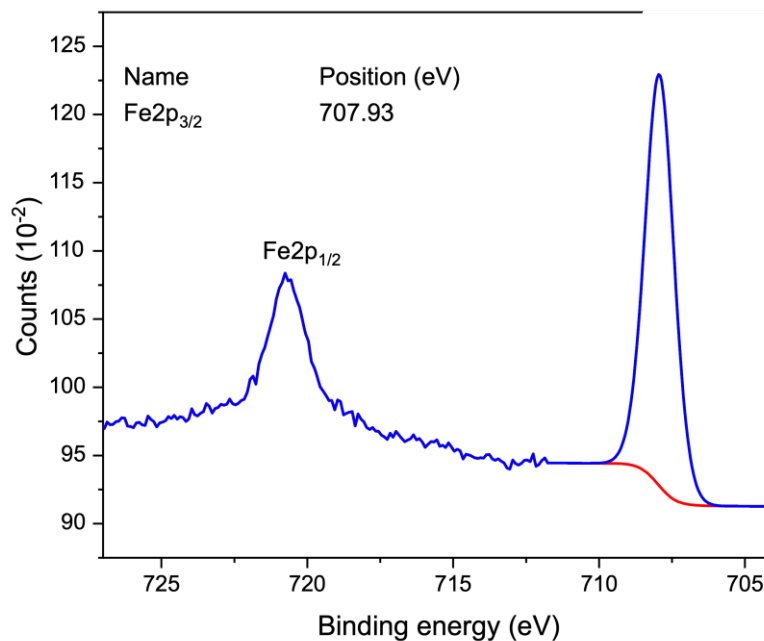
Figure 4.33A: XPS spectrum of the Fe2p region for the product of **1-*p*** + FcBCN, showing incorporation of ferrocene into the product based on the Fe peak at 707.93 eV.

4.4 Crystallographic Information

Data Collection and Processing. The sample was mounted on a Mitegen polyimide micromount with a small amount of Paratone N oil. All X-ray measurements were made on a Bruker Kappa Axis Apex2 diffractometer at a temperature of 110 K.

For the cluster decorated with 8 *p*-azidobenzoate ligands, **1-*p***, the unit cell dimensions were determined from a symmetry constrained fit of 9990 reflections with $4.78° < 2\theta < 72.08°$. The data collection strategy was a number of ω and φ scans which collected data up to $78.868°$ (2θ).

For the cluster decorated with 6 *p*-azidobenzoate ligands, **2-*p***, the unit cell dimensions were determined from a symmetry constrained fit of 9879 reflections with $4.66° < 2\theta < 56.52°$. The data collection strategy was a number of ω and φ scans which collected data up to $56.542°$ (2θ).

For the cluster decorated with 8 *m*-azidobenzoate ligands, **1-*m***, the unit cell dimensions were determined from a symmetry constrained fit of 9991 reflections with $4.46° < 2\theta < 56.72°$. The data collection strategy was a number of ω and φ scans which collected data up to $56.728°$ (2θ).

For the cluster decorated with 6 *m*-azidobenzoate ligands, **2-*m***, the unit cell dimensions were determined from a symmetry constrained fit of 9808 reflections with $4.96° < 2\theta < 49.98°$. The data collection strategy was a number of ω and φ scans which collected data up to $50.086°$ (2θ).

The frame integration was performed using SAINT.[5] The resulting raw data was scaled and absorption corrected using a multi-scan averaging of symmetry equivalent data using SADABS.[6]

Structure Solution and Refinement. The structure was solved by using a dual space methodology using the SHELXT program.[7] Most non-hydrogen atoms were obtained from the initial solution. The remaining atomic positions were obtained from subsequent difference Fourier maps. The clusters reside on a crystallographic inversion centre. Consequently, the templating CO_3^{2-} anion is disordered. The hydrogen atoms were introduced at idealized positions and were allowed to ride on the parent atom.

For the cluster decorated with *p*-azidobenzoate ligands, **1-*p***, the fractional formula arises from a compositional disorder where there is co-crystallized CH_3CN and DMF occupying the same site in the lattice. The occupancy of the predominant acetonitrile fraction refined to a value of 0.795(6). Two of the silver atom positions (Ag5/Ag5' and Ag10/Ag1D) were disordered. The occupancies for the Ag5 and Ag10 sites refined to values 0.761(13) and 0.830(6) respectively. The distances between the disordered silver pairs was 0.337 Å for

the Ag5/Ag5' pair and 0.505 Å for the Ag10/Ag1D pair. The thiolate ligand in residue 2 was disordered by a rotation about the S1 – C1 bond. The occupancy of the predominant rotamer refined to a value of 0.588(4). The coordinated DMF molecule in residue 11 was disordered. The occupancy of the predominant component refined to a value of 0.671(5). There was also a acetonitrile of solvation which disordered across a crystallographic inversion centre.

The structural model was fit to the data using full matrix least-squares based on F^2. The calculated structure factors included corrections for anomalous dispersion from the usual tabulation. The structure was refined using the SHELXL program from the SHELX suite of crystallographic software.[8] Graphic plots were produced using the Mercury program.[9] Additional information and other relevant literature references can be found in the reference section of this website (http://xray.chem.uwo.ca).
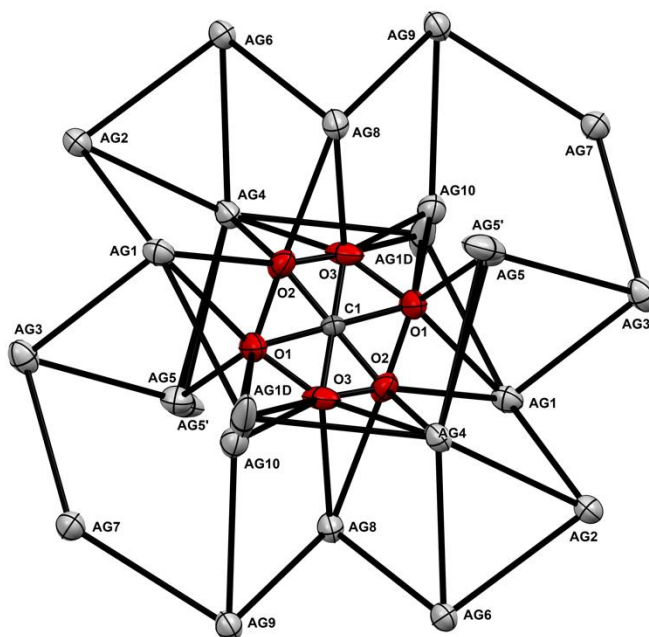
Figure 4.34A: ORTEP drawing of **1-*p*** cluster core showing naming and numbering scheme. Ellipsoids are at the 50% probability level.
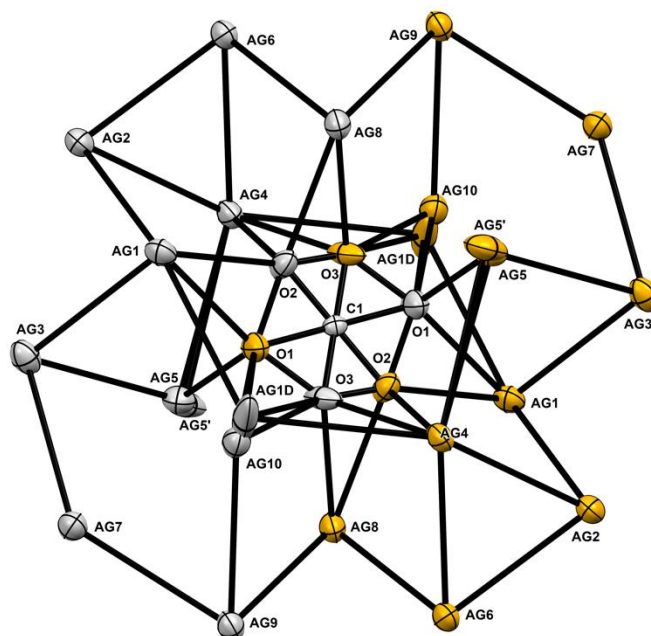
Figure 4.35A: ORTEP drawing of **1-*p*** cluster core coloured by symmetry operation showing naming and numbering scheme. Ellipsoids are at the 50% probability level. White coloured atoms show the asymmetric part of the cluster while the yellow-coloured atoms are the atoms related by a crystallographic centre of symmetry.
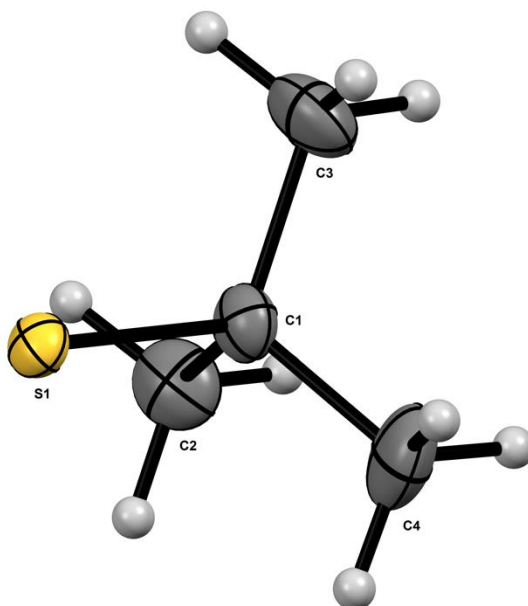
Figure 4.36A: ORTEP drawing of **1-*p*** cluster thiolate ligand showing naming and numbering scheme. Ellipsoids are at the 50% probability level and hydrogen atoms were drawn with arbitrary radii for clarity.
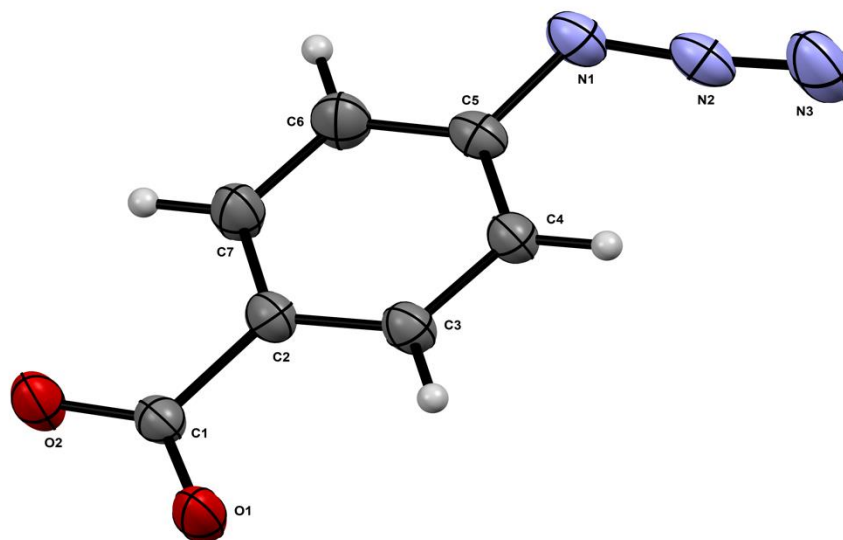
Figure 4.37A: ORTEP drawing of 1-*p* cluster carboxylate azide ligand showing naming and numbering scheme. Ellipsoids are at the 50% probability level and hydrogen atoms were drawn with arbitrary radii for clarity.

Table 4.1A: Summary of Crystal Data for **1-*p*** and **1-*m***

Formula	$C_{115.42}H_{160.70}Ag_{20}N_{31}O_{23.42}S_{10}$ (**1-*p***)	$C_{109}H_{150}Ag_{20}N_{28}O_{23}S_{10}$ (**1-*m***)
Formula Weight (*g/mol*)	4835.20	4698.55
Crystal Dimensions (*mm³*)	$0.441 \times 0.282 \times 0.175$	$0.163 \times 0.151 \times 0.069$
Crystal Color and Habit	colourless prism	colourless Prism
Crystal System	triclinic	triclinic
Space Group	P -1	P -1
Temperature, K	110	110
a, Å	15.811(7)	15.7006(9)

b, Å	16.110(6)	16.4507(9)
c, Å	18.026(5)	17.2409(10)
α,°	97.075(10)	62.3450(10)
β,°	111.638(14)	86.4050(10)
γ,°	107.925(8)	71.2090(10)
V, Å^3	3913(2)	3714.1(4)
Number of reflections to determine final unit cell	9990	9991
Min and Max 2θ for cell determination, °	4.78, 72.08	4.46, 56.72
Z	1	1
F(000)	2358	2283
ρ (*g/cm^{-3}*)	2.052	2.100
λ, Å, (MoKα)	0.71073	0.71073
μ, (*cm^{-1}*)	2.641	2.778
Diffractometer Type	Bruker Kappa Axis Apex2	Bruker Kappa Axis Apex2
Scan Type(s)	phi and omega scans	phi and omega scans
Max 2θ for data collection, °	78.868	56.728
Measured fraction of data	0.999	0.998

Number of reflections measured	419931	46485
Unique reflections measured	46684	18506
R_{merge}	0.0383	0.0191
Number of reflections included in refinement	46684	18506
Cut off Threshold Expression	$I > 2sigma(I)$	$I > 2sigma(I)$
Structure refined using	full matrix least-squares using F^2	full matrix least-squares using F^2
Weighting Scheme	$w=1/[sigma^2(Fo^2) + (0.0297P)^2 + 4.3473P]$ where $P=(Fo^2+2Fc^2)/3$	$w=1/[sigma^2(Fo^2) + (0.0238P)^2 + 3.5846P]$ where $P=(Fo^2+2Fc^2)/3$
Number of parameters in least-squares	1054	957
R_1	0.0318	0.0242
wR_2	0.0686	0.0548
R_1 (all data)	0.0554	0.0302
wR_2 (all data)	0.0795	0.0574
GOF	1.031	1.043
Maximum shift/error	0.003	0.002
Min & Max peak heights on final ΔF Map ($e^-/\text{Å}^3$)	-1.337, 2.853	-0.766, 1.251

Table 4.2A: Summary of Crystal Data for **2-*p*** and **2-*m***

Formula	$C_{101}H_{156}Ag_{20}N_{26}O_{27}S_{10}$ (**1-*p***)	$C_{95}H_{142}Ag_{20}N_{24}O_{25}S_{10}$ (**1-*m***)
Formula Weight (*g/mol*)	4644.51	4498.32
Crystal Dimensions (*mm³*)	$0.090 \times 0.083 \times 0.042$	$0.152 \times 0.064 \times 0.036$
Crystal Color and Habit	yellow plate	colourless rod
Crystal System	triclinic	triclinic
Space Group	P -1	P -1
Temperature, K	110	110
a, Å	13.4796(15)	18.381(8)
b, Å	16.3363(18)	18.601(8)
c, Å	17.368(2)	23,024(14)
α,°	90.682(2)	96.475(12)
β,°	104.230(2)	108.479(11)
γ,°	104.564(2)	106.329(14)
V, Å³	3577.3(7)	6987(6)
Number of reflections to determine final unit cell	9879	9808
Min and Max 2θ for cell determination, °	4.66, 56.52	4.96, 49.98

Z	1	2
F(000)	2260	4360
ρ (*g/cm^{-3}*)	2.156	2.138
λ, Å, (MoKα)	0.71073	0.71073
μ, (*cm^{-1}*)	2.884	2.948
Diffractometer Type	Bruker Kappa Axis Apex2	Bruker Kappa Axis Apex2
Scan Type(s)	phi and omega scans	phi and omega scans
Max 2θ for data collection, °	56.542	50.086
Measured fraction of data	0.998	0.998
Number of reflections measured	44228	113659
Unique reflections measured	17711	24677
R$_{merge}$	0.0423	0.0684
Number of reflections included in refinement	17711	24677
Cut off Threshold Expression	I > 2sigma(I)	I > 2sigma(I)
Structure refined using	full matrix least-squares using F^2	full matrix least-squares using F^2
Weighting Scheme	w=1/[sigma^2(Fo^2) + (0.0297P)^2 + 4.3473P] where P=(Fo^2+2Fc^2)/3	w=1/[sigma^2(Fo^2) + (0.0238P)^2 + 3.5846P] where P=(Fo^2+2Fc^2)/3

Number of parameters in least-squares	930	1641
R_1	0.0392	0.0482
wR_2	0.0762	0.1141
R_1 (all data)	0.0696	0.0883
wR_2 (all data)	0.0851	0.1324
GOF	1.035	1.038
Maximum shift/error	0.001	0.001
Min & Max peak heights on final ΔF Map (e^{-}/Å^3)	-1.828, 3.245	-1.340, 2.985

Where:

$R_1 = S \mid \mid F_o \mid - \mid F_c \mid \mid / S \, F_o$

$wR_2 = [\, S(\, w(\, F_o^2 - F_c^2 \,)^2 \,) \, / \, S(w \, F_o^4 \,) \,]^{\frac{1}{2}}$

$GOF = [\, S(\, w(\, F_o^2 - F_c^2 \,)^2 \,) \, / \, (\text{No. of reflns. - No. of params. })]^{\frac{1}{2}}$

4.5   Permission to Reprint and Adapt Copyrighted Material

Figure 4.38A: Permission to reprint Figure 1.1 (in Chapter 1. Section 1.2, from Reference 15 in Chapter 1 References)

Figure 4.39A: Permission to reprint Figure 1.2 (in Chapter 1. Section 1.3, from Reference 26 in Chapter 1 References)

Order Date	01-Nov-2022	Type of Use	Republish in a thesis/dissertation
Order License ID	1285276-1	Publisher	ROYAL SOCIETY OF CHEMISTRY
ISSN	1364-548X	Portion	Chart/graph/table/figure

LICENSED CONTENT

Publication Title	Chemical communications	Rightsholder	Royal Society of Chemistry
Article Title	Thermochromism and piezochromism of an atomically precise high-nuclearity silver sulfide nanocluster	Publication Type	e-Journal
		Start Page	2372
		End Page	2375
Author/Editor	Royal Society of Chemistry (Great Britain)	Issue	19
Date	01/01/1996	Volume	57
Language	English		
Country	United Kingdom of Great Britain and Northern Ireland		

REQUEST DETAILS

Portion Type	Chart/graph/table/figure	Distribution	Worldwide
Number of Charts / Graphs / Tables / Figures Requested	1	Translation	Original language of publication
		Copies for the Disabled?	No
Format (select all that apply)	Print, Electronic	Minor Editing Privileges?	Yes
Who Will Republish the Content?	Academic institution	Incidental Promotional Use?	No
Duration of Use	Life of current edition	Currency	CAD
Lifetime Unit Quantity	Up to 499		
Rights Requested	Main product		

NEW WORK DETAILS

Title	Synthesis and Surface Modification of Azide Decorated Silver Nanoclusters	Institution Name	The University of Western Ontario
		Expected Presentation Date	2022-12-05
Instructor Name	Alexander Stöckli		

ADDITIONAL DETAILS

Order Reference Number	N/A	The Requesting Person/Organization to Appear on the License	Alexander Stöckli

REUSE CONTENT DETAILS

Title, Description or Numeric Reference of the Portion(s)	Figure 1, Part A, B, C	Title of the Article/Chapter the Portion Is From	Thermochromism and piezochromism of an atomically precise high-nuclearity silver sulfide nanocluster
Editor of Portion(s)	Sun, Qiao-Qiao; Li, Qian; Li, Hai-Yang; Zhang, Miao-Miao; Sun, Meng-En; Li, Si; Quan, Zewei; Zang, Shuang-Quan	Author of Portion(s)	Sun, Qiao-Qiao; Li, Qian; Li, Hai-Yang; Zhang, Miao-Miao; Sun, Meng-En; Li, Si; Quan, Zewei; Zang, Shuang-Quan
Volume of Serial or Monograph	57		
Page or Page Range of Portion	2372-2375	Issue, if Republishing an Article From a Serial	19
		Publication Date of Portion	2021-03-07

Figure 4.40A: Permission to reprint Figure 1.3 (in Chapter 1. Section 1.3, from Reference 27 in Chapter 1 References)

CCC Marketplace

Order Date	01-Nov-2022	Type of Use	Republish in a thesis/dissertation
Order License ID	1285271-1	Publisher	ROYAL SOCIETY OF CHEMISTRY
ISSN	1364-548X	Portion	Chart/graph/table/figure

LICENSED CONTENT

Publication Title	Chemical communications	Rightsholder	Royal Society of Chemistry
Article Title	Small size yet big action: a simple sulfate anion templated a discrete 78-nuclearity silver sulfur nanocluster with a multishell structure.	Publication Type	e-Journal
		Start Page	2361
		End Page	2364
Author/Editor	Royal Society of Chemistry (Great Britain)	Issue	19
Date	01/01/1996	Volume	54
Language	English		
Country	United Kingdom of Great Britain and Northern Ireland		

REQUEST DETAILS

Portion Type	Chart/graph/table/figure	Distribution	Worldwide
Number of Charts / Graphs / Tables / Figures Requested	1	Translation	Original language of publication
		Copies for the Disabled?	No
Format (select all that apply)	Print, Electronic	Minor Editing Privileges?	Yes
Who Will Republish the Content?	Academic institution	Incidental Promotional Use?	No
Duration of Use	Life of current edition	Currency	CAD
Lifetime Unit Quantity	Up to 499		
Rights Requested	Main product		

NEW WORK DETAILS

Title	Synthesis and Surface Modification of Azide Decorated Silver Nanoclusters	Institution Name	The University of Western Ontario
		Expected Presentation Date	2022-12-05
Instructor Name	Alexander Stöckli		

ADDITIONAL DETAILS

Order Reference Number	N/A	The Requesting Person/Organization to Appear on the License	Alexander Stöckli

REUSE CONTENT DETAILS

Title, Description or Numeric Reference of the Portion(s)	Figure 2, Parts A and D	Title of the Article/Chapter the Portion Is From	Small size yet big action: a simple sulfate anion templated a discrete 78-nuclearity silver sulfur nanocluster with a multishell structure.
Editor of Portion(s)	Cheng, Li-Ping; Li, Yan-An; Luo, Geng-Geng; Peng, Tao; Su, Hai-Feng; Sun, Di; Wang, Zhi; Wu, Qiao-Yu; Zheng, Lan-Sun	Author of Portion(s)	Cheng, Li-Ping; Li, Yan-An; Luo, Geng-Geng; Peng, Tao; Su, Hai-Feng; Sun, Di; Wang, Zhi; Wu, Qiao-Yu; Zheng, Lan-Sun
Volume of Serial or Monograph	54		
Page or Page Range of Portion	2361-2364	Issue, if Republishing an Article From a Serial	19
		Publication Date of Portion	2018-03-07

Figure 4.41A: Permission to reprint Figure 1.4 (in Chapter 1. Section 1.3, from Reference 24 in Chapter 1 References)

Figure 4.42A: Permission to reprint Figure 1.5 (in Chapter 1. Section 1.4, from Reference 28 in Chapter 1 References)

Figure 4.43A: Permission to reprint Figure 1.6 (in Chapter 1. Section 1.4, from Reference 30 in Chapter 1 References)

Figure 4.44A: Permission to reprint Figure 1.7 (in Chapter 1. Section 1.4, from Reference 24 in Chapter 1 References)

Figure 4.45A: Permission to reprint Figure 3.1 (in Chapter 3. Section 3.1, from Reference 2 in Chapter 3 References)

4.6   References

1. Teo, B. K.; Xu, Y. H.; Zhong, B. Y.; He, Y. K.; Chen, H. Y.; Qian, W.; Deng, Y. J.; Zou, Y. H. *Inorg. Chem.* **2001**, *40* (26), 6794– 6801

2. Dommerholt, J.; Schmidt, S.; Temming, R.; Hendriks, L. J. A.; Rutjes, F. P. J. T.; van Hest, J. C. M.; Lefeber, D. J.; Friedl, P.; van Delft, F. L. *Angew. Chem. Int. Ed.* **2010**, *49* (49), 9422–9425

3. Yamashina, M.; Suzuki, H.; Kishida, N.; Yoshizawa, M.; Toyota, S. *Angew. Chem. Int. Ed.* **2021**, *60* (33), 17915-17919; *Angew. Chem.* **2021**, *133* (33), 18059-18063

4. Smith, P. A. S.; Hall, J. H.; Kan, R. O. *J. Am. Chem. Soc.* **1962**, *84* (3), 485-489

5. Bruker-AXS, SAINT version 2013.8, **2013**, Bruker-AXS, Madison, WI 53711, USA

6. Bruker-AXS, SADABS version 2012.1, **2012**, Bruker-AXS, Madison, WI 53711, USA

7. Sheldrick, G. M., *Acta Cryst.* **2015**, *A71*, 3-8

8. Sheldrick, G. M., *Acta Cryst.* **2015**, *C71*, 3-8

9. Macrae, C. F.; Bruno, I. J.; Chisholm, J. A.; Edington, P. R.; McCabe, P.; Pidcock, E.; Rodriguez-Monge, L.; Taylor, R.; van de Streek, J. and Wood, P. A. *J. Appl. Cryst.*, **2008**, *41*, 466-470

Curriculum Vitae

Name: Alexander Stöckli

Post-secondary Education and Degrees:
Mount Allison University
Sackville, New Brunswick, Canada
2016-2020 H. B. Sci.

The University of Western Ontario
London, Ontario, Canada
2020-2022 M. Sc.

Honours and Awards:
University of Toronto National Book Award
2016

Governor General's Academic Award Medal
Bronze
2016

Sterling Walls Entrance Scholarship
Mount Allison University
2016

H. E. Bigelow Research Award
2019

H. E. Bigelow Undergraduate Scholarship
2019

T. A. of the Month
Mount Allison University
2019

Western Graduate Research Scholarship
2021

Related Work Experience
Teaching Assistant
Mount Allison University
2019-2020

Student Research Assistant
Mount Allison University
2019-2020

Teaching Assistant
The University of Western Ontario
2020-2022